Predicting and Improving Damage Tolerance of Composite Structures

Lundsgaard-Larsen, Christian

Publication date:
2009

Document Version
Publisher's PDF, also known as Version of record

Predicting and Improving Damage Tolerance of Composite Structures

PhD Thesis

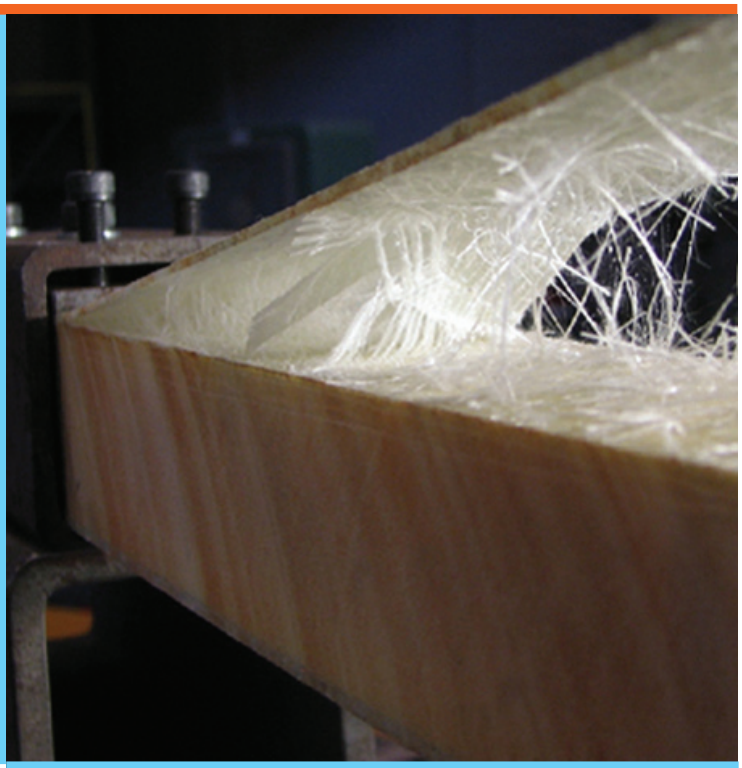

Christian Lundsgaard-Larsen
DCAMM Special Repport No. S107
August 2008

DTU Mechanical Engineering
Department of Mechanical Engineering

Predicting and Improving Damage Tolerance of Composite Structures

Christian Lundsgaard-Larsen

TECHNICAL UNIVERSITY OF DENMARK
DEPARTMENT OF MECHANICAL ENGINEERING
SECTION OF COASTAL, MARITIME AND STRUCTURAL ENGINEERING
AUGUST 2008

Published in Denmark by
Technical University of Denmark

Section of Coastal, Maritime and Structural Engineering
Department of Mechanical Engineering
Technical University of Denmark
Nils Koppels Alle, Building 403, DK-2800 Kgs. Lyngby, Denmark
Phone +45 4525 1360, Telefax +45 4588 4325
E-mail: info.skk@mek.dtu.dk
WWW: http://www.mek.dtu.dk/

Publication Reference Data
Lundsgaard-Larsen, C.
Predicting and Improving Damage Tolerance of Composite Structures
PhD Thesis
Technical University of Denmark, Section of Coastal, Maritime and Structural Engineering.
August, 2008
ISBN xxxxx
Keywords: Cohesive law, Cohesive zone modelling, Composites, Sandwich structures, Fibre bridging, DCB-UBM, ENF, Dynamic fracture, J integral

Preface

This thesis is submitted as a partial fulfilment of the requirements for the Danish Ph.D. degree. The work was conducted at the Section of Coastal, Maritime and Structural Engineering, Department of Mechanical Engineering, Technical University of Denmark, during the period from March 2005 to August 2008. The project was supervised by Associate Professor Christian Berggreen, Senior Scientist Bent F. Sørensen and Professor Jørgen Juncher Jensen.

My sincere thanks to Associated Professor Christian Berggreen for his encouragement, enthusiasm and many fruitful discussions. His help and guidance is highly appreciated. Great thanks to Senior Scientist Bent F. Sørensen from the Materials Research Department, Risø DTU, for highly skilled and invaluable help. I am further grateful to Professor Jørgen Juncher Jensen for making many complicated formal matters seem trouble-free and to colleagues at the Department for creating a friendly and inspiring working environment. Also thanks to Professor Leif A. Carlsson for his constructive criticism.

Part of this thesis was conducted abroad during five months at Teledyne Scientific in Thousand Oaks, California, USA, and two months at University of Genova, Italy. Very special thanks go to Dr. Brian N. Cox and Associate Professor Roberta Massabò for giving me the opportunity to visit them and for many highly educational discussions.

Thanks to M.Sc. student Ulrik Rasmussen for excellent work regarding the manufacture of test specimens and help to carry out the experiments described in Chapter 5. I am also very grateful to M.Sc. students Claus Jenstrup and Kasper Karlsen, who carried through their Master's thesis project with the author as co-supervisor. Their highly skilled work contributed to developing the methods described in Section 3.3.

I would also like to thank Poul-Erik Hyldbo and Torben Bender Christensen from the workshop at Mechanical Engineering, DTU for preparing specimens, Tom Løgstrup Andersen, Christian H. Madsen and Jacob Christensen from Fiberlab, Risø DTU, for help with the manufacture of sandwich panels, and the staff at AFM, Risø DTU, for assistance during the experiments.

My very special thanks go to Lina for her great support during the entire study.

This page is intentionally left blank.

Executive Summary

When optimised composite structures operating in a stochastic loading environment are designed, the question often arises whether a flaw or damage of a given size in the structure is critical or not. Defects may occur randomly during production or due to handling or in-service use. Thus, to generate guidelines for the damage assessment of composite structures, a need for reliable methodologies and models, able to predict the residual strength of damaged composite structures, exists.

In this thesis special attention is given to sandwich structures where thin stiff faces are adhered to a thick light core, which acts as a separating medium increasing the bending stiffness and bending strength. In a sandwich component, face/core debonds are a common and critical defect, and during loading a debonded area of the sandwich may act as a starter crack, propagating throughout large parts of the sandwich structure. Thus, it is necessary to explore methodologies for predicting crack growth in debonded sandwich structures and, furthermore, to be able to design the face/core interface in a way that limits or prohibits crack growth.

Propagation of a face/core debond often entails fibers connecting the separated crack faces, which partially shield the crack tip from the loading and thus increase the fracture resistance. As the zone of bridging fibers becomes large, Linear Elastic Fracture Mechanics (LEFM) is not applicable and a Cohesive Zone Model (CZM) may be applied instead. A CZM entails two steps: (1) measure cohesive laws at various mixed mode loadings, and (2) implement the cohesive laws in a finite element model in order to predict the fracture behaviour of different geometries and loading conditions.

In the first step a new test method for measuring mixed-mode cohesive laws from face/core cracking of sandwich structures is proposed. The method utilises an existing testing principle where a Double Cantilever Beam is loaded by Uneven Bending Moments (DCB-UBM). The proposed modifications entail adhering steel layers to the sandwich faces to reduce deflections. The J integral is derived analytically by use of laminate beam theory, and mixed-mode cohesive laws are extracted by relating the J integral to the opening of the pre-crack tip, measured by a Digital Image Correlation (DIC) system. The accuracy of the approach is discussed along with the fracture behaviour for two different tested materials.

The DCB-UBM tests show that a face/core debond crack may propagate in three basic ways: (1) propagate in the interface, (2) kink into the face, or (3) kink into the core. The fracture

resistance may be very different along the various paths and the crack tends to propagate where the resistance is smallest. As the crack propagates in the face/core interface or kinks into the face, Large Scale Bridging (LSB) may develop. It is desired to utilise fibre bridging in a controlled manner to arrest the crack in the interface. A glass fibre mat of randomly oriented fibre strands, either in the form of a Chopped Strand Mat (CSM) with short fibres or as a Continuous Filament Mat (CFM) with long fibres, is inserted between the face and core during production. In mode I dominated loading conditions, tests show that the crack tends to propagate in the CSM/CFM layer where fibres are easily pulled out, which leads to large-scale bridging and consequently increased fracture resistance. It is found that the amount of fibre bridging varies with mode-mixity, and for the CSM configuration the steady state fracture resistance is between 0.8 and 1.6 kJ/m^2, while for the CFM it varies between 0.8 and 2.4 kJ/m^2.

It is unwanted that the crack kinks from the CSM/CFM layer and into the adjacent face layers (often multi-axial or UD layers) since this will damage the load-carrying laminate. To limit the tendency of crack kinking it is proposed to insert a thin woven layer between the load carrying face layers and the CSM/CFM layer, which extends the mode-mixity transition point where the crack divert into the load carrying face laminate. The crack never penetrates the woven layer, but for high mode II loadings an additional crack is developing on the opposite side of the woven layer, and eventually this continues to kink into the load carrying face laminate.

The methodology of initially measuring cohesive laws and subsequently implementing these in a model which predicts the fracture behaviour of another geometry is tested. The other geometry constitutes a sandwich beam, fixed at the ends, while at the centre an initial debond crack is propagated by pulling the sandwich face apart from the core. The geometry has the effect that the mode-mixity at the crack tip changes gradually from mode I to intermediate mixed-mode. Thus, the test is highly versatile for the validation of the methodology in a large mode-mixity spectrum. Tests with both the CSM and CFM lay-up configurations are conducted and experimental and numerical results are compared. The numerical and experimental results fit within deviations of approximately 50 %, and possible sources for the deviations are discussed.

Finally, a pure numerical study of the fracture of a composite End Notched Flexure (ENF) specimen is presented. There is a wish to measure cohesive laws from composites with Through-Thickness Reinforcements (TTR) during high-rate loading, and this study is an initial step towards designing suitable test specimens. A finite element model of the ENF specimen is generated, and the objective is to investigate the influence of the shape of the cohesive law on the fracture response at high-rate loadings. If the responds is sensitive to the shape of the cohesive law, it is plausible that cohesive laws may be extracted by conducting high-rate experiments and subsequently changing the cohesive law in the finite element model, until numerical results coincide with the experimental results.

It is found that at loading rates between 0 and 40 m/s, a load point displacement range appears in the simulation where both the crack tip speed and the displacement profile inside

the process zone are approximately constant. For this range cohesive laws may be extracted and associated with a certain rate. As the load point speed is increased to 40 m/s, the crack tip speed increases successively to 273 m/s, whereas load point speeds above 40 m/s do not increase the rate further, but instead lead to various undesirable dynamic effects such as oscillations and multiple process zones developing in the specimen. Generally, results suggest that the displacement profile (which may be measured experimentally using a high-speed DIC system) is sensitive to the cohesive law, in apposition to the reaction force where dynamic effects tend to overrule the effects of the cohesive law. The sliding speed is believed to be a more adequate rate measure than the crack tip speed, and a simple method for determining the sliding speed in the process zone from the crack tip speed and the sliding displacement profile is suggested. Results from simulations are used to support the proposed method.

This page is intentionally left blank.

Synopsis

Ved design af optimerede kompositstrukturer, der skal operere i stokastisk varierende belastningsmiljøer, opstår spørgsmålet, om en defekt af en given størrelse i strukturen er kritisk eller ej. Defekter kan opstå tilfældigt under produktionen, ved håndtering eller under brug. For at kunne skabe retningslinjer for skadeståleligheden af kompositstrukturer, er der et behov for pålidelige metoder, der kan forudsige den tilbageværende styrke af skadede kompositstrukturer.

I denne afhandling er særlig opmærksomhed rettet mod sandwichstrukturer, hvor stive skind er limet på en let kærne, der har funktion som et afstandsstykke, der øger bøjningsstivheden og bøjningsstyrken. I en sandwichkomponent er skind/kærne delamineringer en almindelig og kritisk defekt, der kan agere som en startrevne, og ved belastning sprede sig ud i store dele af sandwichstrukturen. Derfor er det nødvendigt at udforske metoder til at forudsige revneudbredelsen i delaminerede sandwichstrukturer og desuden designe skind/kærne samlingen på en måde, som begrænser eller forhindrer revneudbredelse.

Propagering af en skind/kærne delaminering medfører ofte fibre, der forbinder de separerede brudflader, hvilket skærmer revnespidsen fra belastningen og øger brudsejheden. Når zonen af krydsende fibre bliver stor er lineær elastisk brudmekanik (LEFM) ikke længere brugbart og i stedet kan en kohæsiv zone model bruges. En kohæsiv zone model består af to skridt: (1) måle kohæsive love ved varierende mixed-mode belastninger, og (2) implementere de kohæsive love i en finit element model til at forudsige brudopførslen af forskellige geometrier og belastningstilfælde.

En metode til at måle mixed-mode kohæsive love fra revneudbredelse i skind/kærne samlinger af sandwichstrukturer er foreslået. Metoden udnytter et testprincip, hvor en dobbelt konsol bjælke bliver belastet med uens bøjningsmomenter (DCB-UBM). De foreslåede modifikationer består i at lime stållag på sandwichskindene for at reducere deformationerne. J integralet er udledt analytisk ved brug af laminat bjælketeori, og mixed-mode kohæsive love er udledt ved at relatere J integralet til åbningen af startrevnespidsen, som er målt med en digital billedkorrelationsmetode. Nøjagtigheden af fremgangsmåden er diskuteret sammen med variationen i brudadfærd for to forskellige testede materialer.

DCB-UBM forsøgene viser, at en skind/kærne delamineringsrevne kan propagere på tre grundlæggende måder: (1) propagere i samlingen, (2) kinke ind i skindet eller (3) kinke ind

i kærnen. Brudsejheden kan være meget forskellig i de forskellige materialer, og revnen har for vane at propagere der, hvor modstanden er mindst. I tilfælde af at revnen kinker ind i skindet, kan fibre krydse de genererede brudflader, hvilket skærmer revnespidsen mod belastningen og øger brudsejheden. Det er et mål at udnytte de krydsende fibre på en kontrolleret måde til at forhindre revnen i at propagere videre. En fiberglasmåtte af tilfældigt orienterede fiberbundter enten med korte fibre (CSM) eller med lange (CFM) er indsat mellem skind og kærne under produktionen. I mode I dominerede belastninger viser forsøgene, at revnen har tendens til at propagere i CSM/CFM laget, hvor fibrene er lette at trække ud, hvilket leder til krydsende fibre i stor skala, og som følge heraf øges brudsejheden. Det ses, at mængden af krydsende fibre varierer med mode-mixity, og for CSM konfigurationen er ligevægtsbrudsejheden mellem 0.8 og 1.6 kJ/m^2, mens den for CFM er mellem 0.8 og 2.4 kJ/m^2.

Det ønskes ikke at revnen skal kinke fra CSM/CFM laget og ind i skindet, da dette vil skade det lastbærende laminat. For at begrænse tendensen til at revnen kinker, indsættes et tyndt lag vævet glasfiber mellem skind og CSM/CFM, hvilket forlænger mode-mixity værdien, hvor revnen kinker (dvs. at der kræves en mere mode II domineret belastning for, at revnen kinker ud af CSM/CFM laget). Revnen gennembryder ikke det vævede lag, men ved høje mode II tilfælde, initieres en ekstra revne på den modsatte side af det vævede lag, og til sidst fortsætter revnen med at kinke ind i skindet.

En systematisk metode bestående i først at måle kohæsive love for et sandwich testemne og efterfølgende implementere den kohæsive lov i en model til at forudsige brudopførslen af en anden geometri er undersøgt. Den anden geometri er en sandwichbjælke, holdt fast ved enderne mens en delaminering i midten udbredes ved at trække i sandwichskindet i en retning vinkelret på skindets overflade. Geometrien medfører, at mode-mixity ved revnespidsen ændres gradvist fra mode I domineret til mixed-mode midt imellem mode I og mode II, efterhånden som revnen propagerer, dvs. testmetoden er meget alsidig, i og med at metoden bliver testet i et bredt mode-mixity spektrum. Både CSM og CFM konfigurationen bliver testet, og eksperimentelle og numeriske resultater bliver sammenlignet. De numeriske og eksperimentelle resultater passer indenfor ca. 50 % afvigelse, og mulige kilder til afvigelserne er diskuteret.

Afslutningsvis præsenteres et rent numerisk studie af et revnet emne belastet i bøjning (ENF). Der hersker et ønske om at måle kohæsive love fra kompositter med forstærkninger gennem tykkelsesretningen under høje belastningshastigheder, og dette studie er et første skridt på vejen mod at designe testemner. En finit element model af ENF emnet bygges op, og målet er at undersøge indflydelsen af den kohsive lovs form på emnets opførsel under brud ved højhastigheds belastninger. Hvis emnets opførsel er følsom overfor den kohæsive lov, er det plausibelt, at den kohæsive lov kan findes ved først at udføre højhastighedsforsøg og derefter ændre den kohæsive lov i finit element modellen, indtil numeriske resultater er sammenfaldende med de eksperimentelle.

Det ses, at ved belastningshastigheder på mellem 0 og 40 m/s, fremkommer et tidsinterval, hvor både revnespidshastigheden og flytningsprofilet i proceszonen er nogenlunde konstante. I dette interval er det sandsynligt, at kohæsive love kan genereres fra forsøgene og

associeres med en given brudhastighed. Når belastningshastigheden bliver øget til 40 m/s, stiger hastigheden af revnespidsen gradvist til 273 m/s, hvorimod belastningshastigheder over 40 m/s ikke øger brudhastigheden men i stedet leder til forskellige uønskede dynamiske effekter såsom oscillationer og udvikling af flere proceszoner i emnet. Generelt antyder resultaterne, at flytningsprofilet, som kan måles experimentalt ved hjælp af et digital billedekorrelationssystem, er følsomt overfor den kohæsive lov i modsætning til reaktionskraften, hvor dynamiske effekter har det med at tilsidesætte effekterne fra den kohæsive lov. Det antages at forskydningshastigheden er et mere generelt passende mål for brudhastighed end revnespidshastigheden, og en simpel metode til at bestemme forskydningshastigheden i proceszonen ud fra revnespidshastigheden og forskydningsprofilet foreslås. Det er konstateret, at resultater fra simuleringen understøtter den foreslåede metode.

This page is intentionally left blank.

Contents

This page is intentionally left blank.

Symbols

Roman Symbols

A_b	extension stiffness term for beam b
a	crack length
a_o	pre-crack length
a_s^I	material length scale
B	specimen width
B_b	coupling stiffness term for beam b
b	integer subscript (beam index)
D	damage variable in ABAQUS
D_b	bending stiffness term for beam b
$\overline{E}$	plane strain or stress Young's modulus
E_c	Young's modulus of core
E_el	elastic energy
E_f	Young's modulus of face
E_{kin}	kinetic energy
E_s	Young's modulus of steel
$\mathcal{G}_i$	energy release rate for crack propagating along interface
$\mathcal{G}_m$	energy release rate for crack propagating in matrix material
H	specimen dimension
H_1	thickness beam 1
H_2	thickness beam 2
h	specimen dimension
J	J integral value
J_o	crack tip fracture energy
J_I	mode I dissipated damage energy
J_{II}	mode II dissipated damage energy
J_I^c	work of separation for pure mode I
J_{II}^c	work of separation for pure mode II
$J_{bridging}$	fracture resistance due to bridging
J_{damage}	sum of mode I and II damage energies
$J_{damage,inc}$	increase in damage energy during output time step

J_R	fracture resistance of the material
$J_{reversible}$	reversible (elastic) energy in cohesive element
J_{ss}	steady-state fracture resistance
k	slope of undamaged cohesive law
k_n	slope of undamaged cohesive law in normal direction
k_t	slope of undamaged cohesive law in tangential direction
L	failure process zone length
l_1	roller distance at beam 1
l_2	roller distance at beam 2
l_c^I	estimated length of the cohesive zone
M_1	moment applied to beam 1
M_2	moment applied to beam 2
M_3	resulting moment
M_x	moment applied to laminate
N_x	force applied to laminate
n_j	outward normal to integral contour
P	wire force
p	integer subscript (path index)
$q_1 - q_4$	points for measuring crack opening
R_b	mid-plane radius
S	curve length
t_c	core thickness
t_f	face thickness
t_s	steel reinforcement thickness
t_o	time of constant velocity
t_n	time at output step n
$u(x)$	opening displacement function inside process zone
v_i	components of displacement vector
$v(t)$	load point speed
v_{tip}	crack tip speed
v_o	load point speed at time of constant velocity (t_o)
v_{12}	sliding speed in process zone
v_{22}	normal opening speed in process zone
W	strain energy density
y_p	y-coordinate for interface between ply $p-1$ and p

Greek Symbols

α_1	slope of line between P_0 and P_1
α_2	slope of line between P_0 and P_2
α_3	slope of line between P_0 and P_3

α_4	slope of line between P_0 and P_4
δ	crack opening
δ^*	pre-crack tip opening
δ_o	opening where damage initiates
δ_1	opening transition point between crack tip and bridging processes
δ_c	opening where cohesive stresses vanish
δ_e	effective displacement
δ_t^*	pre-crack tip tangential opening
δ_n^*	pre-crack tip normal opening
δ_n	normal opening
δ_t	tangential opening
δ_n^c	critical normal displacement
δ_t^c	critical tangential displacement
δ_{12}	shear opening displacement
δ_{22}	normal opening displacement
δ_A	opening displacement at point A
δ_B	opening displacement at point B
δ_x	load point displacement in x-direction
δ_y	load point displacement in y-direction
$\delta(t)$	load point displacement
ϵ_{xx}	strain in x-direction
ϵ_x^0	laminate mid-plane strain
Γ_{tip}	integration path around the crack tip
Γ_{local}	integration path just outside failure process zone
Γ	integration path for J integral
Γ_1-Γ_{10}	integration path pieces
Γ_i	fracture toughness of interface
Γ_m	fracture toughness of matrix material
κ_x^0	laminate mid-plane curvature
κ_b	mid-plane curvature
λ	normalized effective separation measure
$\mathcal{G}_i$	energy release rate along interface
$\mathcal{G}_m$	energy release rate of matrix material (across interface)
ν_c	Poisson's ratio of core
ν_f	Poisson's ratio of face
ν_s	Poisson's ratio of steel
ρ	density
σ	cohesive stress
σ_o	stress at damage initiation
σ_n^o	stress at damage initiation under pure mode I
σ_t^o	stress at damage initiation under pure mode II
σ_i^o	interface strength
σ_m^o	matrix material strength
σ_1	stress at transition point between crack tip and bridging processes

σ_A	stress at point A
σ_B	stress at point B
σ_e	effective stress
σ_{ij}	stress tensor
σ_{max}	max stress in steel layer
$\overline{\sigma}_n$	undamaged normal stress in cohesive element
$\overline{\sigma}_n$	undamaged tangential stress in cohesive element
σ_n	cohesive normal stress
σ_t	cohesive shear stress
σ_{xx}	stress in x-direction
σ_{12}	cohesive shear stress
σ_{22}	cohesive normal stress
θ_1	rotation of beam 1
θ_2	rotation of beam 2
θ_3	mid-plane rotation
φ_δ	phase angle described by opening displacements
φ_J	mode-mixity described by mode I and II damage energies
φ_σ	mode-mixity described by normal and tangential stresses
φ_o	mode-mixity described by normal and tangential stresses at crack tip

Abbreviations

CSM	Chopped Strand Mat
CFM	Continuous Filament Mat
CZM	Cohesive Zone Modelling
DCB	Double Cantilever Beam
DCB-UBM	Double Cantilever Beam loaded by Uneven Bending Moments
DIC	Digital Image Correlation (optical measurement system)
ENF	End Notched Flexure (specimen)
LEFM	Linear Elastic Fracture Mechanics
LSB	Large Scale Bridging
MMB	Mixed-Mode Bending (specimen)
STT	Sandwich Tear Test
TTR	Through-Thickness Reinforcements

Chapter 1

Introduction

1.1 Background and Motivation

During the last couple of decades composite materials have gained enormous popularity in applications where low weight is a design criterion such as in airplanes, wind turbines and high-speed ferries. Composites offer a large potential for high stiffness and strength to weight ratios, however, due to limited knowledge of fracture behaviour and damage tolerance, designs are often made with higher safety factors than corresponding metal structures. Composite laminates are layered materials that contain weak planes between layers where debonds can form and propagate. Testing and analysing composite structures with debonds are the main themes of this thesis.

1.1.1 Damage Tolerance of Sandwich Structures

Sandwich structures consist of strong and stiff faces separated by a light core that acts as a spacer between faces to increase the bending stiffness, and often the faces are made of a composite material adhesively bonded to the core. The functionality of a sandwich structure may be reduced by damage occurring by various failure modes, see e.g. Zenkert (1995). The formation and the propagation of interface debonds are common and critical damage modes needed to be accounted for in the design of sandwich structures. Debonds can arise as a result of defects from production when an area between face and core has not been sufficiently bonded. In use, impact loading, e.g. due to collision with objects, can result in formation or growth of a debond crack. With debonds present the structure might fail under loads significantly lower than those for an intact sandwich structure (Nøkkentved et al. (2005), Berggreen and Simonsen (2005)).

Depending on the loading mode of the crack and the fracture properties of face, core and interface, the debond may propagate in the interface or kink into the adjacent face or core.

As the crack propagates in the core the size of the energy dissipating zone (process zone) is usually small, and crack propagation is successfully modelled by Linear Elastic Fracture Mechanics (LEFM) Bao and Suo (1992). As the crack propagates in the face/core interface or kinks into the laminate, bridging fibres may provide closing tractions between the separating crack surfaces, which may entail a process zone that is large compared with various specimen geometries and LEFM is no longer sufficient. In a cohesive zone model cohesive elements are embedded between bulk elements in a predetermined crack path to mimic the traction behaviour as the material separates. Cohesive elements can be used to simulate fracture with both large and small process zones and this approach is used extensively in the present thesis.

Several studies deal with experiments to determine the fracture toughness of face/core debonds in sandwich structures, e.g. Cantwell and Davies (1996), Li and Carlsson (1999) and Østergaard et al. (2007). However, a complete determination of the interface fracture properties in the form of a cohesive law has not yet been conducted. In Berggreen (2004) LEFM is used to analyse the fracture behaviour of debonded sandwich beams and panels. An approach is adopted where the fracture toughness is initially measured from a Double Cantilever Beam loaded by Uneven Bending Moments (DCB-UBM) and subsequently implemented in a finite element model to predict crack propagation of a face/core debond. In Berggreen (2004) experimental and numerical results correlate well for the light density foam core (80 g/m^3) where the crack tends to propagate in the core next to the interface. For the heavier cores (130 and 200 g/m^3) the crack propagates in the interface with large-scale fibre bridging, and here the finite element model based on LEFM underestimates the loading capacity of the sandwich structure. This thesis aims at using the same methodology as described in Berggreen (2004) with a cohesive zone approach. Thus, both small and large process zones can be accounted for.

1.1.2 High-rate Fracture of Through-thickness Reinforced Laminates

Fracture at high rates can obviously occur if the structure is loaded at high speed, but even at very slow loading rates the structure may enter into a state where a large amount of elastic energy is stored in the structure, which may lead to unstable (fast) crack propagation, see e.g. Li et al. (2005a). For most materials fracture resistance is highly dependent on rate, and there is a need to be able to measure fracture properties from tests conducted over a range of strain rates going from quasi-static loading to fast impact. Several studies deal with measuring high-rate fracture toughness of composite specimens, see Cantwell and Blyton (1999) for a review, but the approach from earlier studies is mainly to describe only one fracture parameter (the fracture toughness) as a function of crack tip speed. Fracture of composites may entail large-scale bridging, which makes LEFM insufficient for characterising the fracture behaviour, and instead a method that describes the full traction-separation relation, such as CZM, is more appropriate. Extracting cohesive laws from experiments during static loading is a highly exploited area, see e.g. Cox and Marshall (1991), Massabò et al. (1998), Sørensen

and Jacobsen (2003), and Li et al. (2006b), whereas the work conducted in the dynamic regime is rather limited and only a single recent study has been found, see Carlberger and Biel (2008). In this thesis the topic of extracting cohesive laws in the dynamic regime is addressed, and the work is meant as an initial step towards developing procedures for predicting high-rate fracture behaviour in the case of large-scale bridging.

Through-thickness reinforcements (TTR) of composite laminates, e.g. z-pins or stitching, are widely used to improve the damage tolerance of composite materials, see e.g. Tomashevskii et al. (1980), Krasnov et al. (1987) and Freitas et al. (1994). Regarding laminates with TTR, separating layers involves fibres being pulled out of a matrix material which shields the crack tip from the loading and increases the fracture energy. Specimens with TTR are considered in this thesis for two main reasons: 1) Laminates with TTR are technologically important, however, not yet well understood, especially in the dynamic regime, and 2) delamination of composites with TTR normally involves large-scale bridging and large process zones, which are adequately modelled by cohesive zones (not by LEFM).

1.2 Objectives and Scope of the Work

The development and design of new composite structures such as aircraft or wind turbine blades involve a large amount of costly tests that are conducted on various scales and complexity levels, see the schematic illustration in Figure 1.1. It is wanted to reduce the amount of large-scale tests and replace them with reliable simulations based on data obtained from small-scale material and fracture tests.

To analyse the fracture behaviour of debonded layered composites fully, at least three different types of failure need to be addressed: 1) Static failure under monotonic loading, 2) dynamic failure where the damage behaviour is affected by inertia and strain rate and 3) long-term cyclic loading and environmental effects, which reduce the durability and carrying capacity of the structure. For many structures a critical design limit is fatigue. However, it is believed that reliability of the methodology needs to be demonstrated for the simpler cases before approaching more advanced issues.

The overall aim of this thesis is to aid the development of a systematic procedure for measuring, predicting and improving the damage tolerance of layered composite structures. Methods for measuring cohesive laws from experiments are addressed by development of a modified DCB sandwich specimen (Chapter 3) and by investigating the dynamic fracture behaviour of a composite end notched flexure specimen (Chapter 6). The experimentally measured cohesive laws are implemented in a finite element model and fracture tests on sandwich beams are used to validate both the measured cohesive laws and the methodology (Chapter 5). Modifications are introduced to the material configuration to address the crack kinking behaviour and to improve the damage tolerance by modifying the interface design (Chapter 4).

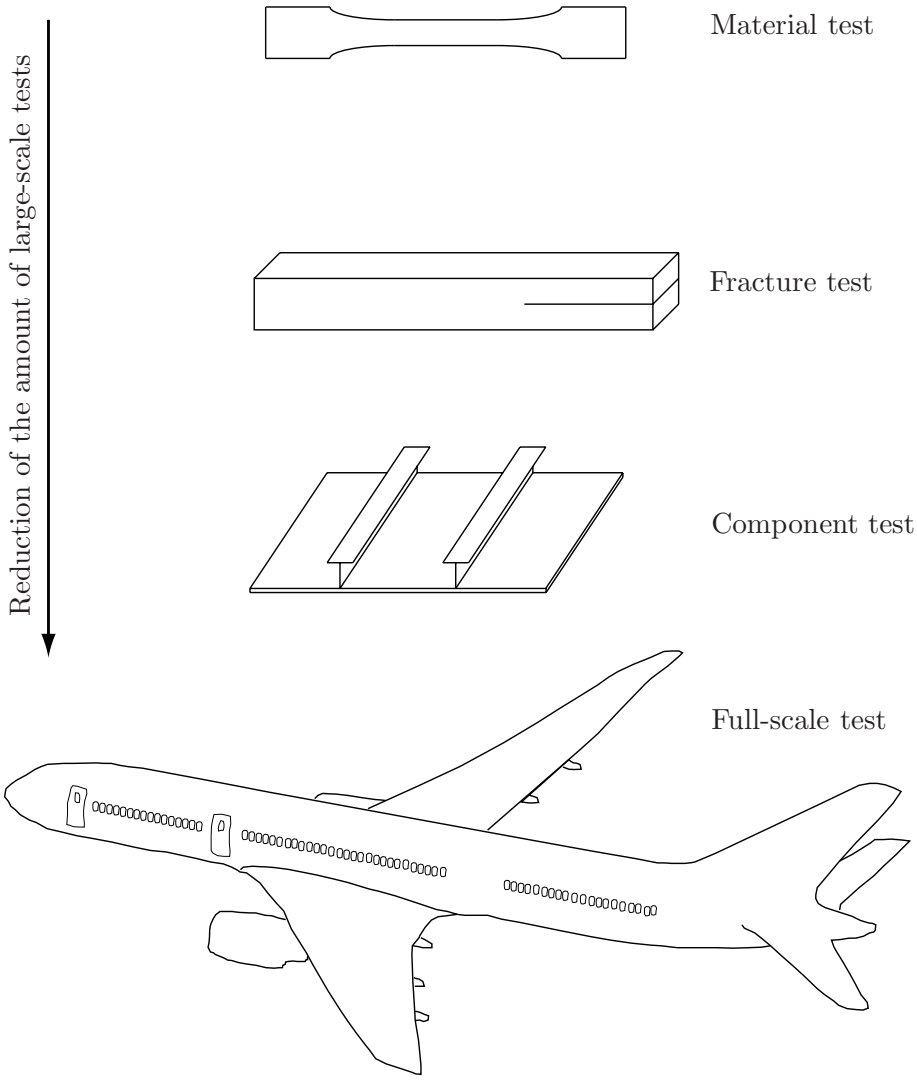

Figure 1.1: Schematic illustration of various test specimens used in the product development phase.

1.3 Overview of the Thesis

The key areas of novelty in this thesis are described briefly by the following points.

- Based on classical laminate theory the J integral equation is derived for a multilayered double cantilever beam loaded by bending moments.
- By use of a digital image correlation (DIC) system the crack opening parameters of a cracked sandwich specimen are obtained.
- Adhering stiff steel layers to relatively compliant composite faces reduces unwanted large deflections and removes the need for accurate measurements of the face properties.
- The crack kinking behaviour of a debonded sandwich specimen is investigated for various mixed-mode loadings and a thin woven laminate is inserted adjacent to the load-carrying laminate reducing the tendency for the crack to deflect into the load-carrying laminate.
- By use of a standard finite element package, crack growth of a debond damaged sandwich structure is predicted using previously measured cohesive laws.

The following is a short description of each chapter in the thesis.

Chapter 2: The basic theory behind Cohesive Zone Modelling (CZM) and finite element implementation is described. Various mixed-mode cohesive zone formulations from the literature are described, and the influence of the shape of the cohesive law on the fracture behaviour is discussed.

Chapter 3: This chapter describes the development and analysis of a modified sandwich DCB specimen loaded by bending moments. The modifications entail stiffening of the thin composite faces with steel bars and multiple effects of the stiffening are investigated. The J integral is calculated and related to the opening of the pre-crack tip and thus cohesive laws are extracted. Results for two sandwich interface configurations are described and discussed. This chapter is an extension of the work published in Lundsgaard-Larsen et al. (2008).

Chapter 4: This study deals with kinking of a face/core interface crack into the adjacent face or core. The effect of the mode-mixity on the crack propagation path is investigated, and the influence of material configurations on the kinking behaviour and following steady state fracture resistance is examined. The effect of embedding a woven layer in the laminate to prevent crack kinking is further considered.

Chapter 5: Large-scale tests and simulations of crack propagation in sandwich beams during development of large-scale bridging are conducted and numerical/experimental results are compared. The cohesive laws measured in Chapter 3 are used as input for the finite element

model. The aim of the chapter is to validate the procedure for predicting the fracture behaviour using CZM.

Chapter 6: A purely numerical study is conducted on a composite End Notched Flexure (ENF) specimen loaded at various loading rates taking inertia effects into consideration. The aim of the study is to increase the knowledge of high-rate fracture behaviour as an initial step towards deducing rate dependent cohesive laws from dynamic fracture tests.

Chapter 7: This chapter presents the conclusions and suggestions for future work.

Chapter 2

Cohesive Zone Modelling

2.1 Background and Theory

The concept of cohesive zones was introduced by Barenblatt (1959) and Dugdale (1960) and the early numerical implementation conducted by Petersson (1981), Stigh (1987) and Needleman (1987). In recent years, Cohesive Zone Modelling (CZM) has gained renewed popularity as a powerful tool for representing fracture processes. CZM is particulary useful where the process zone is large compared with relevant specimen dimensions, e.g. the crack length, since then LEFM does not apply. The cohesive stresses between layers can represent several fracture mechanisms such as fibre bridging, plasticity and friction smeared together, and as the fracture process incorporates several cohesive mechanisms, the shape of the cohesive law will reflect this. A cohesive law representing both crack tip fracture and large-scale bridging in the crack wake is schematically illustrated in Figure 2.1.

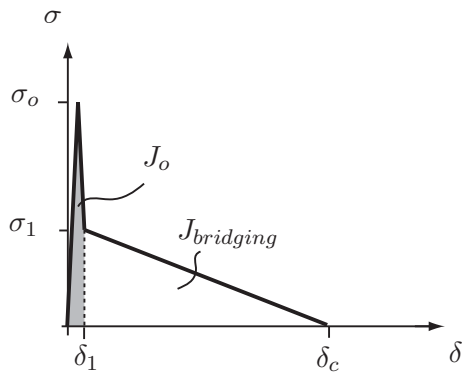

Figure 2.1: Schematic illustration of a cohesive law with two fracture mechanisms: The crack tip separation and large-scale bridging in the crack wake.

As regards Figure 2.1, σ is the traction between cracked faces, δ is the separation, σ_o is the maximum stress at the crack tip, σ_1 is the stress transferred by bridging fibres behind

the crack tip at separation δ_1, and δ_c is the critical displacement where stresses vanish. J_o and $J_{bridging}$ correspond to energies dissipated near the crack tip and due to bridging fibres respectively. As for most finite element formulations of cohesive laws the illustration in Figure 2.1 has zero stress for $\delta = 0$, and subsequently the stress increases with the initial slope k. To avoid numerical instabilities when solving a finite element model, it is important that a change in stress is always associated with a change in deformation, and therefore the stress is increased from zero in the numerical implementation. The initial stiffness k should be put to a high number compared to the elasticity of the specimen, in order to mimic perfect adhesion of the intact part of the specimen. This will be further described later.

If $\delta_1 \ll a$ where a represents various relevant dimensions, e.g. the crack length, the cohesive law in Figure 2.1 is equivalent to a bridging law, where the tip process is represented by LEFM and the long-range tractions are simulated with cohesive elements, see Carpinteri and Massabò (1996).

2.1.1 Experiments to Extract Cohesive Laws

Modelling of fracture using a cohesive zone model consists of two parts: (1) The cohesive law may be derived from either micromechanics or mechanical tests, and (2) subsequently applied to computing the load-carrying capacity of a component. Various methods exist for extracting cohesive laws from fracture mechanical tests and the author has chosen to categorise the different approaches into three groups: (1) direct measurements, (2) indirect measurements and (3) J integral approach. The three different concepts are explained below and some examples from the literature are given.

(1) Direct measurements: This method is typically based on a test where the material or interface is being directly pulled apart in a direction corresponding to either mode I, mode II or mixed-mode. Often the specimen contains no notches and it is assumed that the stress distribution is uniform and given as the applied load divided by the original ligament area, while the material separation is measured by an extensometer or by subtracting the elastic deformation from the crosshead displacement.

This approach was used by Cox et al. (1996) for 3-D woven graphite/epoxy composites, by Li et al. (2005b) for bonding of glass fibre composites, and by Liu et al. (2007) for z-pin reinforced laminates. See the schematic illustration of the method in Figure 2.2.

The advantage of the direct method is that the cohesive law is measured without time-consuming finite element modelling and/or J integral calculations. Since there is no pre-notch and uniform stress distribution is assumed, it is straightforward to read the peak stress from the load-displacement curve. However, often the assumption of a uniform stress distribution is doubtful, and stress concentrations near edges or imperfections might lead to misinterpretations of the results. Furthermore, the specimen design has to be carefully considered to avoid dynamic crack propagation behaviour, since in the absence of a notch

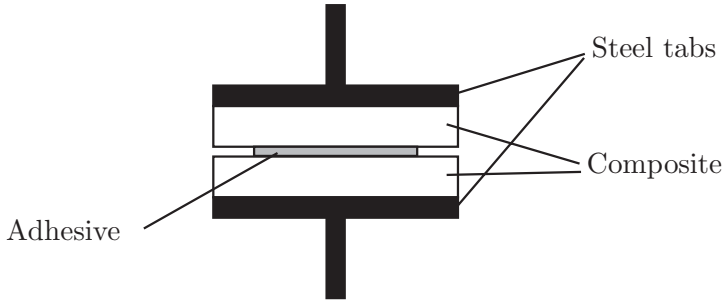

Figure 2.2: Setup for direct measurement of an adhesive layer between composite plates.

the elastic energy in the tensile specimen can more easily exceed the critical energy necessary to propagate a crack through the entire ligament.

(2) Indirect measurements: In this method experimental results of a fracture specimen are compared to numerical results, which are coupled with an assumed cohesive law. By varying the cohesive law until experimental and numerical results agree the cohesive law is determined. Some examples of fracture specimens used for this approach are Double Cantilever Beam (DCB) for mode I, End Notched Flexure specimen (ENF) for mode II and Mixed-Mode Bending (MMB) for mixed-mode, see Figure 2.3.

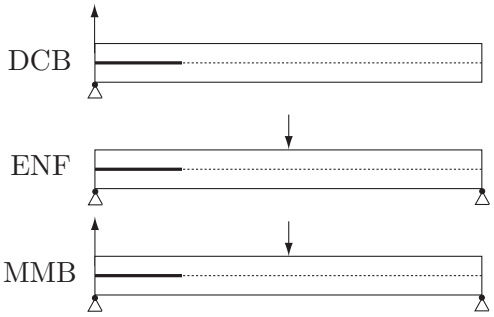

Figure 2.3: Schematic illustration of common fracture mechanical test methods used for indirect measurements of traction-separation relations in mode I (DCB), mode II (ENF) and mixed-mode (MMB).

Various parameters define the cohesive law, such as e.g. area below curve J_c, peak stress σ_o, and critical displacement δ_c, see Figure 2.1, however, not all parameters are easily extracted from the experimental results. The area of the cohesive law is relatively simple to extract, since it clearly affects the load-displacement curve. The area may be determined as the crack length increases and the load-displacement curve approaches that for the case of LEFM, for which analytical expressions exist, see example in Section 2.2.6. It is, however, more difficult to determine the shape of the cohesive law, since this is only rarely reflected clearly in the test results.

Various results from the experiments can be exploited to determine the cohesive law. Usually, the load-displacement curve is used as in e.g. Li et al. (2006b), whereas in some cases the

crack opening profile near the process zone is used, see Cox and Marshall (1991) and Massabò et al. (1998). In Massabò et al. (1998) mode II cohesive laws are extracted from delamination of a stitched carbon/epoxy laminate by comparing a CZM to experiments, using both the load-displacement relations and the crack opening profile in the process zone.

(3) J integral approach: This method utilises the connection between the J integral of the loaded specimen and the bridging forces in the process zone. As described in Sørensen and Jacobsen (1998) the cohesive law can be found by differentiating the fracture resistance J_R with respect to the opening of the pre-crack tip. This principle has been used for steel plates bonded by adhesive layers, see Andersson and Stigh (2004), Leffler et al. (2007) and Högberg and Stigh (2006) for mode I, mode II and mixed-mode loading, respectively. Sørensen et al. (2006) uses the J integral approach to measure mixed-mode cohesive laws for layered composites by means of a test-rig applying Uneven Bending Moments to a DCB specimen (DCB-UBM). The advantage of loading the specimen by pure moments is that the J integral becomes independent of the crack length and can be calculated only from the geometry, elastic properties and applied moments. Chapter 3 of this thesis is concerned with extracting mixed-mode cohesive laws from a face/core sandwich interface by calculating the J integral for a sandwich specimen loaded by pure bending moments.

All known experimental methods for estimating cohesive laws are connected with some degree of uncertainty. Generally, experiments described in (2) are appropriate for determining the area below the cohesive law, whereas experiments in (1) are appropriate for determining the peak stress and the critical length. The J integral approach in (3) is suitable for finding the area below the cohesive law and may also be used to find the detailed shape, if the opening displacement of the pre-crack tip is measured accurately enough. This will be described further in Chapter 3. Some important questions arise:

1. Which parameters of the cohesive law are controlling the fracture behaviour?
2. To what detail must the shape of the cohesive law be known?
3. Which experiments will be sufficient to determine the cohesive law at the required level of detail?

The answers to these questions depend on the circumstances of the individual cases, as will be further discussed in the following section. The cohesive law should be determined with a level of detail sufficient to obtain satisfying fracture predictions for the analyzed structures.

2.1.2 Length Scales

As described in Parmigiani and Thouless (2006) CZM combines two traditional views of fracture criteria being either stress-based (Inglis (1913)) or toughness-based as in LEFM (Griffith (1920)). By varying the properties of the cohesive law it is possible to identify

three different regimes: One where the fracture toughness controls fracture, one where peak stress controls fracture and one intermediate where both parameters are important. The importance of the toughness parameter relative to the strength can be estimated from a length scale Bao and Suo (1992)

$$a_s^I = \delta_c \overline{E}/\sigma_o \tag{2.1}$$

where δ_c and σ_o are parameters of the cohesive law, see Figure 2.1, and $\overline{E}$ is the plane stress/strain Young's modulus of the specimen material. a_s^I is a material property, since the cohesive law and Young's modulus are material properties. If the length parameter is small compared to a characteristic length of the structure a, i.e. the crack length or hole radius, LEFM prevails and crack propagation will be in a brittle manner. By increasing a_s^I/a crack propagation becomes more ductile and the peak stress value of the cohesive law will become increasingly important.

The characteristic length scale a_s^I described above is closely related to the cohesive zone size. As described by Bao and Suo (1992) and Yang and Cox (2005), in an infinite body under uniform remote loading (small-scale bridging limit) the order of magnitude estimate of the cohesive zone length l_c^I is given by

$$l_c^I = a_s^I \tag{2.2}$$

In a slender mode I loaded body of thickness $2h$ and with a crack in the centre, the characteristic length becomes dependent on the beam thickness, and l_c^I is estimated to be as follows (ignoring numerical factors close to unity):

$$l_c^I = (a_s^I)^{1/4} h^{3/4} \tag{2.3}$$

Note that the process zone size increases with increasing thickness h in (2.3), which is consistent with typical R-curve behaviour where the crack length to reach steady state increases with specimen thickness. Regarding a fracture mechanical test, the ratio a_s^I/a indicates the sensitivity of the shape of the cohesive law on the fracture behaviour and the level of detail (about the cohesive law) that (potentially) can be derived from the experimental results.

2.1.3 Idealised Cohesive Laws

The cohesive law may be measured from experiments or predicted from micromechanical models. Often the micromechanical model is beneficial to increase the understanding regarding various fracture mechanisms and to explain the effect of altering various properties on the fracture behaviour. Some examples of micromechanical models of fracture mechanisms are fibre bridging in Spearing and Evans (1992), fibre pull-out in Hutchinson and Jensen (1990) and kink band propagation in Budiansky et al. (1998).

In CZM all fracture mechanisms in and around the crack tip are gathered in a constitutive relation between traction and separation of the fracture surfaces. Often the detailed

traction-separation behaviour is fitted with idealised shapes used to model fracture. These are convenient to formulate and implement and in many cases they provide sufficient information to predict fracture accurately. The purpose of this section is to describe some of the shapes used in earlier models and review a study on the influence of the shape on fracture behaviour. It is important to acknowledge that the sensitivity to the shape depends on the material length scales and specimen geometry, as described above.

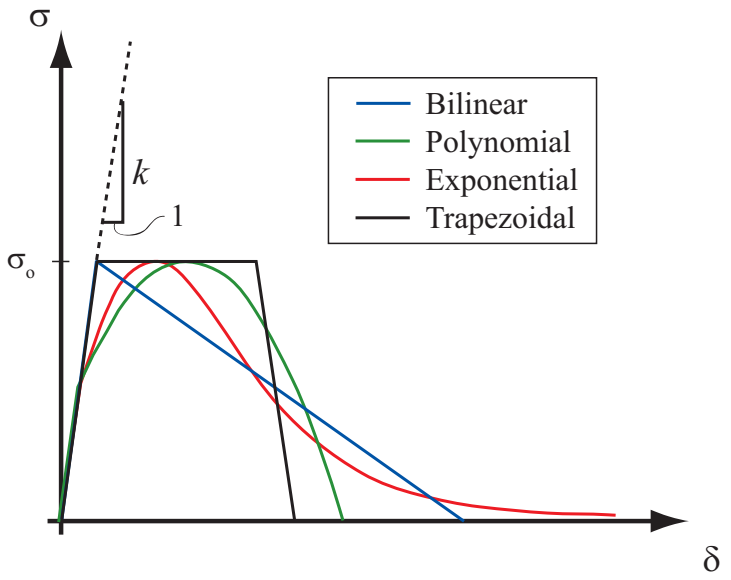

Figure 2.4: Idealised cohesive laws used for a comparison study in Alfano (2006).

The following four idealized shapes are considered in the present study: (1) bilinear, (2) polynomial, (3) exponential or (4) trapezoidal, see Figure 2.4. The *bilinear* shape is the simplest in the sense that it can be described by only two parameters (in addition to the initial elastic stiffness k) e.g. critical stress σ_o and fracture energy J_c. This shape has been used for modelling delamination of composites with through-thickness reinforcements, e.g. Dantuluri et al. (2007), mode I fracture of braided carbon fibre composites in Xie et al. (2006) and mixed-mode delamination of composites in Camanho et al. (2003). Li et al. (2005b) demonstrated that the bilinear shape is not always sufficient to describe fracture of an adhesively bonded composite specimen. The remedy suggested is to include an extra tip on the original bilinear cohesive law with a higher critical stress denominated the intrinsic cohesive strength. A *polynomial* shape was used e.g. to model decohesion of fibre/matrix interfaces by Tvergaard (1990) and face/core delamination in foam-cored sandwich structures by El-Sayed and Sridharan (2002). In addition Blackman et al. (2003) used a cubic form to study fracture of fibre composites and adhesively bonded joints. In contrast to the bilinear shape the polynomial is differentiable, which may be an advantage in the finite element implementation. The *exponential* shape was used by Xu and Needleman (1993) to model decohesion of hard particles in a matrix. The same formulation was later revised by van den Bosch et al. (2006) to make it more adequate for mixed-mode fracture. The

trapezoidal cohesive law was proposed by Tvergaard and Hutchinson (1992) and later used extensively, e.g. for modelling fracture of composites, Yang and Cox (2005), and buckling driven delamination in sandwich columns, Østergaard (2008).

A numerical comparison study of the four mentioned shapes was conducted by Alfano (2006) for different fracture specimens loaded in pure mode I or II. In the study the same initial stiffness k, the same peak value of the traction σ_o and the same fracture energy J_c were used for all four shapes, see Figure 2.4. Load-displacement curves for an aluminium DCB and a steel compact specimen, see Figure 2.5, were determined. The DCB specimen illustrated in Figure 2.5 is assumed to have the elastic properties of aluminium, and the compact specimen the properties of steel. The material and interface properties are listed in Table 2.1.

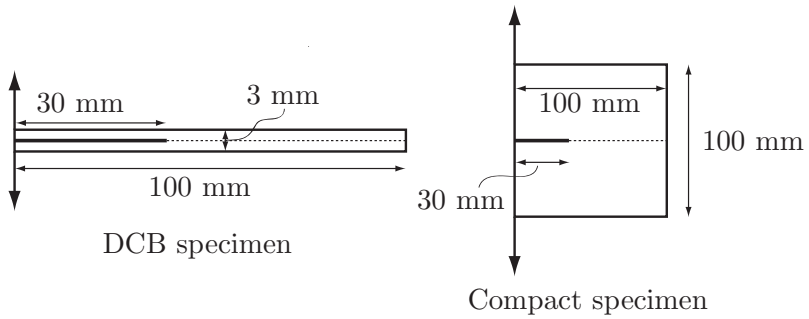

Figure 2.5: Geometry of two simulated test specimens used in Alfano (2006). The two specimens are scaled differently in the illustration.

Aluminium (DCB)	$E = 70$ GPa; $\nu = 0.3$
Steel (compact specimen)	$E = 210$ GPa; $\nu = 0.2$
Interface	$J_c = 500$ J/m^2; $\sigma_o = 30$ MPa; $k = 10^{13}$ N/m^3

Table 2.1: Material elastic properties and interface properties defining the cohesive law from simulations in Alfano (2006).

Results from Alfano (2006) show that the geometry of the fracture specimens decides whether or not the shape of the softening curve affects the load-displacement curve. For the aluminium DCB, results were practically independent of the shape, whereas for the steel compact specimen a difference up to 15% was recorded. The influence was however significant only in the vicinity of the maximum applied load.

In the following results obtained in Alfano (2006) are supported by conducting a simple analysis of the two specimens using Eqs. (2.2) and (2.3). The process zone size for the steel compact specimen and the aluminium DCB is estimated: For the steel compact specimen the process zone size just before the crack propagates is equal to the length scale within order of unity, which according to the cohesive law is $a_s^I = 77$ mm. For the aluminium DCB specimen the length scale is $a_s^I = 26$ mm, but due to the slenderness of the specimen the process zone size decreases and is from Eq. (2.3) estimated to be 3 mm (within order of unity). The size of the process zone of the aluminium specimen is relatively small compared

to the crack length of 30 mm, whereas for the steel compact specimen the process zone is relatively large. Therefore the load-displacement curve of the steel compact specimen is much more sensitive to the shape of the cohesive law compared to the aluminium DCB.

In addition to the study by Alfano (2006), it is relevant to consider Jacobsen and Sørensen (2001) where the influence of the shape of the cohesive law on measured R-curves is investigated numerically. Furthermore, Gu (1995) considers the effect of the shape of the cohesive law on the loading capacity for various notch sizes normalised by the length scale described by Eq. (2.1).

2.1.4 Mixed-mode Behavior

Up to this point the description of cohesive laws has been limited to pure mode deformation (mode I or mode II). The fracture mechanisms that the cohesive law represents are often mode dependent, and in general a cohesive law should be defined for both normal and shear tractions as a function of both normal and shear openings. Mixed-mode cohesive law formulations for such cases have been proposed previously, and some of them will be presented in the following.

Mixed-mode cohesive law formulations are either coupled or uncoupled, and for the latter the tractions in both normal and tangential directions depend only on displacement in the same direction. Conversely, in a coupled formulation both normal and tangential tractions depend on both normal and tangential opening displacements. Examples of uncoupled and coupled mixed-mode formulations from the literature are given in the following.

Yang and Thouless (2001) proposed an *uncoupled* formulation combined with the following mixed-mode fracture criteria:

$$\frac{J_I}{J_I^c} + \frac{J_{II}}{J_{II}^c} = 1 \tag{2.4}$$

where J_I^c and J_{II}^c are the work of separation for pure modes, and the energy dissipation associated with mode I and mode II is given by

$$J_I = \int_0^{\delta_n} \sigma_n(\delta_n) d\delta_n, \qquad J_{II} = \int_0^{\delta_t} \sigma_t(\delta_t) d\delta_t \tag{2.5}$$

As the criteria in Eq. (2.4) is fulfilled the stresses in the normal and tangential directions drop to zero. For a mixed-mode loading case the traction-separation behaviour in the normal and tangential directions is schematically illustrated in Figure 2.6.

The same formulation was adopted by Li et al. (2006b) and Xie and Waas (2006), which have shown excellent agreement between model predictions and experiments regarding fracture of adhesively bonded composites.

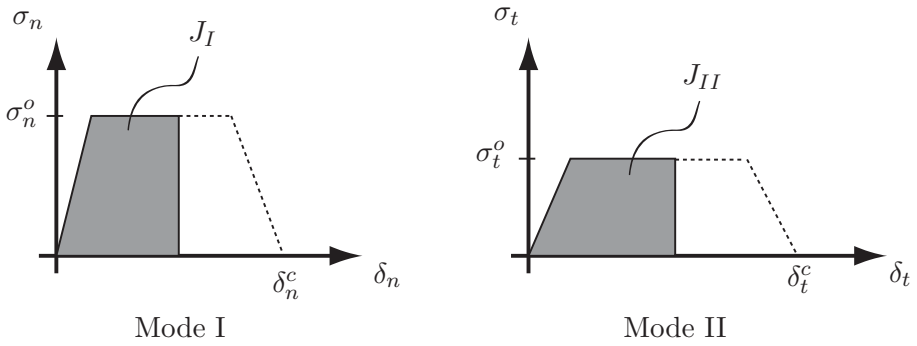

Figure 2.6: Cohesive law formulation from Yang and Thouless (2001). The dotted lines represent the traction-separation behaviour in pure mode I and II, and the shaded areas are the mixed-mode work of the cohesive tractions.

Tvergaard and Hutchinson (1993) suggested a *coupled* formulation where the stiffness degradation depends on a normalised effective separation measure:

$$\lambda = \sqrt{\left(\frac{\delta_n}{\delta_n^c}\right)^2 + \left(\frac{\delta_t}{\delta_t^c}\right)^2} \tag{2.6}$$

where δ_n and δ_n^c, and δ_t and δ_t^c are the separations and critical separation lengths in the normal and tangential directions n and t. The tractions in the normal and tangential directions are given by

$$\sigma_n = \frac{\sigma(\lambda)}{\lambda}\frac{\delta_n}{\delta_n^c}, \qquad \sigma_t = \frac{\sigma(\lambda)}{\lambda}\frac{\delta_n^c}{\delta_t^c}\frac{\delta_t}{\delta_t^c} \tag{2.7}$$

where the generalised traction function $\sigma(\lambda)$ is illustrated in Figure 2.7.

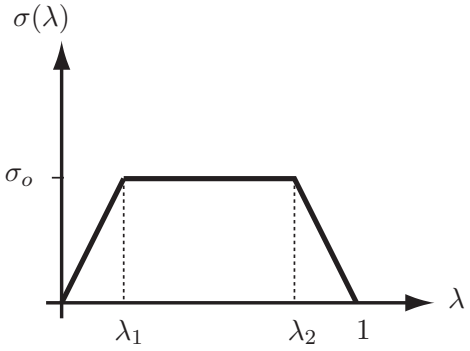

Figure 2.7: The traction as a function of normalised displacement λ in Tvergaard and Hutchinson (1993).

In the following, the uncoupled approach as described in Yang and Thouless (2001) with the overall failure envelope Eq. (2.4) is compared with the coupled cohesive law formulation

described in Tvergaard and Hutchinson (1993). The chosen cohesive law is trapezoidal with $\lambda_1 = 0.003$ and $\lambda_2 = 0.99$, see Figure 2.7. The mixed-mode cohesive law formulation is explored by assuming that the opening displacement is increased in a fixed direction with the angle φ_δ to the normal direction, see Figure 2.8. The effective (resultant) displacement is given by $\delta_e = \sqrt{\delta_n^2 + \delta_t^2}$ and the effective stress by $\sigma_e = \sqrt{\sigma_n^2 + \sigma_t^2}$.

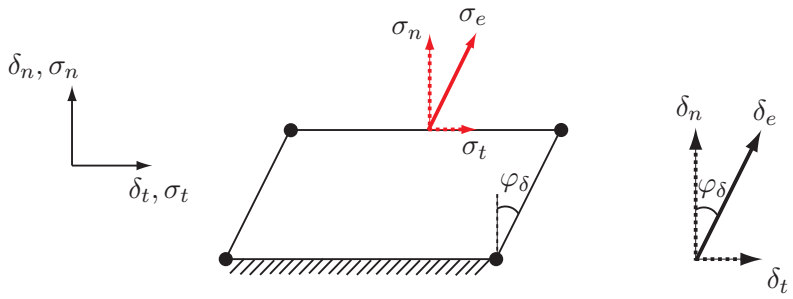

Figure 2.8: Loading of a single cohesive element in a fixed direction φ relative to the normal direction. The normal and shear stresses in the element and the corresponding displacements are illustrated.

The mixed-mode traction-displacement relations are illustrated in Figures 2.9 and 2.10 for the formulation used in Yang and Thouless (2001) and Tvergaard and Hutchinson (1993), respectively (identical properties are assumed for pure mode I and II conditions, i.e. $J_I^c = J_{II}^c$, $\delta_I^c = \delta_{II}^c$ etc.). The mixed-mode cohesive law is illustrated in the full mode-mixity range by plotting the phase angle of $\varphi_\delta = \{0, 10, 20, ..., 90\}$.

Consider the subplot in Figure 2.9 (a). It is seen that the traction in the normal direction is unaffected by the displacement in the tangential direction, and for mixed-mode cases the critical length (where tractions vanish) is $\delta_e = 1/\sqrt{2}\delta_c$. The equivalent is observed for the tangential direction in Figure 2.9 subplot (b). In subplot (c) the effective (resultant) stresses for mixed-mode loadings are a factor of $\sqrt{1^2 + 1^2} = \sqrt{2}$ higher than stresses in pure mode loading, and for that reason the energy increases a factor of $\sqrt{2}$ faster compared to the pure mode case, see subplot (d).

The results from the coupled mixed-mode formulation of Tvergaard and Hutchinson (1993) are illustrated in Figure 2.10 where the normal stresses depend on the tangential displacements and vice versa, see subplots (a) and (b). If e.g. the opening displacement is dominated by shear the shear tractions are larger than the normal tractions. The equivalent stress in subplot (c) is the same for pure and mixed-mode loadings, and in contrast to the uncoupled case shown in Figure 2.9 failure occurs at an effective displacement of $\delta_e = \delta_c$ for all loading directions, see Figure 2.10 subplot (d).

The choice whether to assume uncoupled or coupled behaviour depends on several circumstances. It is intuitive that for many fracture scenarios an initial loading and separation in one direction will weaken the interface and affect the traction-separation behaviour in the other direction, which suggests that a coupled behaviour is appropriate. The question is

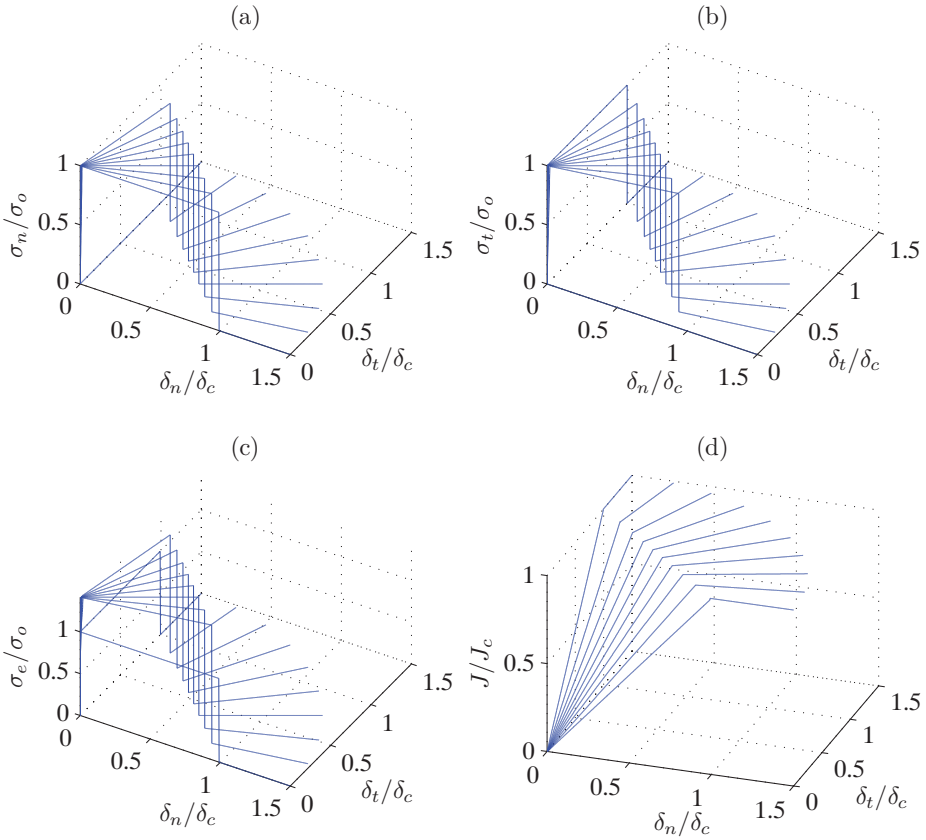

Figure 2.9: Mixed-mode behaviour of cohesive law formulation of Yang and Thouless (2001) with identical properties in mode I and II. (a) and (b) are normal and tangential tractions normalised by the critical stress σ_o, (c) represents the effective (resultant) tractions normalised by σ_o, and (d) illustrates the energy dissipation normalised by the pure mode critical energy.

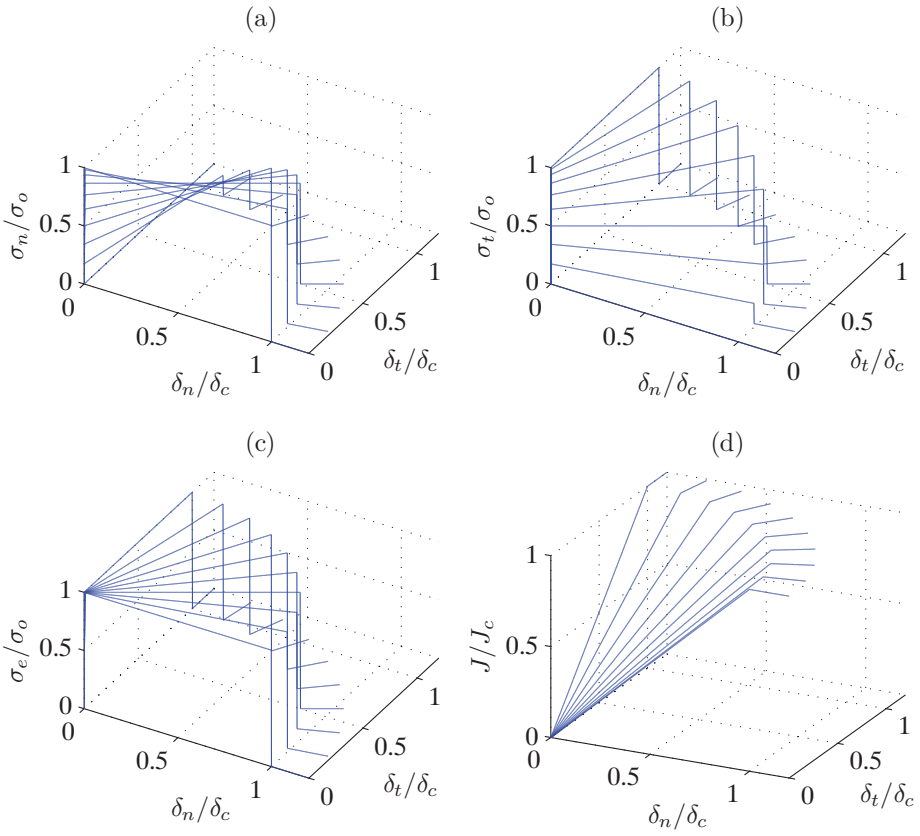

Figure 2.10: Mixed-mode behaviour of cohesive law formulation of Tvergaard and Hutchinson (1993) with identical properties in mode I and II. (a) and (b) are normal and tangential tractions normalised by the critical stress σ_o, (c) represents the effective (resultant) tractions normalised by σ_o, and (d) illustrates the energy dissipation normalised by the pure mode critical energy.

then which coupling to assume. It is difficult and time-consuming to conduct tests for all mixed-mode cases, and often only results from pure mode I and II experiments are used to predict mixed-mode fracture. For fracture of composite materials the fracture mechanisms that affect the traction-separation behaviour are different for various mode-mixities, and it is therefore not in general reasonable to assume that the mixed-mode traction-separation behaviour can be predicted from the pure modes.

Until now, this chapter has been devoted to giving an overview of methods used within cohesive zone modelling. Various test methods for measuring cohesive laws have been categorised and described and the typical advantages and disadvantages of the various methods have been mentioned. The importance of the shape of the cohesive law on the fracture behaviour has been discussed through length scales and various idealised cohesive laws from the literature. Two frequently used mixed-mode formulations, one coupled and the other uncoupled, have been described and the mixed-mode traction-separation behaviour of the two formulations have been illustrated and compared.

The remaining part of this chapter describes the procedure for setting up a finite element model for analysing specimens by use of CZM. Initially, some general finite element assumptions are mentioned followed by the mixed-mode cohesive law formulation and validation of the model through comparison with an example from the literature.

2.2 Finite Element Implementation

The following describes procedures and assumptions related to creating a cohesive zone finite element model.

2.2.1 General

A 2-D plane strain finite element model is generated and solved in the commercial finite element program ABAQUS version 6.6. The assumption of plane strain is used since (regarding the 3-D stress/strain situation in the specimen) the material far from the crack tip exposed to low strains may limit the tendency of the material near the crack tip to expand or contract in the width direction. The model is solved in the Explicit domain and includes inertia effects, so that it is possible to model dynamic behaviour as the model is exposed to high loading rates (see Chapter 6). If a quasi-static solution is desired, the loading speed is reduced to a level where dynamic effects are insignificant, i.e. $E_{kin}/E_{el} < 0.01$, where E_{kin} is the total kinetic energy in the finite element model and E_{el} is the total elastic energy. The inclusion of inertia in the quasi-static model has some advantages, since without inertia it can be necessary to include viscous damping of the cohesive elements in order to archieve convergence, and care should be taken how this affects the solution, see Abaqus (2006). In this thesis the model is used for different geometries and loading conditions, e.g.

End Notched Flexure (ENF) specimens and sandwich DCB-UBM specimens, which will be described later. The following is an overall description of common issues for the models.

The crack path is predetermined and cohesive elements are embedded between the continuum elements along the crack path, e.g. a sandwich interface. No cohesive elements are embedded in the part of the interface that constitutes the pre-crack. In addition to the cohesive elements a frictionless contact interaction between the two bulk parts is formulated in a penalty master-slave configuration to prevent interpenetration of the cracked surfaces, see Figure 2.11. As the nodes on the slave surface seek to penetrate the master surface, reaction forces are applied to the slave nodes, to oppose the penetration, while equal and opposite forces act on the master surface at the contact point, see Abaqus (2006).

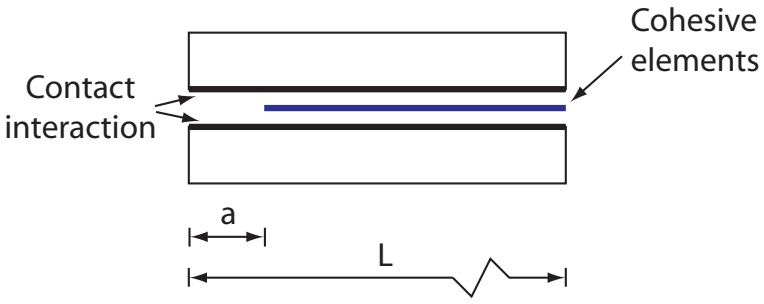

Figure 2.11: Exploded schematic view of the DCB specimen in finite element model. Zero-thickness cohesive elements constitute bonding between beams, and contact interaction prevents interpenetration.

Two element types are used and in ABAQUS they are denoted CPE4R and COH2D4: The CPE4R is a plane strain four-node bilinear element with eight degrees of freedom and reduced integration, which is used to model the continuum material. To construct a mesh refinement near the interface, the element is also used in a three-node version, where two of the four nodes are joined. The COH2D4 element is a four-node linear cohesive element, with constitutive relations described by a traction separation law, see Section 2.2.3.

2.2.2 Mesh Considerations

The mesh is mainly uniform, though refined near the interface, to obtain a more accurate representation of the cohesive zone and contact forces. The mesh refinement near the interface is illustrated in Figure 2.12.

The length of the cohesive elements in the interface is the same as adjacent bulk elements and nodes are coincident. The appropriate mesh size depends on the application, and the cohesive zone should span several cohesive elements in order to get an accurate representation of the traction variation. Furthermore, a sufficient number of bulk elements should be present through the beam thickness in order to represent e.g. bending deformation accurately. A

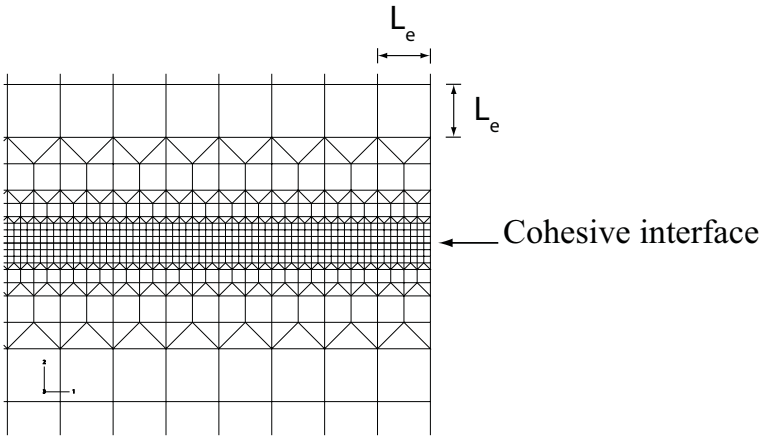

Figure 2.12: Mesh refinement of bulk elements near cohesive interface. The ratio between the side lengths of the largest and the smallest continuum element used in the model is typically 8.

convergence analysis focusing on both bulk and cohesive element size is conducted to ensure that the influence of mesh size on the results is typically less than 2%.

In order to reduce the necessary iterative work when seeking mesh convergence it is useful to have a predetermined estimate of the cohesive zone size. An estimate within order of magnitude can be found for the small-scale bridging limit in Eq. (2.2), and as the slenderness of the specimen affects the process zone size, Eq. (2.3) is to be used instead, see Bao and Suo (1992). When the cohesive law consists of multiple fracture processes, e.g. as illustrated in Figure 2.1 where the cohesive law is a mixture of crack tip processes and large-scale bridging tractions, the process zone size should be considered for each branch individually. The conservative cohesive element size is then estimated from the lesser of the two lengths, see Yang and Cox (2005).

2.2.3 Implementing Cohesive Laws in ABAQUS

The available cohesive law formulation in ABAQUS assumes initial linear elastic behaviour, followed by initiation and subsequent evolution of damage where the stiffness of the element is degraded according to a specific damage evolution law. The cohesive element in ABAQUS exists in a 2-D and 3-D version but since only 2-D analyses are conducted in this thesis, the kinematics of the element is only described in the two plane directions (normal and tangential). The undamaged constitutive relation between traction and separation is given by

$$\left\{ \begin{array}{c} \overline{\sigma}_n \\ \overline{\sigma}_t \end{array} \right\} = \left[\begin{array}{cc} k_n & k_{nt} \\ k_{tn} & k_t \end{array} \right] \left\{ \begin{array}{c} \delta_n \\ \delta_t \end{array} \right\} \tag{2.8}$$

where $\overline{\sigma}_i$ is the undamaged stresses and δ_i is the opening displacements, both in direction i. As illustrated in Figure 2.1 the cohesive law has an initial steep linear part, which is governed by the stiffness terms in Eq. (2.8). If the stiffness is too small, this will add compliance to the undamaged model affecting the solution. Conversely if the stiffness terms are very large, numerical problems appear, and the solution will not converge. The off-diagonal stiffness terms k_{nt} and k_{tn} are assumed equal to zero and $k_n = k_t$ is put to a sufficiently high number found from a convergence analysis for each of the individual cases considered. A quadratic stress criterion is used as the damage initiation envelope which defines the transition where damage initiates. The criterion is similar to the one described in Tvergaard and Hutchinson (1993):

$$\left(\frac{\langle\sigma_n\rangle}{\sigma_n^o}\right)^2 + \left(\frac{\sigma_t}{\sigma_t^o}\right)^2 = 1 \tag{2.9}$$

where σ_n^o and σ_t^o are the critical stresses at pure mode damage initiation in the normal and tangential directions. The quantity within the Macaulay bracket $\langle\rangle$ is put to zero when negative (signifies that a pure compressive deformation does not contribute to damage). Once damage has initiated, the damage evolution is described as a stiffness degradation by a variable D:

$$\sigma_n = \begin{cases} (1-D)\overline{\sigma}_n, & \overline{\sigma}_n \geq 0 \\ \overline{\sigma}_n, & \overline{\sigma}_n < 0 \end{cases} \tag{2.10}$$

$$\sigma_t = (1-D)\overline{\sigma}_t \tag{2.11}$$

The scalar variable D represents the overall damage in the material and is used to describe stiffness degradation in both normal and tangential directions. Before (and at) the point of damage initiation the damage variable D equals zero while upon further loading D increases monotonically to one.

A schematic illustration of a triangular traction-separation law is given in Figure 2.13. After damage initiation σ decreases towards zero according to the damage variable D. If unloading occurs at some point B after damage initiation, the tractions are reduced linearly with displacement toward the starting point A. As the element is reloaded, the same path is followed back to point B and the damage variable D remains constant during unloading and reloading.

Damage evolution in a combination of normal and shear deformation is described by an effective displacement parameter, see Camanho et al. (2003).

$$\delta_e = \sqrt{\langle\delta_n\rangle^2 + \delta_t^2} \tag{2.12}$$

The damage variable D is described as a function of the effective displacement and a mode-mixity measure $D = D(\delta_e, \varphi)$ in a tabbing array, and the mode-mixity is either energy-based

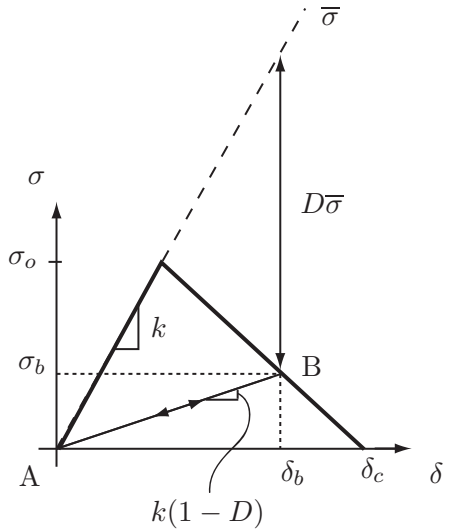

Figure 2.13: Traction-separation relation for linear softening behaviour. Unloading occurs from point B along a straight line toward 0,0 (point A) and reloading along the same path (from A to B).

$\varphi = \varphi_J$ or stress based $\varphi = \varphi_\sigma$, both depending on the full traction-separation history of the cohesive element. The energy based mode-mixity is defined as the ratio between shear-based damage energy and total damage energy described independently for each cohesive element

$$\varphi_J = \frac{J_{II}}{(J_I + J_{II})} \tag{2.13}$$

where J_I and J_{II} are the energies dissipated due to mode I and II deformation given by (2.5).

The stress based mode-mixity is found from

$$\varphi_\sigma = 2/\pi \tan^{-1}(\sigma_t/\sigma_n) \tag{2.14}$$

where σ_t and σ_n are the tangential and normal tractions in the considered cohesive element.

The damage evolution law in ABAQUS is coupled through the damage variable D, and tractions, e.g. in normal direction, depend on displacements in both normal and tangential directions. It is therefore not possible in ABAQUS to formulate an uncoupled damage formulation as used by e.g. Yang and Thouless (2001), since both σ_n and σ_t are exposed to stiffness degradation dictated by the same damage variable $D(\delta_e, \varphi)$. The damage approach in ABAQUS corresponds to the method described in Camanho et al. (2003) and it is possible to formulate various coupled cohesive laws. By setting $(1-D)k_n = \frac{\sigma(\lambda)}{\lambda\delta_n^c}$ and $(1-D)k_t = \frac{\sigma(\lambda)\delta_n^c}{\lambda(\delta_n^c)^2}$ in Eqs. (2.10) and (2.11) the cohesive formulation in ABAQUS equals the Tvergaard and Hutchinson (1993) formulation described by Eq. (2.7). The mixed-mode traction-separation behaviour can be illustrated as in Figure 2.14 (Camanho et al. (2003)).

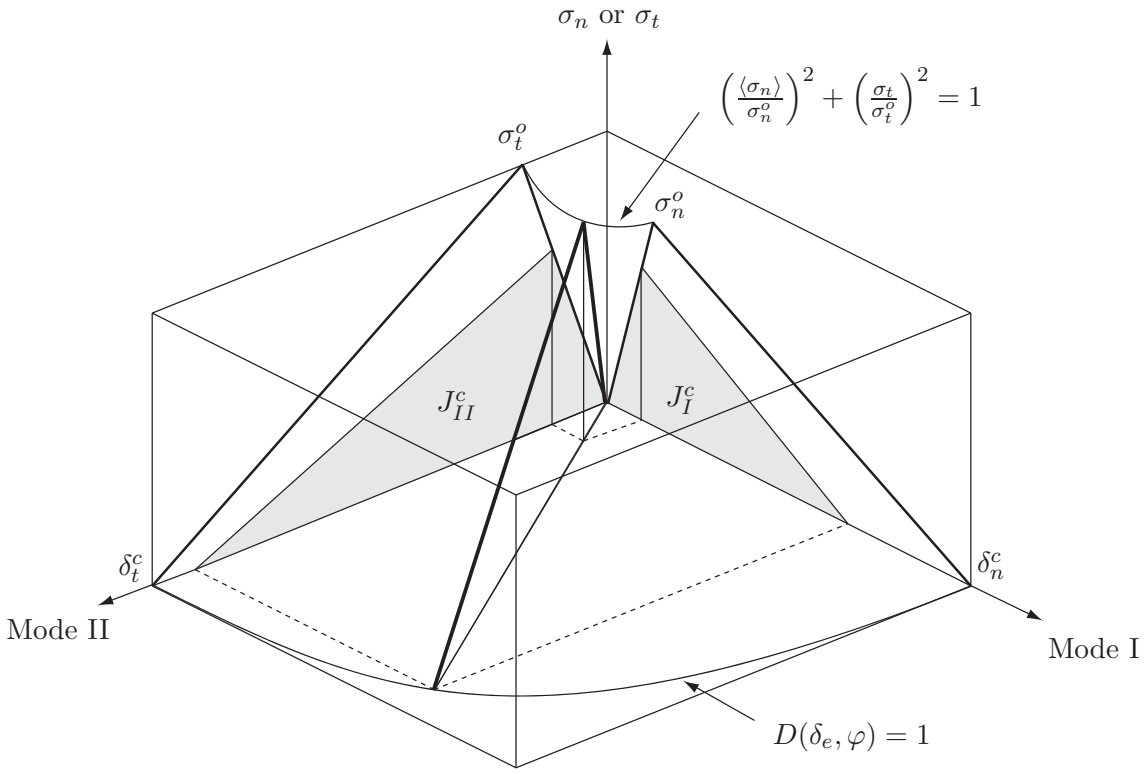

Figure 2.14: Schematic illustration of mixed-mode traction-separation behaviour with linear softening. A mixed-mode opening displacement path is indicated along with corresponding mode I and II fracture energies, J_I and J_{II}, respectively.

The total energy dissipation is given according to (2.5):

$$J_{damage} = J_I + J_{II} \tag{2.15}$$

where the pure mode energies are illustrated as the shaded triangles along the mode I and II axis in Figure 2.14. The figure shows the normal and tangential traction behaviour during loading in a fixed mixed-mode direction: Initially, both the normal and tangential tractions increase linearly according to the cohesive stiffness k until the criterion for damage initiation is met. Then the normal and tangential tractions decrease according to Eqs. (2.10) and (2.11), where the damage variable D is described by a damage evolution law as a function of effective displacement δ_e and φ_J or φ_σ. As $D = 1$ the tractions vanish.

2.2.4 Mode Discrimination

Various energies are available as output parameters from ABAQUS and the most relevant to the analysis conducted in this study are external work, elastic energy, kinetic energy and damage energy. External work is the energy applied to the model from external sources (loads and boundary conditions), elastic energy is the reversible energy stored in elastic deformation, kinetic energy is motion energy and damage energy is the non-reversible energy dissipated in the process zone. To distinguish between mode I and mode II dissipated energy it is desired to extract the damage energy connected with the individual modes. The user is limited to certain ABAQUS output variables and it is not possible to get the energy dissipation for the individual modes directly. Instead this is calculated from other output variables: displacements in n and t directions, damage variable D and initial stiffness k, which are accessible output variables for each cohesive element. The mode I and II dissipated energies are found numerically as described below.

Distinction is made between reversible (elastic) and non-reversible (damage) energies dissipated in the cohesive element. Consider a single cohesive element loaded by the opening displacement δ_A and hence the (by the cohesive law described) closing traction σ_A, see Figure 2.15. In this case the total applied energy is separated in a reversible energy, which is the dark-shaded area below the line going from 0,0 to A, and the light-shaded area is damage energy.

When the opening displacement of a single cohesive element is increased beyond damage initiation, the damage energy increases as well. The damage energy dissipated by going from δ_A to δ_B can be found from geometrical consideration and is illustrated in Figure 2.16.

The increase in damage energy by going from point A to point B is found to be

$$J_{damage,inc} = \frac{1}{2}(\sigma_A\delta_B - \sigma_B\delta_A) \tag{2.16}$$

The increase in damage energy regarding deformation in the normal and tangential directions, respectively, is found from Eq. (2.16), which is the area of the triangle in Figure 2.16.

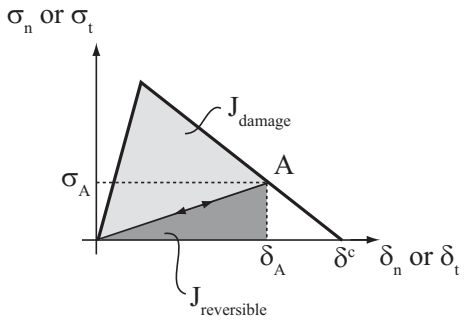

Figure 2.15: Illustration of reversible and non-reversible (damage) energy contributions as the cohesive element is loaded.

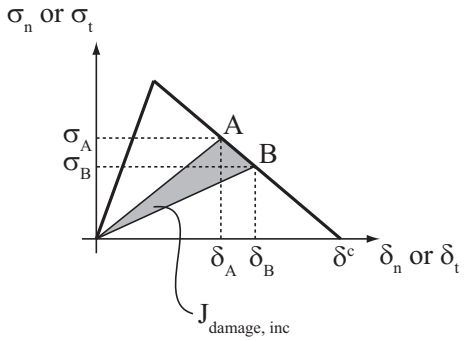

Figure 2.16: Illustration of increase in damage energy as the displacement of the cohesive element is increased from δ_A to δ_B.

This is implemented in an algorithm that extracts the increase in normal and tangential non-reversible energy for each cohesive element for each output time step. The total dissipated damage energy in normal and shear directions J_I and J_{II} at a given time is found as the sum of increase up to this time for all cohesive elements.

2.2.5 Comments on Setting Up the Model

In this section, some of the parameters assigned by the user when performing cohesive zone analysis in ABAQUS/Explicit, are described. The variables are discussed briefly regarding the influence of the variables on the solution and it is the aim that this section should act as a guide for others who intend to build up a similar finite element model in ABAQUS/Explicit. It is outside the scope to describe variables in full detail, and for this the reader is referred to the ABAQUS manual (Abaqus (2006)). The discussed variables are

1. Hourglass control
2. Time step size
3. Density of cohesive material
4. Initial cohesive stiffness k
5. Load ramp time
6. Damping
7. Damage variable D

1. Hourglass control. Four-sided 2-D elements are used in the finite element models presented in this study. In ABAQUS/Explicit only elements with linear shape functions are available and the individual elements will behave poorly in some deformation modes. For a structure exposed to e.g. bending, a finer discretisation is therefore needed to obtain the same accuracy compared to a similar model with higher-order elements. The linear elements used for the present model have spurious singular deformation modes (hourglass) where deformation does not lead to energy dissipation, and therefore no resistance is naturally incorporated. This is solved by resisting these deformation modes artificially by a combined stiffness and viscous approach. The energy dissipated due to this restriction is not physical nor reversible, and care is taken that the artificial energy is always below 1 % of the total elastic energy to confine the error. The problem can be reduced by refining the mesh in regions where stress gradients are high and by distributing concentrated loads and boundary conditions over several nodes instead of just a single node (Abaqus (2006)).

2. Time step size. The time step size can be chosen automatically by ABAQUS or set manually by the user. Usually, the time step in a dynamic analysis is very short compared

to a static one, since it is necessary to capture stress waves moving at high speed in the model. The automatically calculated time step for the dynamic analysis is therefore similar to the crossing time of a stress wave over the smallest element in the model. The wave speed is $\sqrt{\overline{E}/\rho}$, where $\overline{E}$ is the plane stress or strain Young's modulus and ρ is the density of the bulk material. For most simulations conducted in this study the automatically calculated time step was found to be adequate, since a higher value led to problems with convergence whereas a shorter time step increased the calculation time without increasing the accuracy significantly.

3. Cohesive density. Even though the cohesive elements in this study are of zero thickness, they are still associated with a mass per length that is prescribed by the user through the density of the cohesive material multiplied by the nominal thickness. If the density is very small, it will affect the automatically calculated time step and the convergence of the model, whereas if the value is large, it will add significantly extra mass to the system, affecting the results (only for high loading rates). For the present model the density is chosen so that the mass of the cohesive material is approximately 1 % of the total mass, which is found to be a reasonable compromise which will not affect the time step nor the dynamic solution.

4. Initial cohesive stiffness k. Cohesive elements are inserted between continuum elements, which adds extra compliance to the model. Therefore, the slope of the initial linear branch k should be chosen sufficiently high to represent perfect adhesion of the material before damage is initiated. Convergence analyses are conducted in order to ensure that the effect of this extra added compliance is insignificant. A typical value for k in this study is 10 $\overline{E}/h$, where $\overline{E}/h$ describes the stiffness of the specimen in the height direction, $\overline{E}$ is the plane stress or strain Young's modulus of the bulk material and h is half the specimen thickness.

5. Load ramp time. Care should be taken how a load is applied in a dynamic finite element model, since a suddenly applied displacement can result in large reaction forces and substantial stress waves crossing back and forth the specimen. A load should always be associated with a ramp time, and in a quasi-static analysis, care should be taken that the ramp time is sufficiently large to avoid unwanted dynamic effects. The effect of different ramp times will be treated in more detail in Section 6.2.3.

6. Damping. By default damping is added to the explicit dynamic model in the form of bulk viscosity, which can increase the stable time increment and thus decrease the computational time. The viscous damping mostly influences the high-frequency oscillations and is especially useful in a dynamic quasi-static analysis, where stress waves are not appreciated and computational time may thereby be reduced. Care should be taken in a dynamic model with high loading rates since damping might affect the solution significantly. For the dynamic models exposed to high loading rates (described in Chapter 6), damping was not included.

7. Damage variable D. For the present study the damage variable is stated as a tabbing array as a function of effective displacement δ_e and mode-mixity φ. ABAQUS uses linear interpolation between the numbers given in the array, and with a large stiffness k it is necessary to use a very fine discretisation of the monotonically increasing displacement value

δ_e. In the present study the normalised increment of the effective displacement in the array is chosen so that $\delta_e k/\sigma_o \approx 0.05$.

Different variables and methods related to the modelling procedure have been presented, along with a brief discussion of the influence on the solution. In the following, the model is tested by comparing results to an example from the literature. Furthermore, the influence of the shape of the cohesive law for different process zone sizes is demonstrated.

2.2.6 Confirming Model and Relating to LEFM

In this section the previously described finite element model is used to explore the behaviour of a DCB specimen loaded by edge forces. The results obtained are compared with results from an identical loading situation described by Li et al. (2004) to verify the model. Furthermore, the effects of changing the shape of the cohesive law from trapezoidal to triangular, while keeping the maximum stress and area below curve fixed, are explored.

LEFM is based on a mathematical assumption that the process zone is limited to a point at the crack tip, and the fracture process is controlled by the toughness alone. It is given in Li et al. (2004) (and ASTM standard D3433-93 (1993)) that the assumption of LEFM is valid when $\overline{E}J_I^c/\sigma_o^2 h$ is smaller than approx. 0.4.[1] For increasing $\overline{E}J_I^c/\sigma_o^2 h$ values the cohesive strength and the shape of the cohesive law will (increasingly) influence the fracture behaviour.

In the following, two different shapes of cohesive laws are compared regarding the force-displacement relation of a DCB loaded by transverse shear forces F. The peak stress σ_o and the fracture energy J_I^c are identical for the two considered traction-separation laws, but the shape is different, see the illustration in Figure 2.17. The results of a DCB test with the two various cohesive laws implemented are plotted in Figure 2.18 along with results from Li et al. (2004).

In Figure 2.18, the deviations between results from the present model and results presented in Li et al. (2004) are below 2 %. Deviations may be caused by different choice of variables ($\overline{E}$, J_I^c, σ_o and h) in Li et al. (2004) compared to this study, since the used variables are only stated in normalised form.

Besides comparing results to a previous study, the effect of changing the shape of the cohesive law from trapezoidal to triangular may be examined by considering results in Figure 2.18. For values of $\overline{E}J_I^c/\sigma_o^2 h$ below approximately 0.4 the responses of the triangular and trapezoidal traction-separation law are identical, but for increasing $\overline{E}J_I^c/\sigma_o^2 h$ the difference becomes increasingly significant. When the responses of the trapezoidal and the triangle-shaped

[1] In Li et al. (2004) h is chosen as the geometry length scale described in Bao and Suo (1992). According to the ASTM standard LEFM is only valid if the same criterion is fulfilled with h replaced by other relevant geometries such as e.g. the crack length. This is fulfilled in Li et al. (2004) where h is the smallest specimen dimension since the pre-crack length is $a = 2h$.

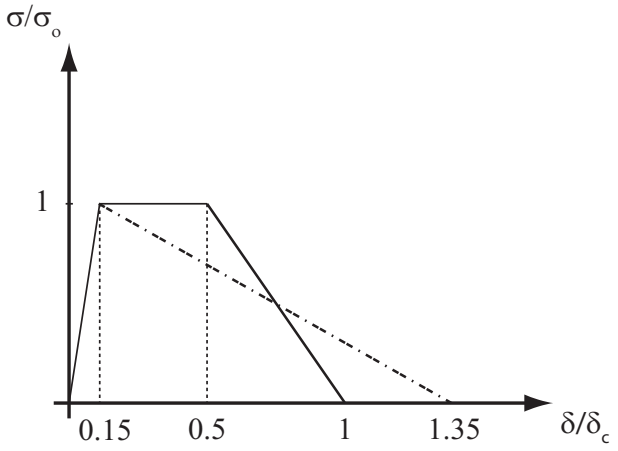

Figure 2.17: Traction-separation laws used for generating results in Figure 2.18.

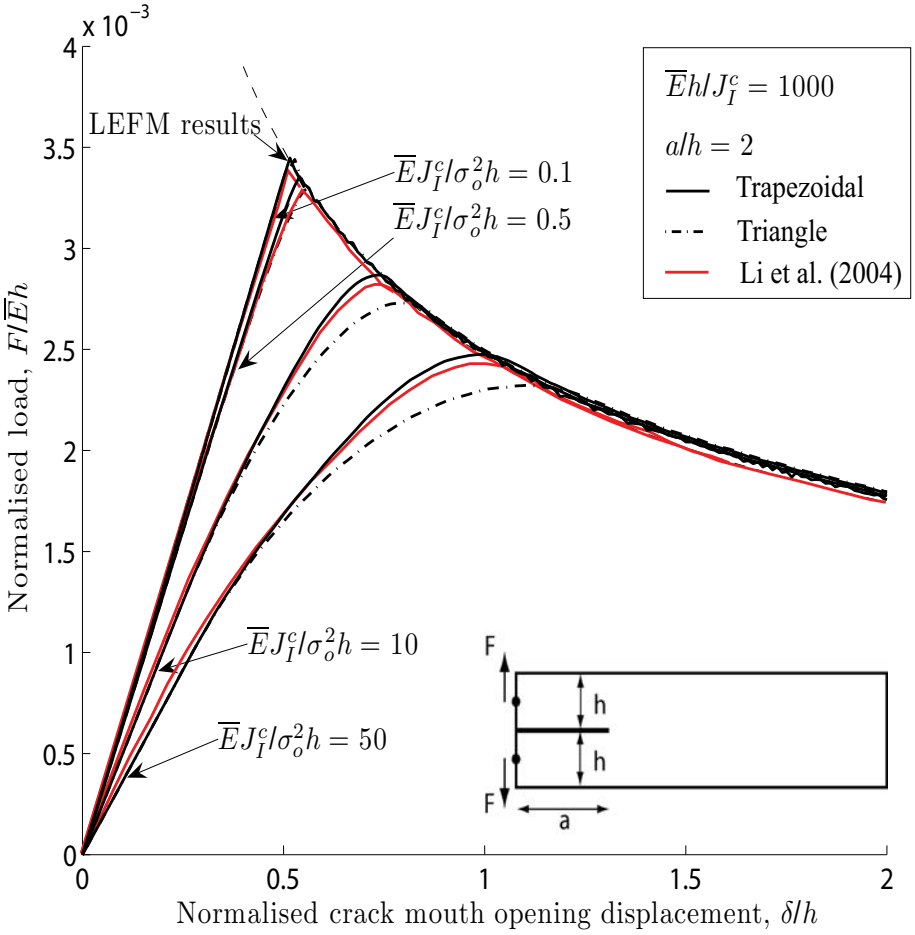

Figure 2.18: Force-displacement diagram for various $\overline{E}J_I^c/\sigma_o^2 h$ values. The cohesive laws used in the model are illustrated in Figure 2.17.

cohesive law are compared with identical $\overline{E}J_I^c/\sigma_o^2 h$ values, it is found that they are coincident for small crack openings, but differ as the process zone evolves to full size. As the crack starts propagating all curves follow the master curve described by LEFM in Li et al. (2004). If the test method considered in this study is to be used for extracting appropriate fracture mechanical data (cohesive laws), it is important that the level of detail extracted from the fracture mechanical test is higher than what is necessary to conduct a subsequent accurate simulation. It is therefore important to choose the geometry of the test specimen, so that the level of detail of the extracted cohesive laws is as high as possible, i.e. $\overline{E}J_I^c/\sigma_o^2 h$ should be well above 0.4.

2.3 Summary

The background and the basic theory for cohesive zone modelling were described. Various test methods for extracting cohesive laws were described and categorised and some advantages and disadvantages mentioned. CZM combines strength- and toughness-based fracture criteria, and the importance of one criterion relative to the other may be found from certain material and geometry dependent length scales. Idealised cohesive laws were described and a comparison study of the influence of shape on fracture behaviour reviewed. One coupled and one uncoupled mixed-mode cohesive law formulation were described and the different kinds of behaviour illustrated with a small example. Issues related to building up a finite element model with a cohesive zone were discussed, e.g. mesh considerations, implementation of cohesive law, discrimination between modes and some user-defined variables important to the finite element model. Finally, the model was tested through a small example and results were compared to the literature.

This page is intentionally left blank.

Chapter 3

Measuring Mixed-mode Cohesive Laws of Sandwich Interfaces

The core idea of this study is to bond stiff layers onto the sandwich faces to increase the bending stiffness, and establish a test procedure that allows direct measurement of mixed-mode cohesive laws for interfaces in sandwich structures. The procedure is a modification of a method described by Østergaard et al. (2007). The advantage of the stiffening includes an increased tolerance of inaccuracies in thickness and elastic properties of the composite faces. Furthermore, the method of determining cohesive laws by the J integral approach, as described in Sørensen and Kirkegaard (2006) for monolithic laminates, is adopted and used to derive cohesive laws for crack propagation in the sandwich interface.

The chapter is organised as follows:

1. Basic mechanics for extracting cohesive laws from experiments using a J integral approach is reviewed. The J integral is employed for a five-layered sandwich specimen by application of laminate beam theory.
2. Effects of adding stiffening layers to the sandwich specimen faces are examined.
3. Specimen dimensions, materials and lay-up are described along with the test procedure.
4. Data analysis and results are presented and discussed for two sandwich types.

3.1 Basic Mechanics and Specimen Analysis

3.1.1 Problem Definition

Crack propagation in sandwich structures might entail Large-Scale Bridging (LSB), in which case the size of the process zone is so large that Linear Elastic Fracture Mechanics (LEFM)

is not applicable. Consider a crack at the interface of a sandwich specimen, see Figure 3.1. The problem is assumed to be two-dimensional and either plane strain or stress conditions prevail.

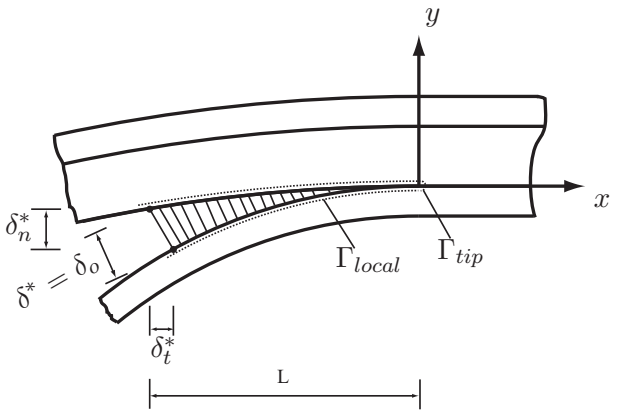

Figure 3.1: Process zone of a crack in a sandwich specimen subjected to mixed-mode loading.

The opening displacement of the pre-crack tip δ^* is projected in a normal and tangential opening displacement component, δ_n^* and δ_t^*. Since the rotation of the specimen can be significant the coordinate system shown in Figure 3.1 rotates with the mean face of the generated crack surfaces, which is later described in detail. The process zone can be considered as a bridged crack either with or without a singular crack tip. In the first case the crack tip is closed for an infinitesimal loading and a singular strain field exists close to the crack tip, whereas behind the crack tip bridging fibres provide closing tractions between the crack faces. Conversely, for a cohesive zone model there is no singularity and the cohesive stresses depend solely on the crack opening displacement, Cox and Marshall (1994). This entails that an infinitesimal loading of the specimen will result in a small opening of the pre-crack tip. In the present study the cohesive zone approach is adopted.

A schematic graph of the fracture resistance, J_R, as a function of pre-crack tip opening is sketched in Figure 3.2 (a). In the presence of LSB it is found to be convenient and physically realistic to separate the process zone mechanisms into (1) cracking of the matrix material and (2) large-scale bridging in the crack wake. The opening of the pre-crack tip is initiated by cracking of the adhesive bond layer at the interface, during which the J integral value increases rapidly. As J reaches a value $J_R = J_o$, the interface begins to separate and the crack propagates more rapidly with fibres bridging in between the separating crack faces. Due to the large-scale bridging in the crack wake the fracture resistance J_R increases further, see Figures 3.1 and 3.2. This can be written as

$$J_R = J_o + J_{bridging} \tag{3.1}$$

where J_o and $J_{bridging}$ are the contribution to the fracture toughness of the resin and the fibre bridging, respectively. As the opening of the initial crack tip reaches δ_c, the fracture resistance reaches a steady state plateau and the process zone simply translates along the

interface as the crack propagates. The crack opening δ_c where the fibres break is considered a material property for a fixed crack opening ratio δ_t^*/δ^*. Conversely, the length of the process zone at steady state L is not a material parameter, since it depends on the specimen geometry and loading, Suo et al. (1992).

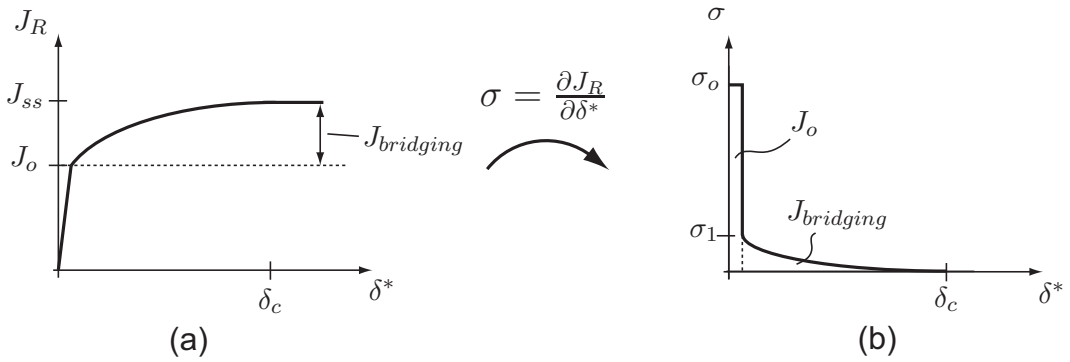

Figure 3.2: Schematic graph of J_R as a function of pre-crack tip opening (a) and derived cohesive law (b).

The normal and shear stresses acting on the crack surfaces due to fibre bridging can be related to the fracture energy dissipated in the process zone by applying the J integral locally around the crack faces and tip, see Figure 3.1. The following expression is taken directly from Sørensen and Kirkegaard (2006) and Suo et al. (1992).

$$J_R = \int_0^{\delta_n^*} \sigma_n(\delta_n, \delta_t) d\delta_n + \int_0^{\delta_t^*} \sigma_t(\delta_n, \delta_t) d\delta_t \tag{3.2}$$

where σ_n and σ_t denote the tractions in the normal and tangential directions, respectively, in the cohesive zone. As indicated by (3.2) the cohesive stresses are assumed to depend only on the local opening displacements, δ_n and δ_t, and not on the opening path.

By differentiating (3.2) with respect to δ_n^* and δ_t^* (Sørensen and Kirkegaard (2006))

$$\frac{\partial J_R(\delta_n^*, \delta_t^*)}{\partial \delta_n^*} = \sigma_n(\delta_n^*, \delta_t^*) \quad \wedge \quad \frac{\partial J_R(\delta_n^*, \delta_t^*)}{\partial \delta_t^*} = \sigma_t(\delta_n^*, \delta_t^*) \tag{3.3}$$

where $\sigma_n(\delta_n^*, \delta_t^*)$ and $\sigma_t(\delta_n^*, \delta_t^*)$ are stresses between the crack faces as a function of normal and tangential opening of the pre-crack tip. From (3.3) the cohesive law can be obtained directly from J_R and measured values of δ_n^* and δ_t^*.

The phase angle $\varphi_\delta = \tan^{-1}(\delta_t^*/\delta_n^*)$ may be used to describe the mode ratio, see Figure 3.3, since conventional LEFM mode-mixity measures are invalid for CZM because of the lack of singularity. By conducting tests for several φ_δ (see Figure 3.3) a surface is generated by interpolating the J_R values between the measured curves. For any given point on the surface the slope of the surface tangent in the δ_n^* and δ_t^* directions, respectively, is the stress in the normal and tangential direction, as described by Eq. (3.3).

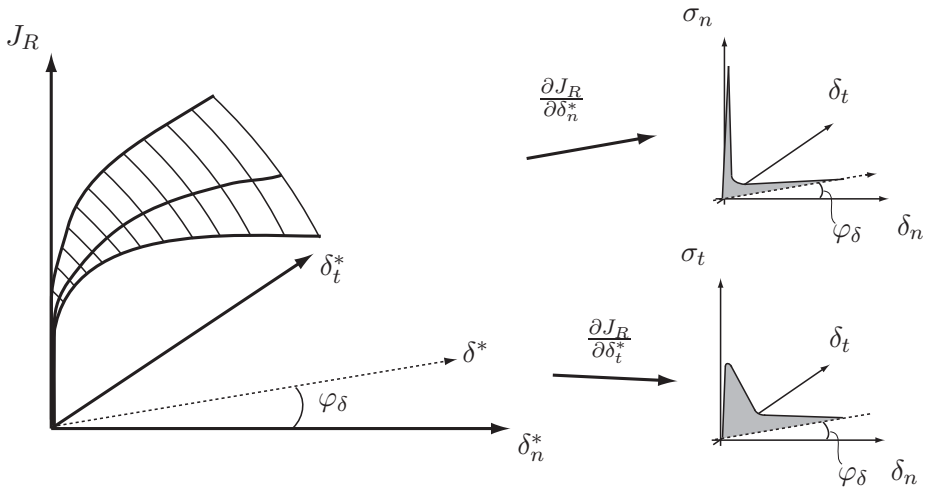

Figure 3.3: Process of extracting cohesive laws from measured J_R, δ_n^* and δ_t^*.

3.1.2 Specimen analysis

In general, under LSB it is not possible to determine the J integral (evaluated around the external boundaries) analytically, since J depends on details of the cohesive laws. For instance, for the standard DCB loaded by transverse (shear) forces, J depends on the beam rotation, which again depends on details of the cohesive law, Högberg and Stigh (2006). However, J can be found analytically for some type of test specimens, e.g. DCB specimens loaded by axial forces and bending moments, Suo et al. (1992). The present study uses a DCB specimen loaded by Uneven Bending Moments (DCB-UBM), see Sørensen et al. (2006). For this specimen J_R can be determined analytically from specimen geometry, elastic properties and applied moments by considering a contour along the outer boundaries of the specimen. In the following, a J integral analysis is conducted for a multilayered specimen using laminate beam theory.

The J integral in general form is given by Rice (1968):

$$J = \int_\Gamma W dy - \sigma_{ij} n_j \frac{\partial v_i}{\partial x} dS \tag{3.4}$$

where Γ is a path going from the lower crack surface to the upper in a counterclockwise direction, $W = \int \sigma_{ij} d\epsilon_{ij}$ is the strain energy density ($= \frac{1}{2}\sigma_{ij}\epsilon_{ij}$ for linear elastic materials), σ_{ij} is the stress tensor, n_j is the outward normal to the considered contour, and v_i are components of the displacement vector. When body forces are neglected, the J integral is path independent Rice (1968), so evaluation along an inner path surrounding the process zone gives the same result as evaluating J along the outer edges of the specimen. The former gives (3.2) and the latter can be evaluated analytically for a DCB-UBM specimen, since the specimen is loaded by pure moments and either plane strain or stress conditions prevail. As mentioned previously, a new specimen design is proposed: Steel bars are adhered to the faces

of the sandwich to reduce deformations and multiple effects of this are described later. The path surrounding the crack is divided into pieces, one for each layer, and the numbering is illustrated in Figure 3.4.

For specimen sides parallel to the x-direction, see Figure 3.4, $dy = 0$ and $\sigma_{xx} n_x = 0$, thus the only non-zero contributions to the J integral originate from the paths near the specimen ends where the moments are applied. Note that for beam 1 and 2, $dS = -dy$ and the outward normal $n_j = (-1, 0)$, whereas for beam 3, $dS = dy$ and $n_j = (1, 0)$, thus for all the sketched paths ($p = 1..10$), $n_j dS = dy$.

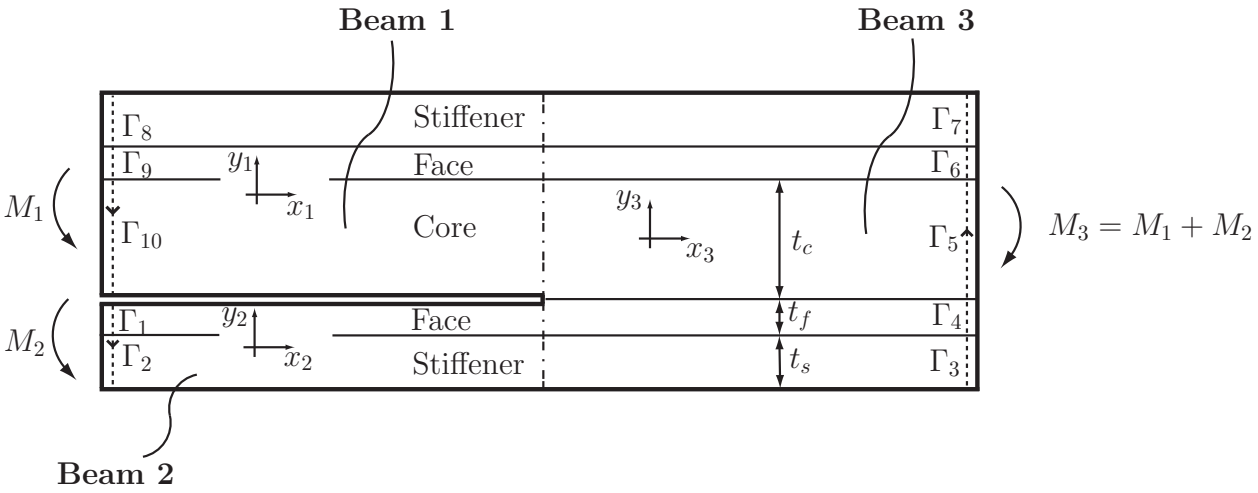

Figure 3.4: Non-zero J integral path pieces for multilayered DCB specimen.

Each layer is considered individually, since the stresses vary discontinuously between layers. The strain energy density given by $W = \frac{1}{2}\sigma_{ij}\epsilon_{ij}$ along with $\partial v_1/\partial x = \epsilon_{xx}$ and $n_j dS = dy$ is inserted in (3.4):

$$J = \sum_{p=1}^{10} \int_{\Gamma_p} -\frac{1}{2}(\sigma_{xx})_p(\epsilon_{xx})_p dy \tag{3.5}$$

where p is the path number indicated in Figure 3.4 and $(\sigma_{xx})_p$ and $(\epsilon_{xx})_p$ are stresses and strains in the x-direction in the layer where path p is located. By assuming isotropic linear elastic material behaviour far from the crack tip

$$(\sigma_{xx})_p = \overline{E}_p(\epsilon_{xx})_p \tag{3.6}$$

where $\overline{E}_p = E_p/(1 - \nu_p^2)$ for plane strain and $\overline{E_p} = E_p$ for plane stress. By inserting into (3.5)

$$J = \sum_{p=1}^{10} \int_{\Gamma_p} -\frac{1}{2}\overline{E}_p(\epsilon_{xx})_p^2 dy \tag{3.7}$$

Note regarding (3.7) that the contribution to J is positive, for beam 1 and 2 since dy is negative (see Figure 3.4), while the opposite is the case for beam 3.

The specimen is analysed by laminate theory. The DCB-UBM specimen is considered as three multilayered individual beams, see Figure 3.4. The strain distribution in each beam is found from laminate beam theory as given in Carlsson et al. (2005). The constitutive properties are given by extension, coupling and bending terms A_b, B_b and D_b where b indicates separate terms for each of the three beams sketched in Figure 3.4. The applied laminate theory assumes zero shear deformation and perfect bonding between layers. The former assumption is reasonable since the specimen is loaded by pure moments and shear deformation is practically negligible. The latter is also reasonable from the perspective that the foam and the composite faces are relatively compliant compared to the thin adhesive connection between layers.

The force N_x and bending moment M_x are given by

$$N_x = A\epsilon_x^0 + B\kappa_x \tag{3.8}$$

$$M_x = B\epsilon_x^0 + D\kappa_x \tag{3.9}$$

where ϵ_x^0 and κ_x is the midplane strain and curvature of the considered beam in the x-direction, see Figure 3.4. The extension, coupling and bending terms are defined for each of the three beams as

$$\begin{aligned} A_b &= \sum_{k=1}^{n} \overline{E}_k (y_k - y_{k-1}) \\ B_b &= \frac{1}{2} \sum_{k=1}^{n} \overline{E}_k (y_k^2 - y_{k-1}^2) \\ D_b &= \frac{1}{3} \sum_{k=1}^{n} \overline{E}_k (y_k^3 - y_{k-1}^3) \end{aligned} \tag{3.10}$$

where k is the ply index, n is the number of layers in the current beam ($n = 3$ for $b = 1$, $n = 2$ for $b = 2$ and $n = 5$ for $b = 3$), $\overline{E}_k$ is the previously defined elastic modulus in the x-direction for ply k, and y_k is the y-coordinate for the interface between ply $k-1$ and k relative to the midplane of the beam. Since the specimen is loaded by pure moments, $N_x = 0$ and (3.8) and (3.9) are written as

$$\epsilon_x^0 = -B\kappa_x / A \tag{3.11}$$

$$\kappa_x = \frac{M_x}{D - B^2/A} \tag{3.12}$$

The strain distribution through the beam thickness is given by

$$\epsilon_x = \epsilon_x^0 + \kappa_x y \tag{3.13}$$

By inserting (3.13) into (3.7), J is formulated as a function of beam extension, bending and coupling terms A_b, B_b and D_b.

$$J = \sum_{p=1}^{10} \frac{\overline{E}_p M_b^2}{6(A_b D_b - B_b^2)^2} [A_b^2(y_{p-1}^3 - y_p^3) - 3A_b B_b(y_{p-1}^2 - y_p^2) + 3B_b^2(y_{p-1} - y_p)] \qquad (3.14)$$

where p is the path number and b = (1,2,3) indicates which beam p is located in, see Figure 3.4, so $b = 2$ for $p = 1$ to 2, $b = 3$ for $p = 3$ to 7 and $b = 1$ for $p = 8$ to 10. Note that J depends on the moments, geometry and elastic properties of the materials, not the crack length. This is different from the conventional DCB test, where the specimen is loaded by forces, ASTM (1996).

It is found that, while (3.14) is derived for a five-layer DCB-UBM specimen, which is used in this study, the expression can be used for a specimen with any number of layers by changing the numbering and the summation boundaries.

3.1.3 Model Verification

The J integral values obtained from (3.14) are compared with known solutions for a bi-material specimen, Suo and Hutchinson (1990), and for a three-layered sandwich specimen, Sørensen et al. (2006), see Figure 3.5. Both of these models assume perfect bonding between layers and zero transverse shear deformation which in the case of pure bending moment (without loading by a transverse force) is accurate. By assuming that two or more layers of the five-layered specimen (illustrated in Figure 3.4) have identical material properties, the model can be reduced to a bimaterial or a three-layered sandwich specimen. Plane strain and the following idealised material properties, thicknesses and loads are assumed for the comparison (subscript 1 refers to material #1 etc.): $E_1 = 10^{10}$ Pa, $E_2 = 10^8$ Pa, $\nu_1 = 0.3$, $\nu_2 = 0.2$, $H = 10$ mm, $h = 30$ mm, and $M = 100$ Nm, see Figure 3.5. The J integral values obtained from (3.14) and solutions from Suo and Hutchinson (1990) and Sørensen et al. (2006) agree within 0.001 %, which is attributed to round-off errors in the calculations.

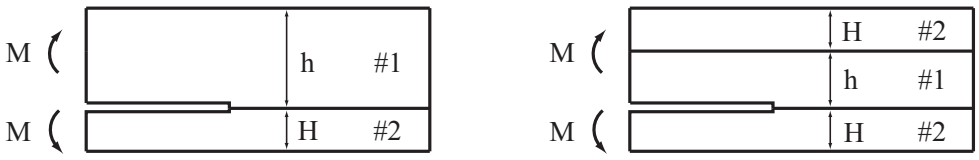

Figure 3.5: Illustration of bimaterial and three-layered sandwich specimen used for checking the model.

3.1.4 Thickness and Strength of Stiffening Material

The purpose of this section is to illustrate the design procedure for finding the optimal steel thickness and required yield stress to avoid plasticity in the steel during loading of the

specimen.

The sandwich specimen with dimensions and elastic properties as described in Lundsgaard-Larsen et al. (2008) is used, however, the same analysis applies to other materials and geometries as well. Plane stress is assumed, thus $\sigma_x = \epsilon_x E_s$, where the strain distribution is assumed to be linear and described by (3.13) and the J value is found from (3.14). For a fixed moment ratio of $M_2/M_1 = 1$, J is plotted as a function of the maximum stress in the steel, σ_{max}, see Figure 3.6.

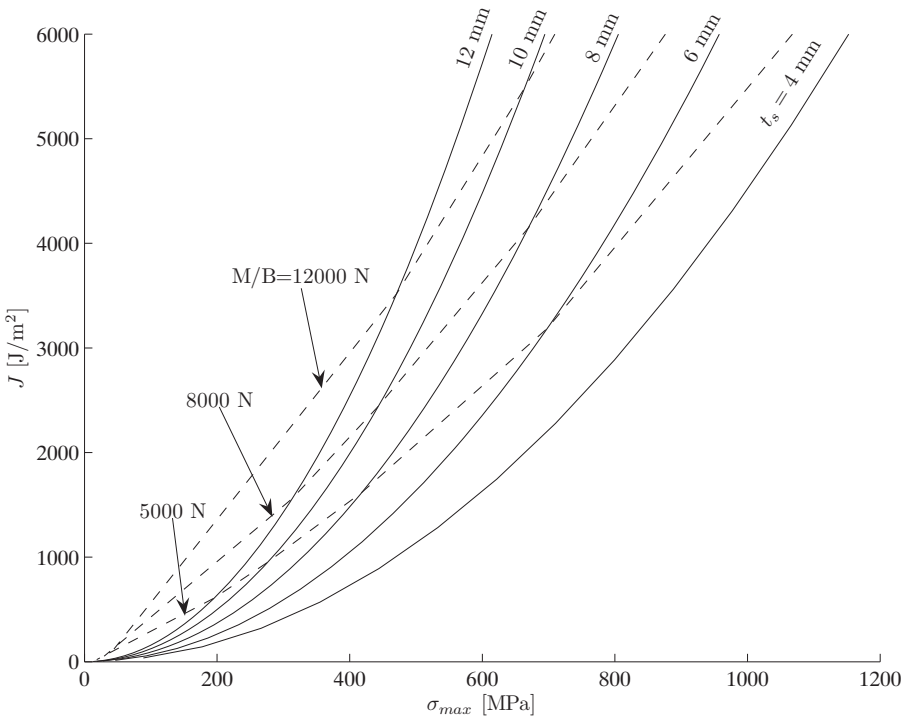

Figure 3.6: Design diagram illustrating J as a function of maximum stress in the reinforced material (for $M_1/M_2 = 1$). Solid lines represent fixed thickness of the reinforcement material, and dashed lines represent fixed moment divided by specimen width. The material properties and thicknesses used are $E_f = 14.1$ GPa, $\nu_f = 0.32$, $t_f = 2.9$ mm, $E_c = 240$ MPa, $\nu_c = 0.3$, and $t_c = 57.$ mm.

The plot in Figure 3.6 is utilised to find the desired level of J that may be reached without risking plastic deformation in the steel bar or moment loadings above the design purpose of the test-rig. Four variables enter into the plot in Figure 3.6, namely J value, maximum stress in the steel, steel bar thickness, and applied moment. The J value is plotted along the y-axis, the maximum stress along the x-axis, the solid lines represent constant steel thicknesses with varying moments and dashed lines vice versa. The dashed lines indicate the limit of a zone (below the line) where the moment is within the capacity of the test rig. (The test rig is presented in Section 3.2.2).

For example, if the desired level of J is 3000 J/m^2 (imagine a horizontal line for $J = 3000$ J/m^2 in Figure 3.6) the steel thickness, applied moment and maximum stress can be found. It is found that with decreasing steel thickness, a higher yield stress is required. The test rig used is designed for specimens of $B = 0.03$ m wide and with a maximum moment of 150 Nm, thus the maximum allowed M/B ratio is 5000 N. To obtain a J value of 3000 J/m^2 within this limit (below the dashed line of M/B=5000N) the yield stress should be approx. 700 MPa for a 6 mm thick bar and 800 MPa for a 4 mm thick reinforcement. The desired level of J cannot be reached by use of any other of the proposed steel thicknesses, while maintaining the maximum design load of the test rig.

The opening displacement of the pre-crack tip in the normal and tangential direction is analyzed for various moment ratios using beam theory in Appendix A. This is included to describe the expected coupling between moment ratio M_1/M_2 and opening displacements δ_n^* and δ_t^*.

3.1.5 Effects of Face Stiffening on the Accuracy of J and Process Zone Length

Applying stiffening material to the thin sandwich faces is important to the described test method. In this section the effects of the stiffening are analysed. Sandwich faces are often heterogeneous and anisotropic and exact stiffness properties can be difficult and test costly to obtain. It will be shown below that for a stiffened DCB specimen where the laminates are compliant in comparison with the stiffening material, the properties of the faces have only minor influence on the J integral value (this was also pointed out in Li et al. (2006b)). It is hence expected that more accurate interface toughness measurements can be obtained, since the exact stiffness parameters of the sandwich faces are no longer of great importance to the results. This is investigated in the following. A plot of normalised J vs. t_f/t_s is shown in Figure 3.7. The analysis is conducted for the geometry and materials used in this study, see Section 3.2.1, but results would be similar for other stiffened specimens.

For the test specimen considered in this study, $t_f/t_s = 0.483$ and $E_f/E_s = 0.067$. The influence of varying the stiffness and thickness of the faces on the J value for constant moments is investigated. If say the maximum allowed deviation on J is chosen to be 5 %, E_f can vary 25 % and t_f 17 %, which is found by considering Figure 3.7. The measured J is therefore quite insensitive to variations of face stiffness and thickness.

Another effect of stiffening the faces is the elongation of the process zone, see Figure 3.8. The effect of the spatial material variation on the derived cohesive laws is expected to be smaller since the fracture process takes place over a larger area and local material variations are evened out.

The influence of the stiffening thickness on the process zone length is investigated by using the Kirchhoff beam model described in Appendix A. The process zone length as a function of

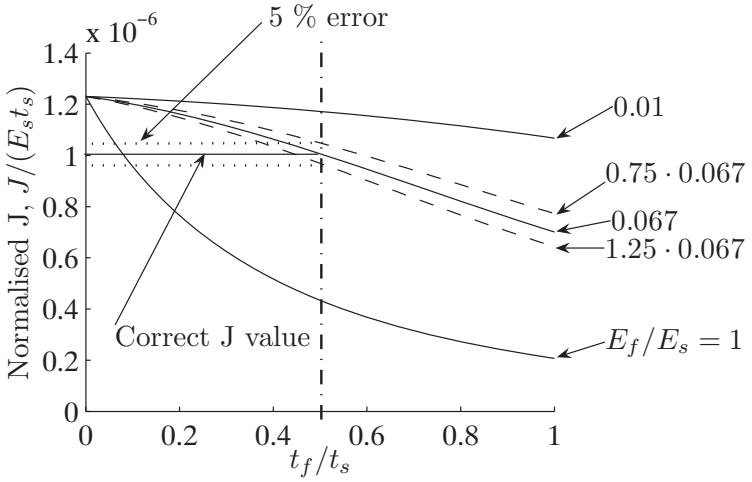

Figure 3.7: Normalised J as a function of t_f/t_s for various E_f/E_s. t_s=6 mm, $E_s = 2.1 \cdot 10^{11}$ Pa, $M_1/B = M_2/B = 3333$ N. Dashed lines represent values obtained using E_f/E_s values that are ±25% off the correct one.

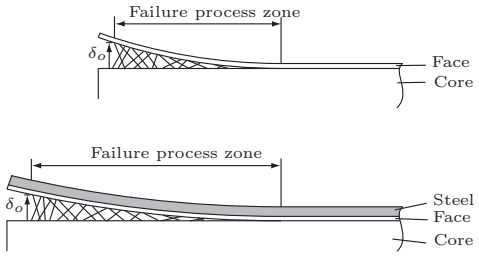

Figure 3.8: By stiffening the face by a metal bar the length of the process zone is increased.

steel thickness is calculated by assuming that steady state is reached when the crack opening is, say $\delta^*/t_f = 3/8$. For the generated plot $J/(E_s t_s) = 8 \cdot 10^{-7}$ and $M_1/M_2 = 1$.

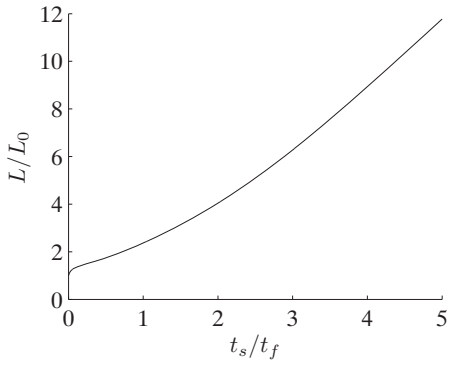

Figure 3.9: Normalised crack length L/L_0 as a function of normalised steel thickness t_s/t_f, where L_0 is the crack length for $t_s = 0$ (no stiffening). Elastic properties and thicknesses are the same as in Figure A.1.

The plot shown in Figure 3.9 is generated in the following way. For any given steel thickness t_s the moment $M_1 (= M_2)$ to obtain, $J/(E_s t_s) = 8 \cdot 10^{-7}$, is found from (3.14). Then the process zone length L to obtain the given crack opening, $\delta^*/t_f = 3/8$, is calculated from (A.1) and (A.2), see Appendix A, where δ^* is related to δ_x^* and δ_y^* by $\delta^* = \sqrt{(\delta_x^*)^2 + (\delta_y^*)^2}$.

By consulting Figure 3.9 it is found that for the specimens used in this study (t_s/t_f=2.07), the fracture process zone is increased by a factor of approx. 4 due to the face stiffening. The elongated process zone due to stiffening is consistent with the R-curve behaviour described e.g. in Suo et al. (1992). Here the damage zone length to reach steady state increases with beam stiffness (thickness).

3.2 Experiments

This section describes details regarding material properties and geometries used for the DCB-UBM experiments.

3.2.1 Specimen Geometry and Materials

Sandwich panels were manufactured using vacuum injection moulding with the glass fibre faces being approximately 3.5 mm thick with two different lay-ups. All specimens have four mats of quadraxial Devold Amt DBLT 850-E10-I and an additional mat with fibres oriented randomly, either Chopped Strand Mat (CSM) and Continues Filament Mat (CFM), both

with a dry area weight of 450 g/m^2. The CSM consists of short fibre bundles of 4-5 cm, whereas the CFM consists of very long fibre bundles. It is the intention that the intermediate CSM or CFM layer should generate fibre bridging as the crack propagates, since fibres are easily being pulled out of this layer. A thorough description of the idea behind using this additional laminate is provided in Chapter 4. All faces are assumed to be in-plane isotropic and the elastic properties of the individual layers are found from additional tests described in Jenstrup and Karlsen (2007) with an effective E-modulus of 14.5 GPa and a Poisson ratio of 0.33.

The polyester resin is Polylite® 413-575, which is specially suited for vacuum injection due to low viscosity. The 20 mm thick Divinycell H200 PVC foam core has a density of 200 kg/m^3 and is manufactured by DIAB AB. The core material is assumed to be linear elastic and isotropic and elastic properties are found in a manufacturer data sheet with an E-modulus and a Poisson ratio of 240 MPa and 0.32, respectively. As discussed previously, large deflections are prevented by adhering 6 mm thick steel bars to each face. To avoid plastic (non-linear) deformation of the stiffening material, steel with a high yield strength of 800 MPa is chosen (the steel type is IMPAX, manufactured by Uddeholm in Sweden). A 12.5 μm thick slip film is placed in the sandwich interface during production to archive a well defined start crack. The geometry of the specimen is shown in Figure 3.10.

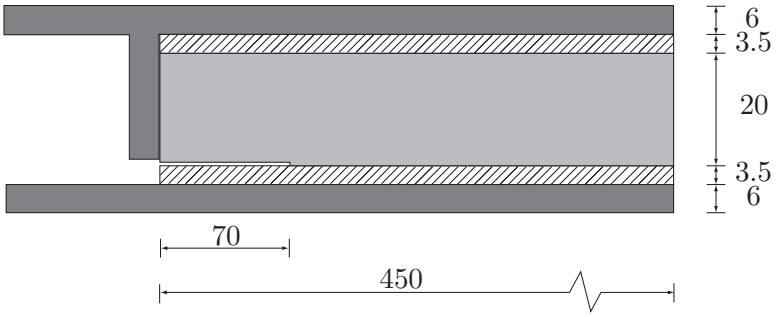

Figure 3.10: Sandwich specimen with pre-crack (dimensions in mm). The specimen is stiffened by 6 mm steel bars adhered to the faces.

The purpose of the vertical steel bar in Figure 3.10 is to transfer deformation to the edge and thus reduce the influence of the otherwise free edge on the stress state in the specimen.

3.2.2 Test Procedure

A unique test rig that allows loading of the DCB sandwich specimen by pure uneven bending moments (DCB-UBM) is used for conducting the experiments. A schematic illustration of the test rig and the loaded specimen is shown in Figure 3.11, and a more detailed description is found in Sørensen et al. (2006). The test is conducted under displacement control in a tensile test machine, and the moment ratio is kept constant throughout the test.

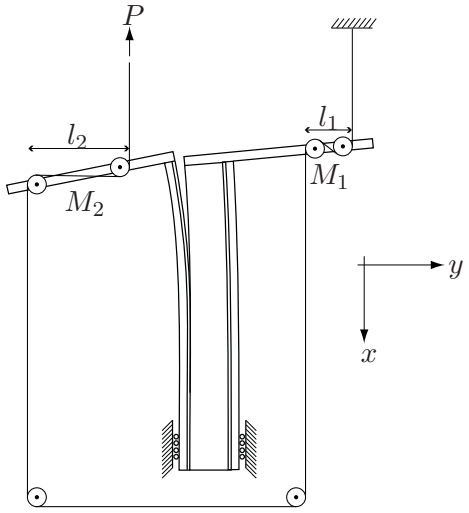

Figure 3.11: Schematic of the loading principle of a DCB-UBM sandwich specimen.

The moments are obtained from a roller-wire system mounted to the top of the specimen, and the force in the wire is measured by a 5 kN load cell. The load is applied by a single wire, thus ensuring that the forces acting on the rollers in the y-direction are equal in size. The moments acting on the left and the right beam are determined from the wire force, P, and the distance between the rollers, thus

$$\begin{aligned} M_1 &= Pl_1 \\ M_2 &= Pl_2 \end{aligned} \tag{3.15}$$

where M_1 and M_2 are moments acting on the left and the right beam defined positive counterclockwise.

The ratio between M_1 and M_2 is adjusted by changing the distance between the rollers. Furthermore, the direction of the moments can be reversed by changing the mounting direction of the wire. If moments with opposite signs are applied, e.g. $M_1/M_2 = -1$, crack opening in the normal direction is dominating (mode I). If moments with the same sign are applied, the crack opening in the tangential direction is more dominating (mode II). It is possible to vary the loading and thus the tangential/normal crack opening ratio δ_t^*/δ_n^* to almost any desired value.

The opening of the initial crack tip position in the normal and tangential directions is measured throughout the test. In earlier experiments with crack propagation in monolithic laminates, this was successfully conducted by inserting pins into the material and measuring displacements with extensometers and LVDTs, see Sørensen et al. (2006). For sandwich specimens, the core is soft and it is tedious to fasten pins close to the crack tip. Instead, in the present study, displacements are measured with a commercial Digital Image Correlation

(DIC) system, ARAMIS. A speckled pattern is applied to the surface of the specimen by spray paint, which allows the system software to track full field 3-D displacements of the specimen surface. The setup including specimen and two 2.0 Mpixel cameras mounted on a tripod is seen in Figure 3.12.

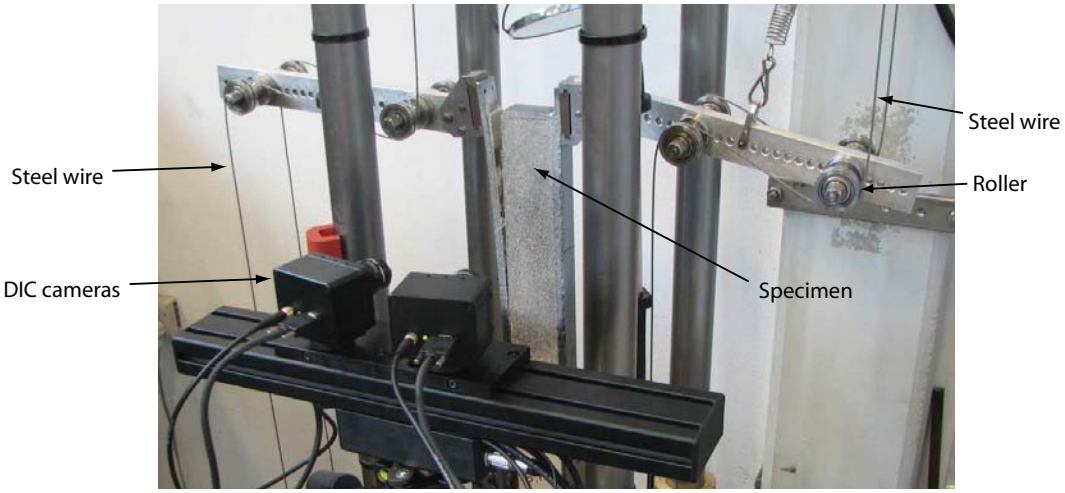

Figure 3.12: The deformation of the sandwich specimen is tracked by two 2.0 Mpixel digital cameras at a frequency of 1 frame per second.

For the DIC measurements the sandwich specimen is spray painted with first white and then black paint to generate a random speckled pattern, which is traceable by the DIC system. The measurement area is approximately 100 by 100 mm and the facet size used for tracing the speckled pattern is 15 by 15 pixels with an overlap of 2 pixels. The accuracy of the DIC system is tested before conducting the experiment. Five pictures are taken of the undeformed specimen while moving the tripod with the two cameras approximately 10 mm for each new picture. Two points are selected on the specimen, and the system identifies these points in each picture. The distance between the two identified points is compared for each picture and the deviation is below 2 μm. This accuracy is, however, dependent on the speckled pattern and the size of the measurement area.

If the two moments M_1 and M_2 are acting in the same direction the resultant moment $(M_1 + M_2)$ can cause the specimen to rotate significantly. This global rotation is taken into consideration in measurements of the normal and tangential crack openings (δ_n^* and δ_t^*). Thus, the opening of the pre-crack tip δ^* is projected to a coordinate system rotated with the deformed sandwich specimen, see Figure 3.13. The rotations θ_1 and θ_2 of beam 1 and 2 are measured from displacements of four points (q_1, q_2, q_3 and q_4). Before the specimen is loaded, the four points are located on a straight line perpendicular to the specimen sides and points q_2 and q_3 are coincident with the tip of the pre-crack. A local (n, t) coordinate system is rotated $\theta_3 = (\theta_1 + \theta_2)/2$ relative to the global (x, y) coordinate system so that the t-axis constitutes the rotated x-axis. The displacements projected to the n and t-axes govern the normal and tangential crack opening (δ_n^* and δ_t^*), respectively.

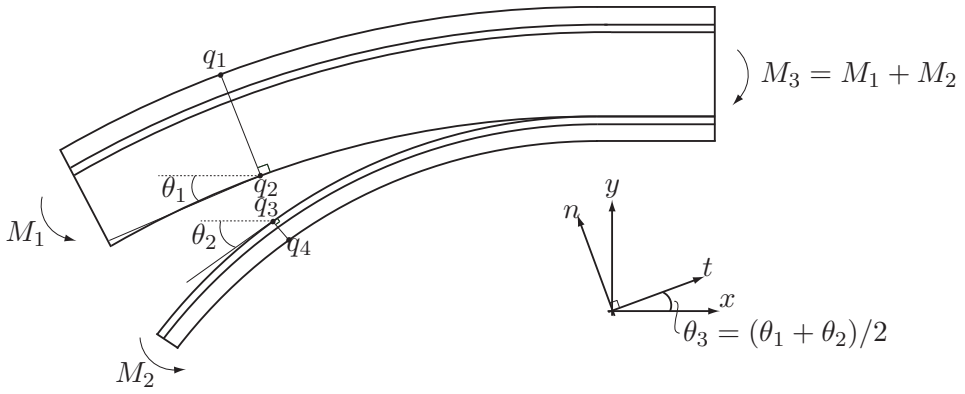

Figure 3.13: Crack opening displacements in the normal and tangential directions δ_n^* and δ_t^* are found by projecting the openings to a rotated coordinate system.

3.3 Results

In this section the processing of data is described and results in the form of a fracture resistance surface plot and derived cohesive laws are presented. M.Sc. students Claus Jenstrup and Kasper Karlsen, who conducted their Master's thesis project with the author as co-supervisor, see Jenstrup and Karlsen (2007), contributed to developing the methods described in this section. First, results for the specimens with a CSM inserted in the interface are presented, and subsequently results for the CFM are shown.

The purpose of the DCB-UBM test is to determine the traction-separation behaviour of sandwich interfaces for various combinations of crack openings δ_n^* and δ_t^*. As described in Appendix A any mode ratio from pure normal to pure shear opening can be obtained by loading the specimen by an appropriate moment ratio. However, the crack will only for a limited mode ratio propagate in the interface without kinking into the adjacent face or core. The J integral as described by (3.14) is based on the assumption that the crack propagates in the interface, and that crack kinking will lead to inaccuracies in the measured fracture resistance. Furthermore, it is difficult to interpret a cohesive law for a crack that gradually kinks, e.g. through layers of the laminate, since the measured fracture resistance history then consists of data from different intermediate layers. For these reasons only the moment ratio interval where the crack stays in the interface during propagation is considered in the following. The issue of crack kinking will be dealt with in Chapter 4.

3.3.1 Surface Representation of Fracture Resistance

The specimens are loaded by four moment ratios $M_1/M_2 = \{-0.5, -0.4, -0.2, 0.0\}$, see Figure 3.4 for the moment numbering and sign convention. The J integral is calculated from the experimental results using Eq. (3.14), and Figure 3.14 shows the results in the form

of fracture resistance J_R vs. pre-crack tip opening δ^* for one specimen. The curve can be separated into two branches, where the first consists of a steep increase in J_R with only a small crack tip opening δ^*, which corresponds to local deformation and/or microcracks developing near the crack tip. As the J_R value reaches a material specific value $J_o \approx 470$ J/m^2 the crack propagates and the pre-crack tip opens significantly more than in the first branch. Steady state is obtained at $J_{ss} \approx 870$ J/m^2, where the curve reaches a plateau. During the tests it was observed that the crack did not propagate at a constant speed, but in jumps of 2-5 cm observed on the fracture resistance curve as sudden drops in J_R. It is desired to extract the points from the curves which give information about the fracture resistance of the material, i.e. only results where the crack propagates. These points are extracted for each of the two branches, so that for the first branch with the steep increase, points are selected according to sufficiently small increments regarding δ^*, and for the second branch only peak points are selected, see Figure 3.14. The fracture resistance during unstable crack growth is not measurable by this test, since the specimen is not in static equilibrium with the applied moments during unstable crack growth. Further, it is believed that inertia effects might play an important role in the unstable fracture behaviour, which is not accounted for in the J integral calculations. A numerical algorithm is used to extract and save the relevant points for further analysis, see example in Figure 3.14.

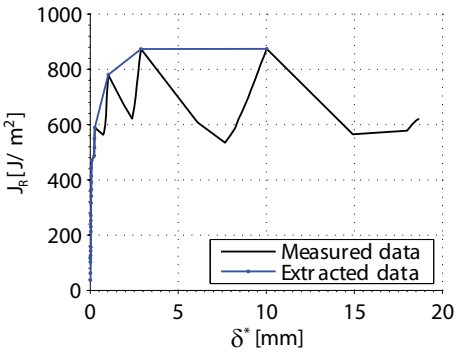

Figure 3.14: Measured and extracted data from a single DCB-UBM test with $M_1/M_2 = 0$.

The results shown in Figure 3.14 are obtained for a moment ratio of $M_1/M_2 = 0$, which are compared to results for other moment ratios in Figure 3.15. Three specimens were tested for each moment ratio. In Figure 3.15 the original specimen numbering is sustained, and may be compared to the physical cracked specimens.

For the selected moment ratios $M_1/M_2 = \{-0.5, -0.4, -0.2, 0.0\}$ the crack propagates within the CSM layer and does not kink into the adjacent face or core. It is, however, observed in some cases that the crack kinks into the core or face for a short while during growth, which is governed by random imperfections in the specimen and might explain the observed scatter. Generally, the fracture resistance decreases as the moment ratio moves from -0.5 toward 0.0, i.e. the opening of the pre-crack tip becomes more shear dominated. It is desired to plot the fracture resistance J_R versus the normal and tangential openings of the pre-crack tip δ_n^* and δ_t^* and in this way generate a fracture surface plot. In order to have a

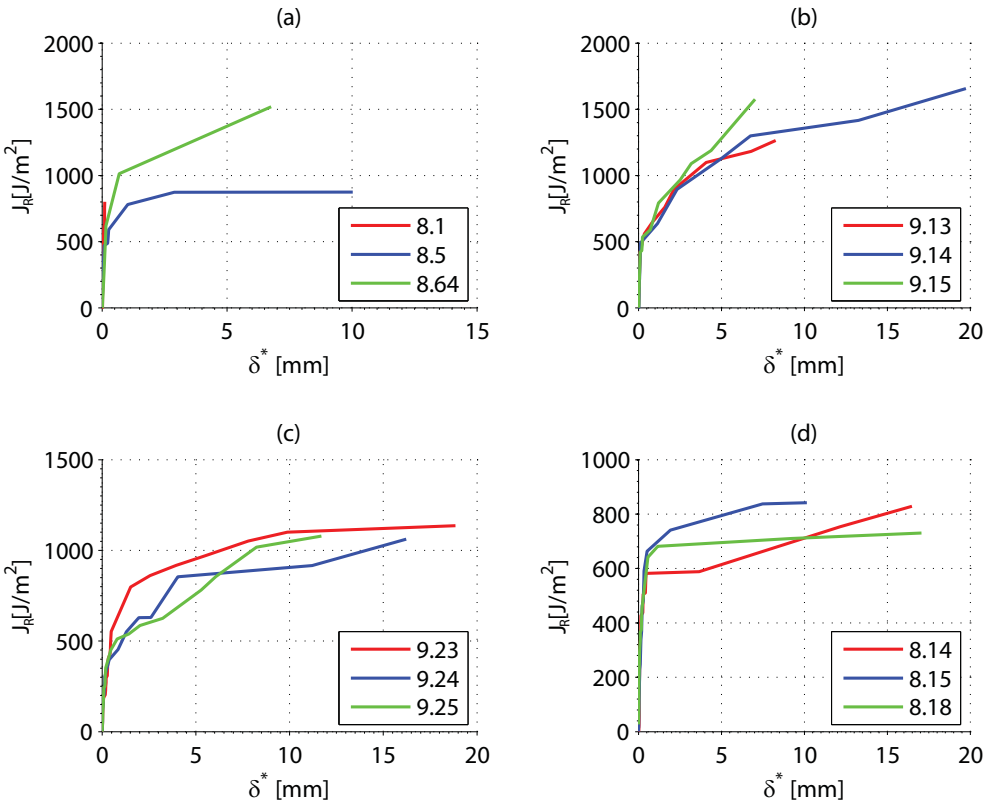

Figure 3.15: Fracture resistance plotted as a function of initial pre-crack tip opening for $M_1/M_2 = \{-0.5, -0.4, -0.2, 0.0\}$ corresponding to subplot (a), (b), (c) and (d), respectively.

consistent data representation of the measured fracture resistance curves, the δ_n^* and δ_t^* data are extrapolated linearly from the point where the data ends until a δ_n^* value of 10 mm, see Figure 3.16. The inter-/extrapolated data are modified slightly to prevent overlap of the four different displacement curves for small δ^* values i.e. actual and interpolated data are not completely coinciding. Overlapping data would complicate subsequent analysis described in the following.

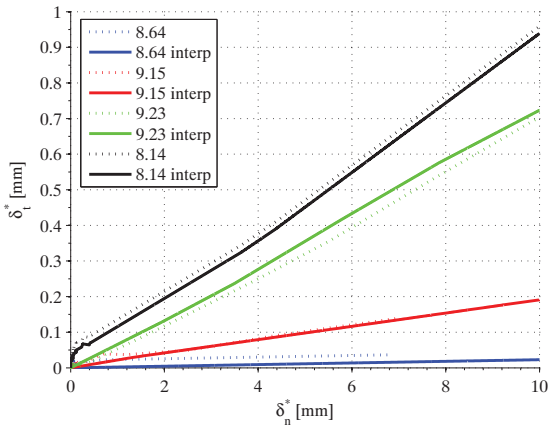

Figure 3.16: Measured and inter/extrapolated pre-crack tip opening δ_t^* vs. δ_n^* for $M_1/M_2 = \{-0.5, -0.4, -0.2, 0.0\}$ corresponding to specimen 8.64, 9.15, 9.23 and 8.14, respectively.

Four specimens (one representing each load case of the moment ratios described above) are chosen to generate the fracture resistance surface, and Figure 3.16 illustrates the opening history of specimens chosen for further analysis. The four J_R vs. δ_n^* and δ_t^* data curves are used to generate the fracture resistance surface by interpolating linearly between them, see Figure 3.17. It is seen that the fracture resistance decreases as the opening becomes more shear dominated (δ_t^*/δ_n^* increases). This behaviour is discussed in Section 3.3.5.

As mentioned previously, the fracture resistance curves generally consist of two branches, where the first is the steep increase in J_R before the pre-crack tip opens, and the second is the gradually increasing J_R toward a steady state plateau after the pre-crack tip has opened. The surface interpolation is conducted for the two different branches independently, so a relatively fine grid regarding δ_n^* and δ_t^* values is used for the surface interpolation of the first branch and a relatively coarse grid is used for the second. The refined grid gives a higher resolution regarding the cohesive laws in the area with steep increase, whereas the coarser grid for the second branch ensures moderate computational time. The illustration in Figure 3.17 shows only the surface in the second branch.

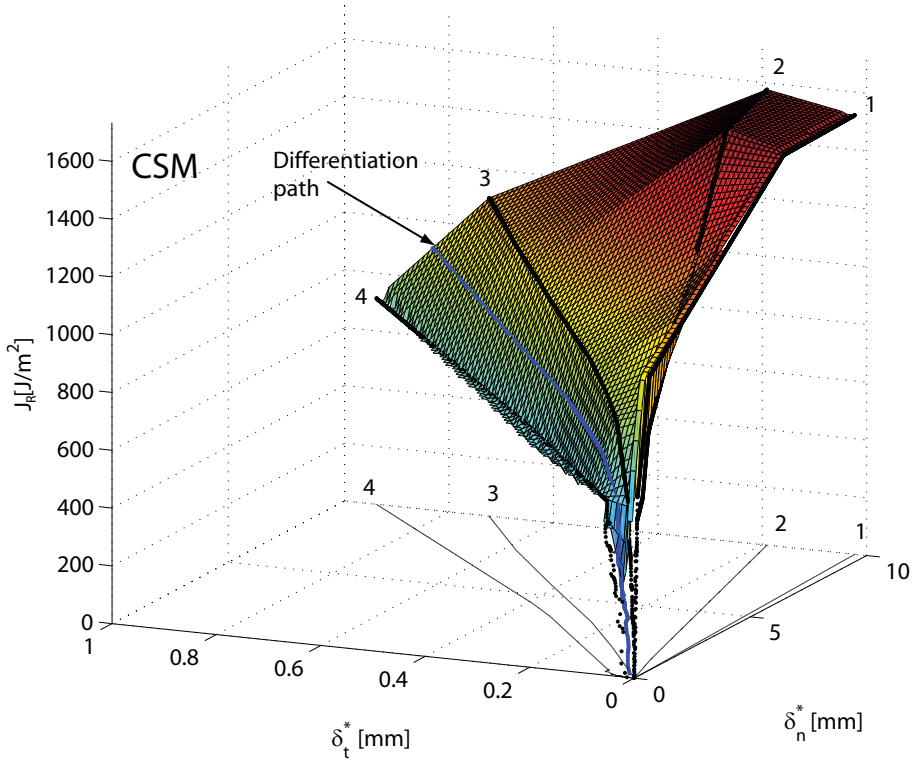

Figure 3.17: Fracture resistance surface J vs. δ_n^* and δ_t^* generated by linear interpolation between measured fracture resistance curves 1 to 4. The phase angle is approximately constant for each experiment and estimated at $\varphi_\delta = \{0.13°, 1.1°, 4.0°, 5.1°\}$ for path 1 to 4, respectively. Three intermediate differentiation paths are found as the average displacements δ_n^* and δ_t^* between the fracture resistance curves. An example of the differentiation path between fracture resistance curves 3 and 4 is indicated by the blue line.

3.3.2 Extracting Mixed-mode Cohesive Laws

In this section mixed-mode cohesive laws are extracted from the fracture resistance surface. As shown schematically in Figure 3.3, cohesive laws regarding normal and shear stresses can be obtained from the fracture resistance surface (J_R vs. δ_n^* and δ_t^*) as the slope of the fracture resistance surface in the normal and tangential directions, respectively. In general, the cohesive law should be found as two complete surface plots, i.e. σ_n vs. δ_n and δ_t, and σ_t vs. δ_n and δ_t. However, the fracture resistance surface is generated from linear interpolation between the four representative experiments i.e. the four black lines in Figure 3.17, and it is found sufficient to only differentiate the fracture resistance surface along three intermediate paths between the four conducted tests. This simplifies the analysis and the visualisation of the results. An example of the path in the middle of two fracture resistance curves is shown as the blue line in Figure 3.17, which is defined by the average opening data values δ_n^* and δ_t^* of specimens 9.23 and 8.14, see Figure 3.16. The surface slopes in the δ_n^* and δ_t^* directions are found numerically by comparing the J_R value of the considered point with J_R of the four surrounding points, as shown schematically in Figure 3.18.

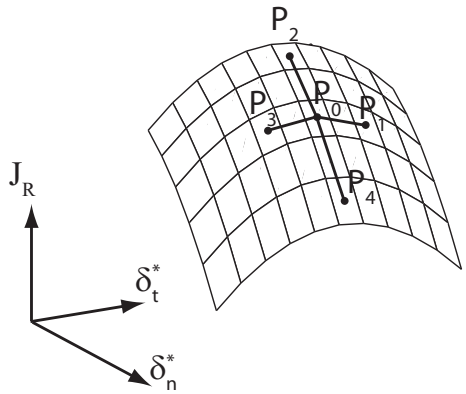

Figure 3.18: Illustration of points used for numerical differentiation of the surface in point P_0 in the normal and tangential directions.

For illustration purposes the surface in Figure 3.18 is generated from a parabolic function whereas the fracture resistance surface is created using linear interpolation. The slope of the surface is found numerically by considering the J_R, δ_n^* and δ_t^* coordinates for the points $P_0, P_1, ..., P_4$ in Figure 3.18, where P_1 and P_3 have the same δ_n^* coordinate as P_0, and P_2 and P_4 have the same δ_t^* coordinate as P_0. The normal and shear stresses are found numerically from Eqs. (3.16) and (3.17).

$$\sigma_t(P_0) = \frac{\alpha_1 + \alpha_3}{2} \ , \quad \alpha_1 = \frac{J_R(P_0) - J_R(P_1)}{\delta_t^*(P_0) - \delta_t^*(P_1)} \ \wedge \ \alpha_3 = \frac{J_R(P_0) - J_R(P_3)}{\delta_t^*(P_0) - \delta_t^*(P_3)} \tag{3.16}$$

$$\sigma_n(P_0) = \frac{\alpha_2 + \alpha_4}{2} \ , \quad \alpha_2 = \frac{J_R(P_0) - J_R(P_2)}{\delta_n^*(P_0) - \delta_n^*(P_2)} \ \wedge \ \alpha_4 = \frac{J_R(P_0) - J_R(P_4)}{\delta_n^*(P_0) - \delta_n^*(P_4)} \tag{3.17}$$

By repeating this approach cohesive laws are extracted for three intermediate paths placed between the curves from the four chosen specimens. The path numbering is chosen so that path 1 is placed between specimens 8.64 and 9.15, where the opening is mostly dominated by normal opening, i.e. the smallest δ_t^*/δ_n^* ratio, path 2 is placed between specimens 9.15 and 9.23 and path 3 between specimens 9.23 and 8.14 (illustrated by the blue line in Figure 3.17). The cohesive laws regarding the normal and tangential directions are shown in Figures 3.19, 3.20 and 3.21.

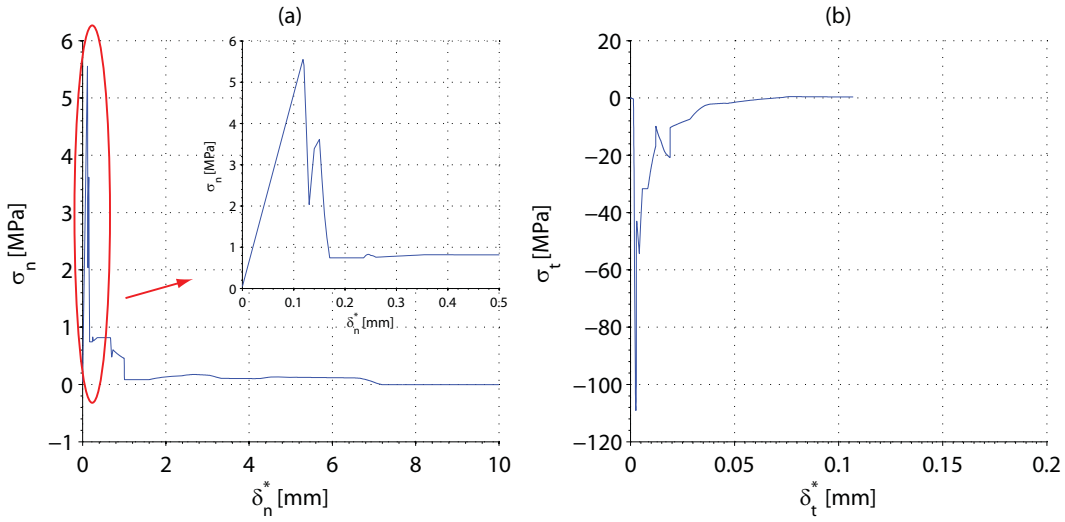

Figure 3.19: Extracted cohesive laws for path 1: (a) normal stress vs. normal opening displacement and (b) shear stress vs. tangential displacement. The steady state fracture resistance for the considered test is $J_{ss} = 1548$ J/m^2.

Like the fracture resistance curves, the derived cohesive laws consist of two branches, the first representing the high stresses before the crack-tip opens, and the second being the stresses transferred through fibre bridging in the process zone after opening of the pre-crack tip.

First, consider the normal stress vs. the normal opening, given in subplot (a) in Figures 3.19-3.21. In the first branch within a normal opening δ_n^* range of 0-0.5 mm, the normal stress σ_n reaches peak stresses of 5.6 MPa, 5.1 MPa and 5.7 MPa for path numbers 1, 2 and 3, respectively. For the second branch within a δ_n^* range of 0.5-10 mm, σ_n initially reduces to a relatively small stress value in the range of 0.1 to 0.3 MPa and from here gradually decreases to zero. The tractions in the tangential direction are shown in subplot (b) of the figures and, generally, they are about an order of magnitude larger than the normal stresses. It should, however, be noted that all stress values in the tangential direction above 5 MPa are reached at displacements of less than 0.05 mm. The validity of the stresses in the tangential direction is discussed in Section 3.3.5.

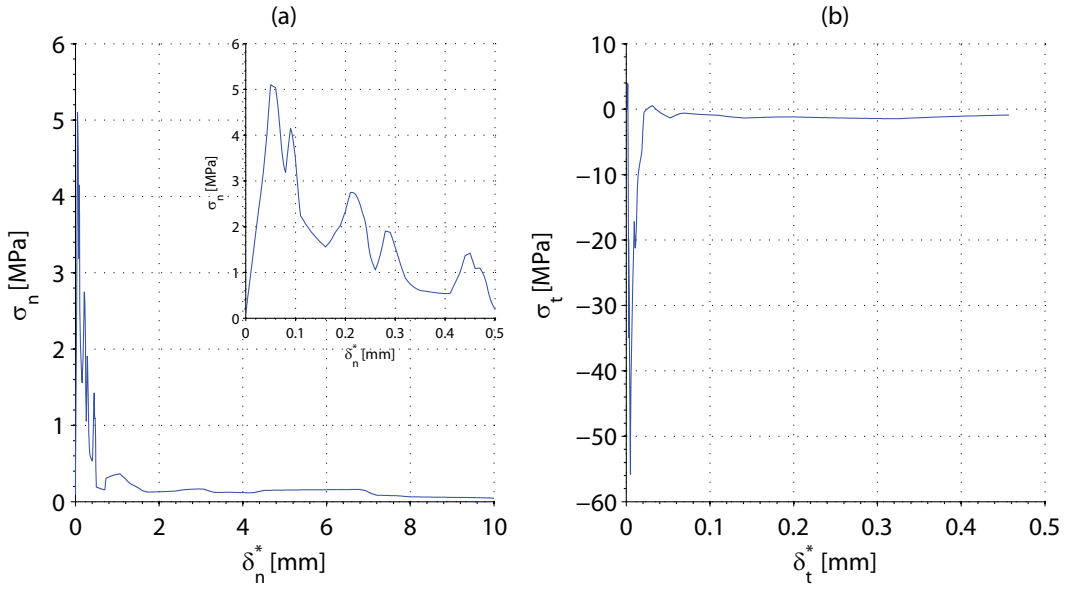

Figure 3.20: Path 2: (a) normal stress vs. normal opening displacement and (b) shear stress vs. tangential displacement. The steady state fracture resistance is $J_{ss} = 1339$ J/m^2.

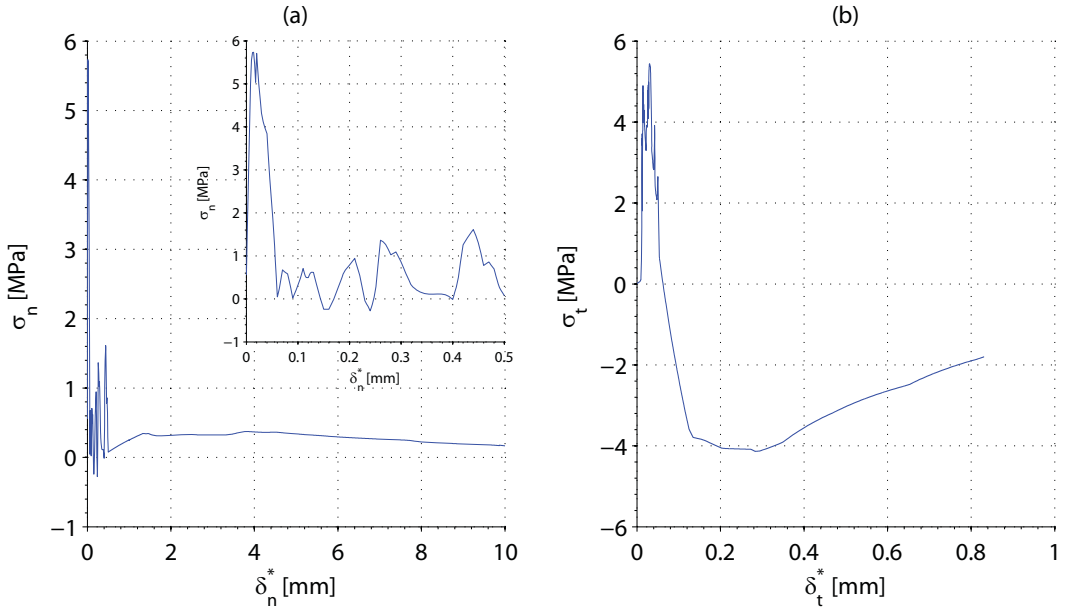

Figure 3.21: Path 3: (a) normal stress vs. normal opening displacement and (b) shear stress vs. tangential displacement. The steady state fracture resistance is $J_{ss} = 906$ J/m^2.

3.3.3 Results for the CFM Layer Configuration

The following describes results in the form of fracture resistant surface and cohesive laws for sandwich interfaces with a Continuous Filament Mat (CFM) between face and core, and the purpose of using a CFM mat in the interface is dealt with in Chapter 4. Since the procedure for generating the results is the same as for the specimens with a CSM described previously, the results are described briefly whereas a more elaborate discussion of the behaviour is found in Section 3.3.5. The fracture toughness surface plot is generated from four representative DCB-UBM experiments with moment ratios $M_1/M_2 = \{-0.4, -0.2, -0.12, 0.0\}$ shown in Figure 3.22. The blue line indicates an example of one out of three intermediate paths along which cohesive laws are obtained from partial differentiation in the normal and tangential directions.

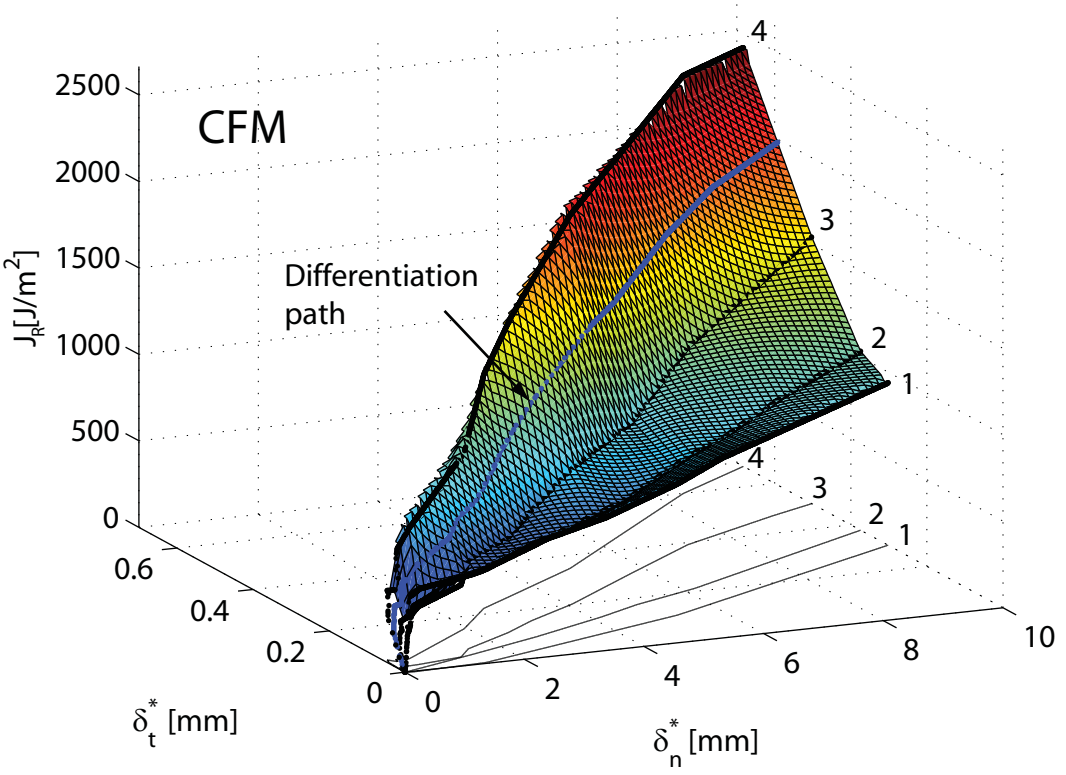

Figure 3.22: Fracture resistance as a function of opening in normal and shear directions. The surface is generated from four tested specimens represented by black lines and an example of the differentiation path is indicated by a blue line. The phase angle is estimated at $\varphi_\delta = \{1.4°, 2.0°, 3.1°, 4.0°\}$ for path 1 to 4, respectively.

The cohesive law is obtained by numerical differentiation along the three intermediate paths and plotted in Figure 3.23. As discussed in Section 3.3.5 the validity of the stresses in the tangential direction is doubtful, thus only stresses in the normal direction as a function of normal displacement are considered in Figure 3.23.

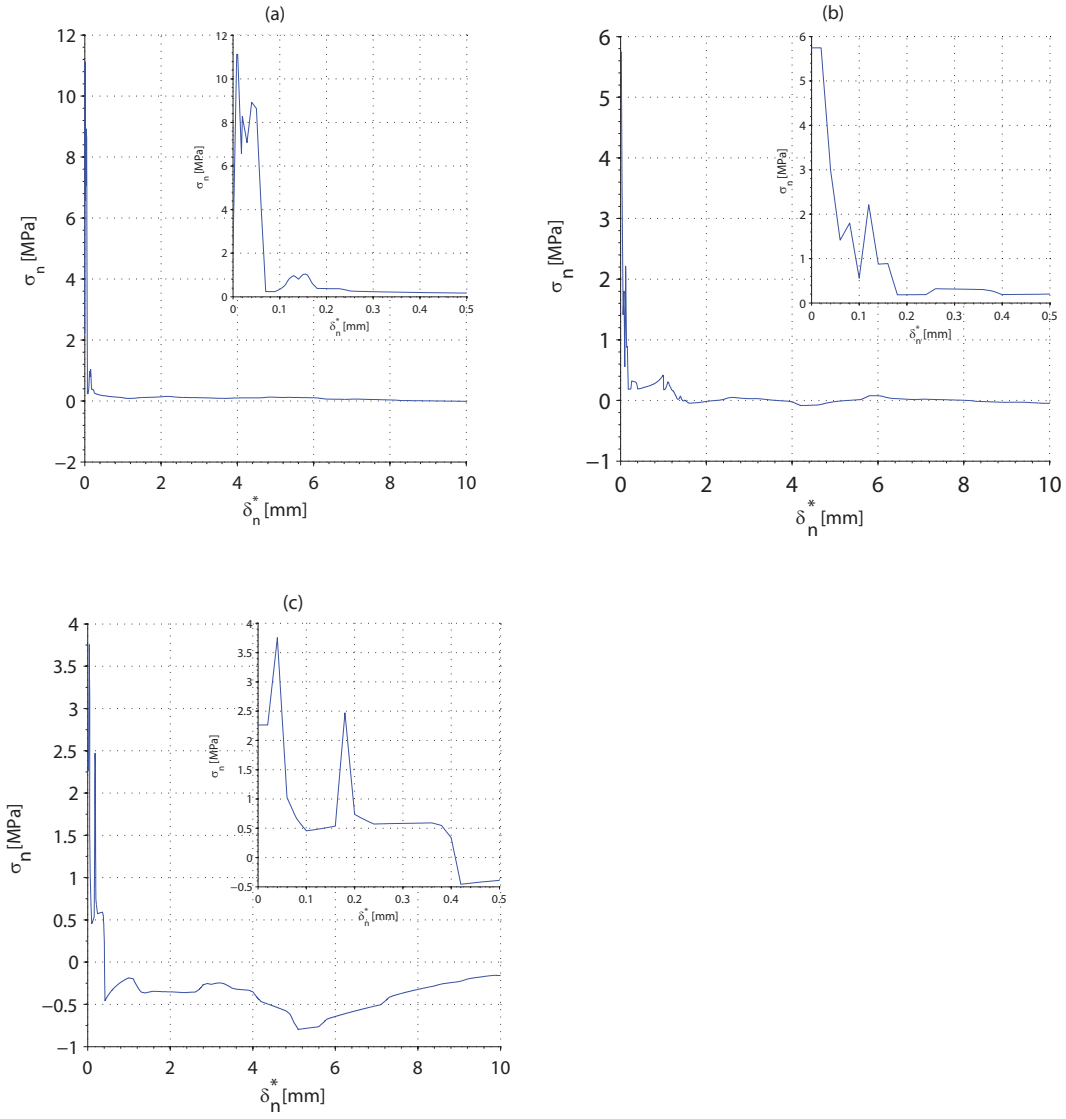

Figure 3.23: Cohesive laws derived along three intermediate paths in subplot (a), (b) and (c) with increasing mode II dominated loading when going from (a) to (c). The maximum stresses in subplot (a), (b) and (c) are 11.1, 5.7 and 3.8 MPa, respectively, and steady state fracture resistances are 986, 1290 and 1980 J/m^2.

As was the case for the specimens with CSM, the shape of the cohesive laws from the CFM configuration consist of two branches indicating a distinction between the crack tip processes and fibre bridging in the crack wake. Results are discussed in Section 3.3.5.

3.3.4 Effect of Specimen Width

The effects of specimen width (z-direction in e.g. Figure 3.1) are investigated. Fibres may bridge across the crack in different angles including across the width direction, which suggests that this dimension might have an influence on the fracture toughness. The general specimen width is 30 mm, and results for these specimens are compared to those for 20 and 40 mm specimens, see Figure 3.24, in the form of J_R vs. δ^*. It is found that the fracture resistance clearly increases with increasing width. The consequence of this is discussed in Section 3.3.5

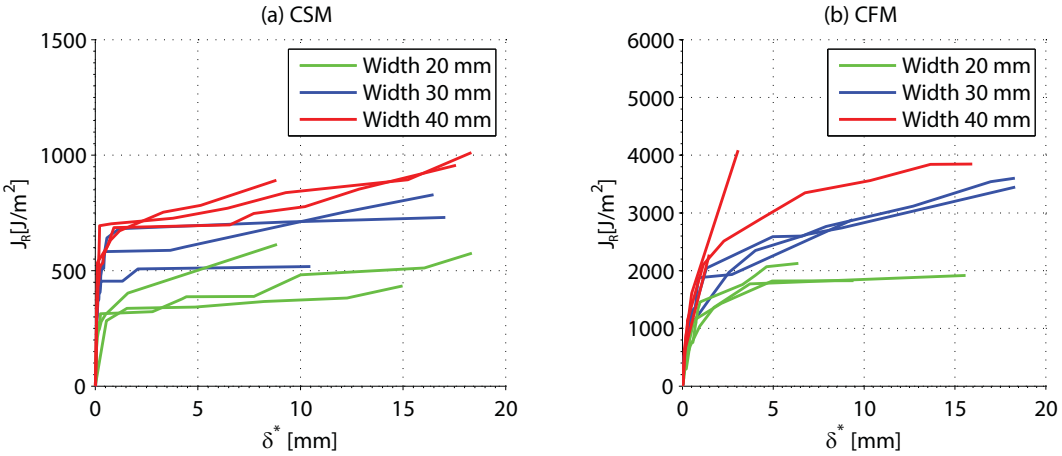

Figure 3.24: Fracture resistance J_R as function of opening displacement δ^* for specimens 20, 30 or 40 mm in the width direction. Subplot (a) shows results for specimens with a CSM layer in the interface, and (b) results for a CFM in the interface. Both are loaded with the moment ratio $M_1/M_2 = 0$.

3.3.5 Discussion and Perspectives

Results for sandwich specimens with a layer of either CSM or CFM between face and core were presented in the previous sections. For all results described the crack propagated in the intermediate CSM or CFM layer and did not kink into the adjacent face or core. This behaviour is a result of two interrelated conditions: (1) The CSM or CFM layer in the interface constitutes a weak layer compared to the face laminate and core, and (2) the loading ratio is sufficiently mode I dominating to avoid crack kinking into the adjacent layers. Subsequent results revealed that as the loading became mode II dominated the crack kinked into the face or core, and this scenario will be covered in Chapter 4.

Regarding the cohesive laws obtained for specimens with a CSM layer, see Figure 3.19 (a), the maximum normal stress of 5.6 MPa is considered to be the strength of the material at which the material will start separating. For comparison the strength of the H200 foam material is 7.1 MPa (DIAB (2008)). The measured peak stress is dependent on the measured displacements within the first branch of the J_R vs. δ^* curve where J_R increases rapidly, and the crack opening is found by tracking displacements of points initially located near the tip of the pre-crack. In practice, these points (p_2 and p_3 found in Appendix A Figure 3.13) are not coincident, but separated approx. 2 mm on the unloaded specimen. This is necessary to avoid following points very close to the opened crack faces, which cannot be traced by the photogrammetry system. Thus the deformation of the material between the points (p_2 and p_3) will create an error dependent on the deformation level between them. This was investigated by selecting points (p_2 and p_3) with different initial distances and interpolating relative displacements to points with zero initial distance. Results show that the maximum stress in the measured cohesive law can vary in the magnitude of 30 % for the specimens considered. However, the general shape of the cohesive law is not significantly influenced by the deformation between measure points, and neither is the energy. A better estimate of the peak stress could be obtained by reducing the measurement area of the DIC system, thus increasing the amount of pixels per unit area. Then it would be possible to obtain measurements closer to the specimen edges and in this way reduce the elastic deformation between the points p_2 and p_3.

For comparison results are found qualitatively similar to mode I fracture of polymer composites in Li et al. (2005b), where the cohesive law is obtained by matching numerical results to experimental observations. Here the cohesive law is described by three parameters; the cohesive strength, the characteristic strength and the fracture toughness. The cohesive strength is the load an intact interface can support whereas the characteristic strength is a parameter that in the presence of a notch controls crack growth together with the fracture toughness value. The need to take these two different strength values into account (or in general take the detailed shape of the cohesive law into account) depends on the circumstances, since there are cases where a high level of detail is necessary in order to predict the fracture behavior accurately.

A comparison of the fracture resistance plot for specimens with the CFM layer in Figure 3.22 with the similar plot for the specimens with the CSM layer in Figure 3.17, shows the interesting difference that the fracture resistance increases when turning toward more mode II for the CFM interface, whereas it decreases for the CSM interface. The crack may propagate along various positions in the CSM or CFM layer, e.g. in the centre or near the outer edge, and the position of the crack influences the amount of fibre bridging observed in the experiment. It is found that increased fibre bridging entails a larger steady state fracture resistance (since it shields the crack tip from the loading). It is characteristic of the fracture of sandwich specimens with CSM that the fibre bridging is relatively heavy for most mode I dominating loadings, whereas for more slidingly dominated crack openings the crack moves to the outer region of the CSM laminate with a smaller amount of fibre bridging. Conversely, the CFM layer is approximately 0.5 mm thicker and more resin-rich and a somewhat more mode II influenced loading is required to make it favourable for the crack to kink into the

centre of this layer.

The stresses in the tangential direction σ_t, see subplot (b) in Figures 3.19-3.21, are typically an order of magnitude larger than the stresses in the normal direction σ_n, see subplot (a). σ_t is measured as the slope of the fracture surface in the δ_t direction according to Eq. (3.3), and considering the fracture resistance surface at a fixed δ_n^* value in Figure 3.17, the change in J is large even though δ_t^* only changes negligibly, which causes the high values of the derived shear stress σ_t. The approach adopted for extracting the cohesive laws assumes that the cohesive stresses depend only on the local openings δ_n^* and δ_t^* and not the opening path, see Eqs. (3.2) and (3.3). This assumption may be doubtful for the considered case, since the steady state fracture toughness is governed by the amount of fibre bridging, which depends on the interlaminar position of the crack in the CSM or CFM layer (e.g. in the centre or near the outer edge). The position of the crack is dependent on the mode-mixity history, and thus the steady state fracture toughness will consequently not be path independent. To explain this further, consider the schematic illustration in Figure 3.25. Here the opening of the pre-crack tip between point A and B is illustrated and the opening may occur along either path 1 or path 2. Since the position of the crack in the CSM or CFM layer depends on the mode-mixity φ_δ, the amount of fibre bridging and hence obtained fracture resistance J_R may be considerably different for path 1 and 2 and thus the assumption of path independence should be taken with reservation. However, as the opening displacement is close to pure mode I ($\delta_t/\delta_n \simeq 0$) the sliding displacement is negligible and the normal stresses can be derived from (3.3). Furthermore, the energy dissipated near the crack tip J_o and the steady state fracture resistance J_{ss}, which may be obtained from the fracture resistance surfaces are valid, also for the mixed-mode cases, since these do not rely on the path independence assumption described above.

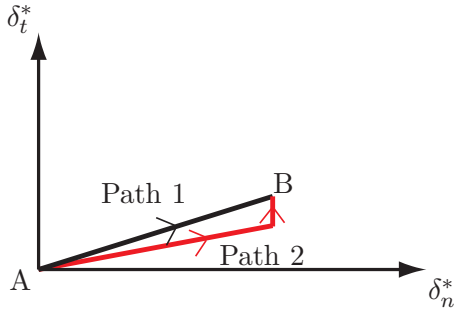

Figure 3.25: Schematic illustration of various crack opening paths going from point A to B.

The cohesive law in Figure 3.23 (c) indicates that there is compression stresses between the cracked faces as they are separating. This entails that stresses are pushing the separating faces apart, which is not physically plausible (unless in a case where loading is highly mode II and fibres might resist closure of the crack). For each of the DCB-UBM experiments the fracture resistance increases as the process zone develops due to fibre bridging, which indicates positive (tensile) tractions between separating faces, and the observed negative stress is believed to be a result of the path independence assumption. Consider the fracture resistance surface in Figure 3.22: As to one of the four black lines representing the conducted

experiments, J_R increases with increasing δ^*, however, when moving along the δ_n^* direction of the surface the slope is negative in some areas, hence the negative normal stresses in Figure 3.23. This will be taken into consideration in the implementation of the measured cohesive laws in the finite element code described later.

Generally, the crack propagates in jumps of 2-5 cm, which is different from results reported in e.g. Sørensen and Jacobsen (2003), where the crack propagates steadily for monolithic composite DCB-UBM specimens. It is believed that this behaviour is characteristic of foam-cored sandwich material, since the behaviour is also observed in Østergaard et al. (2007). It is assumed that unstable crack growth is obtained if

$$\frac{dJ}{da} > \frac{dJ_c}{da} \tag{3.18}$$

where (for LEFM conditions) J is the energy release rate, J_c is the critical energy release rate and a is the crack length. As the crack propagates the force in the wire is relaxed leading to a decrease in the crack driving force. Since the crack length does not enter the expression for the J integral, see Eq. (3.14), the observed unstable crack growth implies that the fracture resistance along the interface of the specimen is not constant or that it is affected by the crack tip propagation rate, i.e. the fracture resistance decreases with crack tip speed. In Sun et al. (2008) it was found that for adhesively bonded steel sheets the fracture toughness decreased during unstable crack growth compared to quasi-static crack growth. One explanation suggested is that plastic deformation ahead of a stationary crack may cause blunting of the crack tip with a consequent increase in energy release rate required to propagate the (stationary) crack. Only the peaks are considered from the measured fracture resistance data, see Figure 3.14, and it could therefore be argued that this is an unconservative measure of the actual average fracture resistance during crack growth. It is, however, not possible to measure high-rate fracture resistance by the conducted test method, and further attempts to clarify this are not made in this thesis.

It is found that the width of the specimens has an effect on the measured fracture resistance, see Figure 3.24. As the cracked surfaces separate bridging fibers cross in various direction including across the width of the specimen, thus a larger width of the specimen may entail more fibres in the bridging zone. In addition, the bonding of the specimen near the edges may be weakened due to cutting the specimens, which further leads to reduced fracture resistance for small specimens. It is believed that the effect will eventually decrease as the specimens become very large, and a certain steady-state width, where increasing the size of the specimen does not lead to increase fracture resistance, may be reached.

The test method developed and analysed in this chapter is used to characterise the fracture behaviour of various interfaces by mapping the crack kinking behaviour for various mode mixities, which is described in Chapter 4. The cohesive laws derived in this chapter are implemented in a commercial finite element software ABAQUS, and later used to predict fracture of a structural component, where the mode-mixity is varying during crack propagation. The procedure for implementing the cohesive laws is described in Chapter 5.

3.4 Summary

A method for extracting mixed-mode cohesive laws for sandwich structures using a modified DCB-UBM specimen is proposed and analysed. Large deflections are reduced by adhering a stiff layer to the sandwich faces. The opening of the pre-crack tip is measured by digital image correlation, and by employing the J integral, the fracture resistance J_R is measured as a function of normal and tangential openings of the pre-crack tip δ_n^* and δ_t^*. A surface plot is generated by linear interpolation between the measured J_R vs. the δ_n^* and δ_t^* curves obtained for different mixed-mode loadings. Traction-separation laws in the normal and tangential directions are extracted by partial numerical differentiation of the fracture resistance surface. Some consistency is observed regarding the cohesive laws, and it is found that the maximum stress level near the crack tip is in the range of 5.1-5.7 MPa for the CSM configuration and between 3.8 and 11.1 for the CFM case, however these values should be taken with reservation. The stress in the process zone where fibre bridging occurs decreases from 0.2 MPa to zero as the crack opens from 0.5 to 10 mm. The accuracy of the approach is discussed along with the variation in fracture behaviour for two different tested materials.

This page is intentionally left blank.

Chapter 4

Design of the Face/Core Interface for Improved Fracture Resistance

This chapter concerns measuring the fracture behaviour of sandwich specimens with various embedded laminate layers near the interface by use of the modified sandwich DCB-UBM specimen described in Chapter 3. The overall aim is to investigate whether it is possible to control the crack kinking behaviour and to increase the damage tolerance of sandwich structures with face/core debonds by the use of proper choice of interface layers.

4.1 Background and Objectives

The following describes the background and some recent work relevant to this study.

4.1.1 Background

A face/core debond crack in a sandwich structure can propagate in three basic ways: 1) propagate self-similarly at the face/core interface, 2) kink into the core or 3) kink into the face, see illustration in Figure 4.1. The least critical scenario from the designers' point of view depends on the circumstances. Crack kinking into and perhaps through the face laminate might be preferable since then the face/core interface crack will disappear from the structure, and there is no risk of further spreading throughout the structure. In other cases crack penetration of the load-carrying laminate might be crucial, and it is preferable that the crack remains in the interface and perhaps is being arrested by bridging fibres. Regardless of the preferred scenario, it is an aim to develop procedures for determining the crack kinking behaviour for various mixed-mode loadings and to use observations to improve the damage tolerance of sandwich structures.

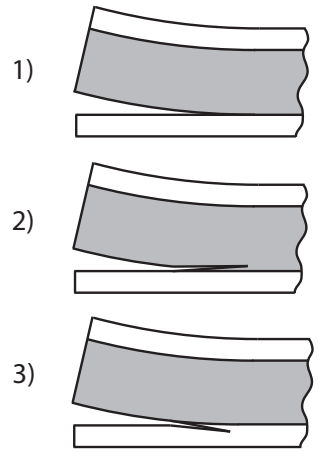

Figure 4.1: Schematic illustration of possible crack propagation paths in a sandwich specimen. 1) crack propagates in interface, 2) crack kinks into core, and 3) crack kinks into face.

The crack path is influenced by the stress state at the crack tip (e.g. characterised by the mode-mixity) and the fracture toughness of the face, core and interface, see Berggreen et al. (2007b). If the interface is sufficiently weak and brittle compared to the core and face laminate, the crack may propagate in the interface regardless of the mode-mixity. If on the other hand the interface is very tough, the crack may kink into the core or face laminate. Thus, with regards to damage tolerance considerations, the "weakest link in the chain" should be identified, since the crack tends to propagate where the resistance is smallest. Hence, the interface region should ideally be carefully tailored in accordance with the fracture properties of the face, core and interface.

Many previous studies have dealt with crack kinking either into or out of an interface. Cook and Gordon (1964) used a stress-based approach to analyse a mode I crack in a continuum approaching a weak plane perpendicular to the crack direction. They concluded that, if the strength of the weak plane is less than 1/5 of the strength of the continuum material ahead of the crack tip, the crack will deflect into the weak plane. Otherwise the crack will cross the interface and continue on the other side. A study by He and Hutchinson (1989) considers a similar problem using a toughness-based fracture criterion, i.e. LEFM. The study compares the energy release rates as the crack extends across the interface or deflects along the interface, and the condition for crack deflection can be written as

$$\frac{\Gamma_i}{\Gamma_m} < \frac{\mathcal{G}_i}{\mathcal{G}_m} \tag{4.1}$$

where Γ_i/Γ_m is the ratio between the fracture toughness of the interface and the material the crack penetrates, and $\mathcal{G}_i/\mathcal{G}_m$ is the ratio between energy release rates for crack deflection along the interface and extension across the interface. Parmigiani and Thouless (2006) used a cohesive zone model to examine a similar problem, see Figure 4.2. The cohesive zone model is capable of incorporating both strength and toughness parameters simultaneously, and it is shown that both are important to the crack deflection problem. Parmigiani and

Thouless (2006) explored whether the crack would deflect along the interface or extend across the interface for various regimes of Γ_m/Γ_i and σ_m^o/σ_i^o, where σ_i^o is the tensile strength of the interface and σ_m^o is the tensile strength of the material across the interface ahead of the crack tip. An interesting observation from this study is that there is no lower bound for Γ_m/Γ_i to guarantee crack extension across the interface, i.e. no matter how tough the interface is compared to the material ahead of the crack tip, crack deflection into the interface can always appear if σ_m^o/σ_i^o is sufficiently large. Conversely, there is a lower bound for σ_m^o/σ_i^o below which penetration is guaranteed regardless of the toughness ratio (Parmigiani and Thouless (2006)).

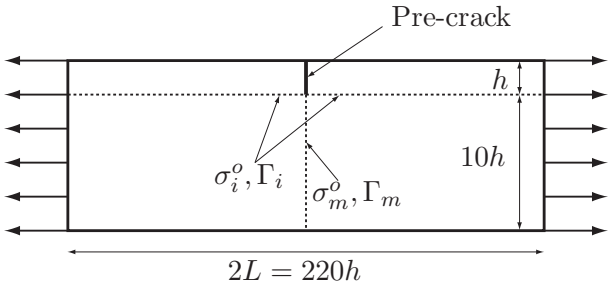

Figure 4.2: Geometry used to predict the crack path for various regimes of Γ_m/Γ_i and σ_m^o/σ_i^o in Parmigiani and Thouless (2006).

The assumption proposed by Parmigiani and Thouless (2006) that the crack path is characterised by the toughness and strength ratios between the interface and the adjacent materials is adopted for a sandwich face/core interface. The crack may either continue along the interface or kink into the adjacent face or core, and it is assumed that the tendency of the crack kinking out of the interface will increase if Γ_m/Γ_i or σ_m^o/σ_i^o decreases. For a crack with LSB it is important to acknowledge that Γ should be a measure of the crack tip toughness, i.e. not the steady state fracture resistance, which is a combination of both crack tip toughness and fracture resistance due to bridging fibres in the crack wake. Since large-scale bridging appears behind the crack tip and transfers relatively small stresses, bridging will not have a significant influence on the crack kinking behaviour, which is dictated by the stress state right in front of the crack tip. Conversely, bridging may increase the fracture resistance remarkably, so potentially the steady state fracture resistance of a face/core interface can be increased (by increasing the fibre bridging) without increasing the tendency of the crack kinking out of the interface. This is useful if it is desired to keep and arrest the crack in the interface, which is assumed in this study.

In several sandwich applications a mat with randomly oriented fibres is inserted between the core and face. The purposes of this mat are: (1) to increase the resin flow near the core during production and thus avoid any dry areas, (2) obtain a more gradually changing stiffness from the compliant core to the stiff face, and (3) a mat with randomly oriented fibres is an effective source for fibre bridging, since fibre bundles are relatively easily being pulled out of the mat. Two various mat types with randomly oriented fibres are considered: Chopped Strand Mat (CSM) and Continuous Filament Mat (CFM), where the CSM consists of 4-6 cm long fibres bundled together and the CFM consists of very long fibre bundles (in principle continuous).

In an experimental study by Cantwell and Davies (1996) sandwich specimens with and without a CSM inserted in the face/core interface were compared for sandwich beams with GFRP faces and balsa cores. For the interface without CSM the crack propagated in the face/core interface, whereas for the specimen with CSM the crack propagated within the CSM layer with an energy release rate 30 % lower than the specimens without CSM. In Truxel et al. (2006) a CFM was inserted in the face/core interface of sandwich specimens with glassfibre/vinylester faces and either balsa or H200 foam core. The CFM layer generated a resin-rich layer where the crack propagated with large-scale bridging. Approximately the same fracture toughness was obtained as for equivalent specimens without CFM.

It is an advantage of the layer with randomly oriented fibres that the interlaminar fracture toughness is the same in all directions, which is generally not the case for laminates with straight fibers. Solaimurugan and Velmurugan (2008) showed that for unidirectional laminates the fibre direction has a large influence on the interlaminar fracture toughness, where e.g. a delamination between two unidirectional laminates oriented 45^o and -45^o relative to the crack propagation direction was 2.4 times tougher than a 0/0 interface. The authors pointed out that the crack travels along the fibre direction, which may lead to increased crack propagation length and amplified fracture toughness. For a debond present in a large panel the crack might propagate in any direction relative to the fibre direction, and the fracture toughness of the propagating crack is difficult to predict. For a crack propagating in a CSM or CFM layer the fracture toughness is not affected by the in-plane crack direction and the damage tolerance is easier to predict.

4.1.2 Objectives

To illustrate the main idea behind this chapter a schematic example is given in Figure 4.3. This illustrates how the fracture resistance of an interface crack is potentially increased by inserting a CSM layer in the interface. It is assumed that the crack propagates along the path where the crack tip fracture toughness is smallest, i.e. the smallest value of J_o^{face}, J_o^{core} and J_o^{CSM}, respectively. For the interface without CSM, see Figure 4.3 (a), $J_o^{core} < J_o^{face}$ and it is likely that the crack will propagate in the core, with the energy release rate equal to J_o^{core} (since the process zone in the core is small $J_{ss}^{core} = J_o^{core}$). Regarding the interface with CSM illustrated in Figure 4.3 (b), $J_o^{CSM} < J_o^{core}$ and it is likely that the crack will propagate in the CSM layer. This entails large-scale fibre bridging and the total fracture resistance increases to $J_{ss}^{CSM} > J_o^{core}$. It is therefore possible that the CSM layer causes a more damage tolerant interface.

The example above is based on the fracture toughness alone and, as deduced from the study by Parmigiani and Thouless (2006), the crack path is influenced both by the fracture toughness and the strength of the face, core and CSM layer. In Figure 4.4 it is illustrated how both the strength and crack tip toughness parameters σ_o and J_o of the face, core and interface may vary independently. Furthermore, the crack path may be influenced by the microstructure of the materials and variations in production variables. The kinking

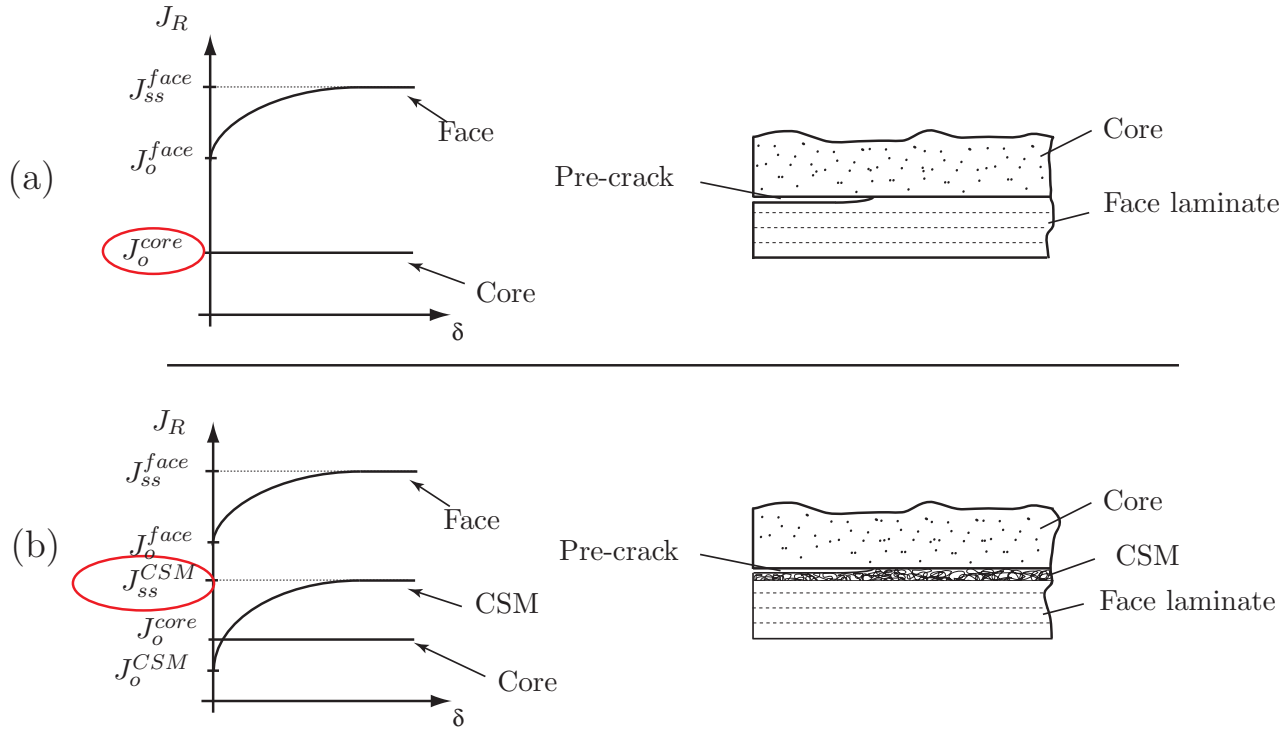

Figure 4.3: Possible fracture resistance curves for (a) UD/core interface and (b) interface with CSM. The red circle marks the steady state fracture toughness equal to the crack driving force necessary to propagate the crack when the process zone has evolved.

behaviour of a sandwich interface crack is sensitive to many parameters, and it is tedious to predict the fracture behaviour from analytical or numerical models of the microstructure, thus reliable experimental approaches are necessary. The aim of the work described in this chapter is to demonstrate the use of the sandwich DCB-UBM specimen described in Chapter 3 for characterising the fracture behaviour regarding fracture resistance and crack kinking for various mixed-mode loadings.

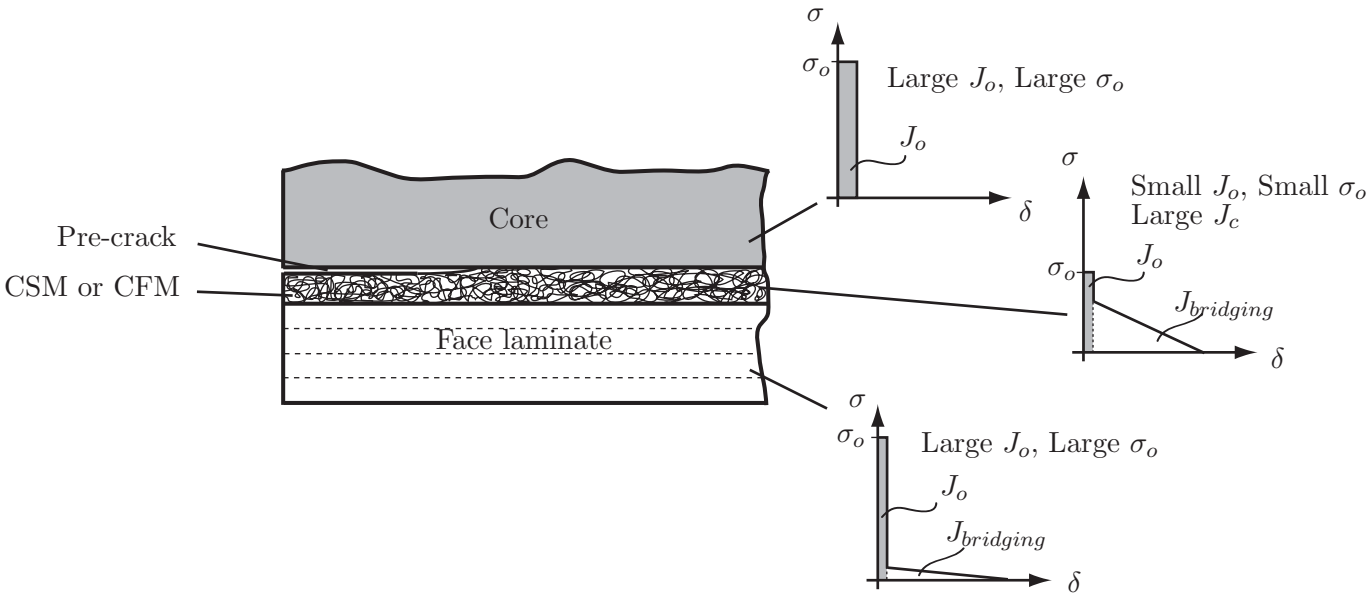

Figure 4.4: Schematic illustration of an interface design that promotes crack propagation in the CSM or CFM layer. The crack path is governed by mode-mixity of the loading and the fracture properties of the individual layers i.e. the maximum stress and crack tip fracture toughness (illustrated as the shaded area of the cohesive laws).

Furthermore, an example is given on how modifying the sandwich interface can influence the crack path and hereby improve the fracture toughness. A thin woven layer is incorporated in the interface during production acting as a crack kinking stopper. The woven layer is inserted between the quadraxial and the CSM or the CFM mat to create a mechanical "wall" with a relatively high in-plane toughness and strength which is difficult to penetrate. The lay-up sequence of a sandwich interface with a CSM or CFM layer and an additional woven mat is illustrated in Figure 4.5.

4.2 Numerical Analysis

The test-method used for determining the fracture behaviour of the various tested materials is a modified Double Cantilever Beam loaded by Uneven Bending Moments (DCB-UBM). In Chapter 3 the analysis of the specimen and the procedure for employing the J integral are described and mixed-mode cohesive laws for sandwich specimens with a crack propagating in

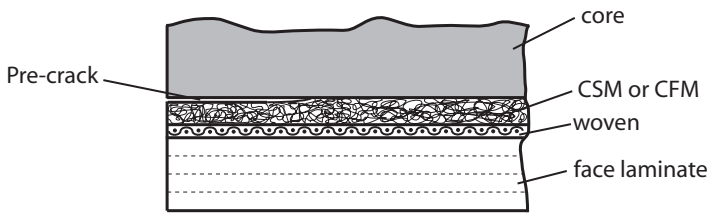

Figure 4.5: Schematic illustration of lay-up sequence in tested sandwich interface.

the CSM or CFM layer are presented. In the following a numerical model of the DCB-UBM specimen is utilised to extract the mode-mixity of the DCB-UBM specimen at various M_1/M_2 ratios. It is an aim to described the mode-mixity in a geometry independent way, hereby permitting prediction of the kinking behaviour by transferring results from one geometry to the other, as will be conducted in Chapter 5.

4.2.1 Mode-mixity of Test Specimen

The DCB-UBM specimen allows loading of the crack tip by various mode mixities from pure mode I to pure mode II by changing the moment ratio M_1/M_2, and it is found that the fracture mechanisms such as fibre bridging and crack kinking vary with mode-mixity. A finite element model is generated in order to extract the mode-mixity as a function of moment ratio M_1/M_2. The model is 2-D, plane strain and the same general assumptions as described in Section 2.2 prevails. A schematic sketch of the geometry and boundary conditions used for the finite element model of the DCB-UBM specimen is illustrated in Figure 4.6. Zero thickness cohesive elements connect continuum elements along the interface except at the pre-crack of 65 mm where no bonding exists between the face and core. The nodes on the right end of the steel bars are fixed, while moment loads are applied to the left side of the specimen (see Figure 4.6). The nodes have no rotational degrees of freedom and moments are applied to the structure by introducing coupling constraints between the nodes at the left steel edge in a master/slave configuration, so that moment loading applied to the master node will cause equal rotation of the entire edge. The mesh consists of three- and four-sided elements with a refinement near the interface and the smallest elements have a side length of 0.25 mm, see the similar mesh refinement in Figure 2.12. The moment loading is increased load controlled from zero until the crack propagates, and at all times a constant moment ratio M_1/M_2 is sustained. In the results dynamic effects can be neglected, i.e. the ratio between global kinetic and elastic energy $E_{kin}/E_{el} < 0.01$.

In order to conduct the simulations and extract the mode-mixity a traction-separation law needs to be prescribed for the cohesive elements in the finite element model. Cohesive laws were determined in Chapter 3 for sandwich specimens with CSM and CFM embedded between face and core, and an idealised cohesive law similar to the determined ones is used as input in the finite element model, see Figure 4.7. Results depend on the assumed shape of

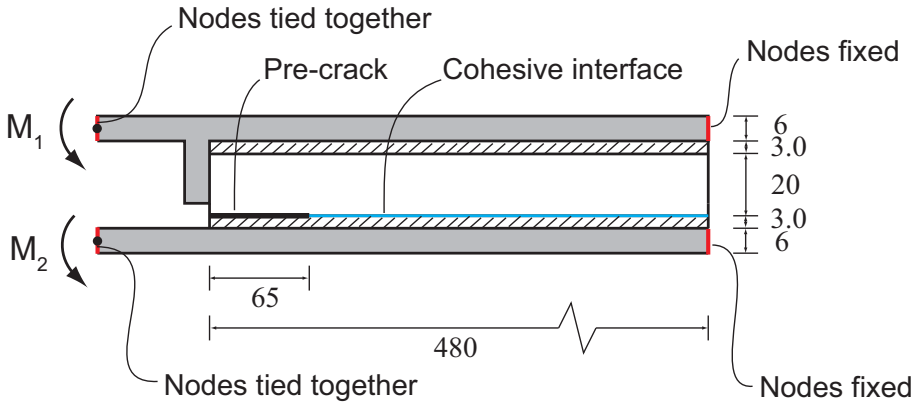

Figure 4.6: Geometry and boundary conditions of the finite element model (dimensions in mm).

the cohesive law, however, it was found that the mode-mixity varied below 3 % as the shape was changed from the one illustrated in Figure 4.7 to triangle-shaped with the same fracture toughness and critical stress (at a moment ratio of $M_1/M_2 = 0$). Thus, it is believed that the idealised cohesive law assumption during calculation of mode-mixities will not affect results substantially. The cohesive law from Figure 4.7 is used for both pure mode I and II and the coupled mixed-mode behaviour is described by Eqs. (2.9), (2.10) and (2.11).

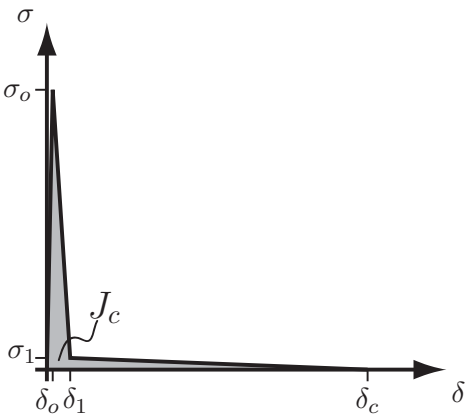

Figure 4.7: Pure mode I and II cohesive law used in simulations of DCB-UBM specimen; $\delta_o = 9$ μm, $\delta_1 = 0.2$ mm, $\delta_c = 10$ mm, $\sigma_o = 5.5$ MPa, $\sigma_1 = 0.15$ MPa and $J_c = 1300$ J/m^2.

For a cohesive zone model, there is no singular stress field, and the conventional LEFM mode-mixity measure based on stress intensity factors is not useable. Instead various other mode-mixity measures related to the displacements and stresses in the process zone may be used. For cases with large-scale bridging it is believed that crack kinking is mainly governed by the processes at the crack tip and less by the bridging behaviour in the process zone. Thus, a mode mixity measure which characterises the stresses at the crack tip is introduced:

$$\varphi_o = \frac{2}{\pi} \tan^{-1} \left(\frac{\sigma_t^o}{\sigma_n^o} \right) \tag{4.2}$$

where σ_t^o and σ_n^o are the tangential and normal stresses of the cohesive element at the crack tip (leading edge of the process zone). φ_o varies between 0 and 1, where $\varphi_o = 0$ indicates pure mode I conditions and $\varphi_o = 1$ pure mode II. It is believed that (4.2) is a useful mode-mixity measure for predicting crack kinking for various geometries based on observations from the DCB-UBM experiments, which is conducted in Chapter 5. φ_o will be used extensively as a mode-mixity measure throughout the remaining part of this chapter.

Due to the concept of loading by pure bending moments, the mode ratio at the crack tip is unchanged as the crack propagates and φ_o is approximately constant once the process zone is fully developed. Thus, each tested moment ratio M_1/M_2 can be associated with a fixed φ_o. However, the mode-mixity varies considerably between the crack tip and elsewhere in the process zone as illustrated in Figure 4.8. Here $\varphi = 2/\pi \tan^{-1}(\sigma_t/\sigma_n)$ is plotted as a function of the x-coordinate with σ_t and σ_n being the current shear and normal stresses of the cohesive elements in the process zone. Note that the variation of φ is large in the vicinity of the crack tip, whereas it is approximately constant far from the crack tip. Furthermore, φ is relatively mode II dominated at the crack tip and becomes increasingly mode I with increasing distance to the crack tip.

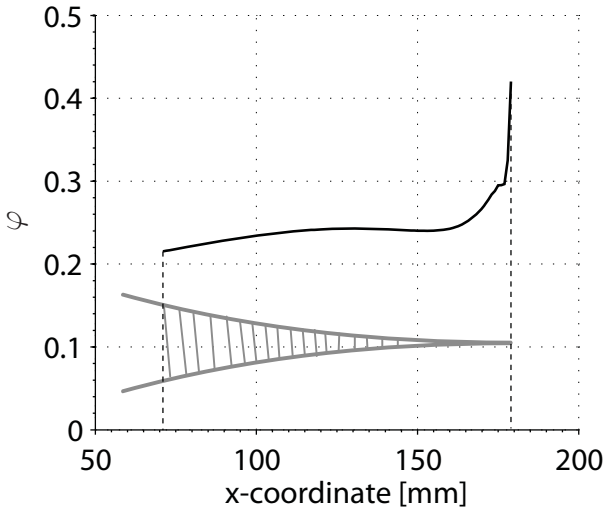

Figure 4.8: Numerically found mode-mixity φ as function of x-coordinate inside the process zone of a loaded DCB-UBM specimen after reaching steady state. For the considered case the moment ratio $M_1/M_2 = 0$ and the cohesive law is illustrated in Figure 4.7.

Generally, when conducting cohesive zone modelling in ABAQUS, a cohesive law is prescribed as function of mode-mixity which is either energy based (see Section 2.2.3) or stress based. In both cases ABAQUS averages the mode-mixity over the loading history of the cohesive element. As described above, it is believed that the fracture resistance is sensitive to the interlaminar position of the crack, which is governed by the stress situation at the crack tip rather than the average stresses in the crack wake. The crack tip mode-mixity may be significantly different from the average one, and the link between them depends on the geometry of the specimen. The average mode-mixity for the DCB-UBM specimen is found

from

$$\varphi_\sigma = \frac{1}{(j_{max} - j_{min})} \sum_{j_{min}}^{j_{max}} 2/\pi \tan^{-1}\left(\sigma_t^j/\sigma_n^j\right) \tag{4.3}$$

Only output steps[1] where the considered cohesive element is in the process zone enter the summation in (4.3), i.e. j_{min} is the first output step number where the cohesive element appears in the process zone and j_{max} is the last. σ_t^j and σ_n^j are the tangential and normal tractions in the considered cohesive element at output time step number j. In Figure 4.9 φ_o and φ_σ are plotted for various moment ratios M_1/M_2.

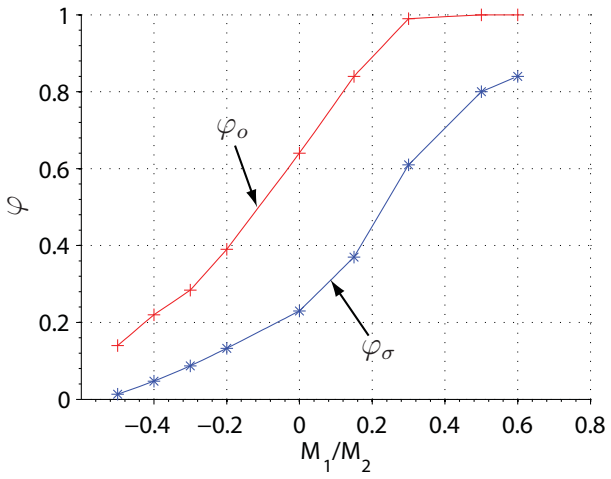

Figure 4.9: Numerically found mode-mixities, where φ_o is at the crack tip (leading edge of the process zone) and φ_σ is the average mode-mixity of the process zone, see Figure 4.8, both as a function of applied moment ratio M_1/M_2.

It should be noted, that the relation between moment ratio and mode mixity in Figure 4.9 depends on the geometry and elastic properties assumed for the test specimen. Different geometry and/or elastic properties would give different (however probably similar) results.

Generally the sign of φ is chosen to depend on the shear direction, so that $\varphi > 0$ as the sliding direction encourages crack kinking into the face and $\varphi < 0$ as crack kinking into the core is encouraged. Only moment ratios in the interval -0.5 to 0.6 are considered in Figure 4.9, since specimens were only tested within this range. The mode-mixities φ_o and φ_σ in Figure 4.9 are used to characterise the fracture of the DCB-UBM specimen in order to predict the fracture behaviour of a sandwich component described in Chapter 5.

Both Figure 4.8 and Figure 4.9 show that $\varphi_\sigma < \varphi_o$ and it is found that both mode mixity measures increases with M_1/M_2. For the tested moment ratio M_1/M_2 between -0.5 and 0.6

[1]The total simulation time domain consists of 200 evenly distributed output steps, in which the finite element program writes results to a file.

φ_o varies between 0.14 and 1.0, whereas φ_σ varies between 0.01 and 0.84. The difference between φ_σ and φ_o is approximately constant 0.16, and comments regarding the distribution of φ inside the process zone at various moment ratios is given in Section 4.4.3.

4.3 Experiments

4.3.1 Materials and Lay-up

Sandwich panels with glass fibre faces and foam cores are manufactured using resin vacuum infusion, and a 12.5 μm thick slip film is inserted between part of the face and core to define the pre-crack. The polyester resin is Polylite® 413-575, which is specially designed for vacuum injection due to its low viscosity. The sandwich faces consist of four DBLT quadraxial mats from Devold Amt, each with a dry area weight of 850 g/m^2 and the fibre directions relative to the longitudinal direction of the specimen [90,45,0,-45], where the -45 degree ply is placed closest to the core. Either a CSM or CFM with an area density of 450 g/m^2 is inserted between the core and the quadraxial laminates, during production. The total face thickness after production is approximately 3.0 mm for laminates with CSM and 3.5 mm for laminates with CFM. Even though the CSM and CFM layer has identical dry weight area densities, the CFM layer has a larger volume and generates a space between the face and core, which is filled with resin during production, thus making the face approximately 0.5 mm thicker compared to the CSM.

For some specimens an additional woven mat is inserted between the CSM or CFM and the face. Two different woven mats are considered, both consisting of plain weave, but various coarseness in weave strands, i.e. tex 68[2] and tex 300. Preliminary tests show that the tex value has an effect on the bonding between the woven mat and the adjacent laminate. Since the behaviour of the specimens was not known before the tests, the choice of which moment ratios M_1/M_2 (and consequently which mode-mixity loadings) to apply to the specimens was made progressively as the tests were conducted accordingly to the observed fracture behavior. The materials and loading parameters of all specimens are listed in Table 4.1 and photos of the various materials are shown in Figure 4.10.

It is the objective of this chapter to investigate the fracture behaviour of sandwich specimens with a CSM or CFM layer and to test the effectiveness of the woven mat to stop the crack from kinking into the adjacent face. Relevant results are described in the following section.

[2]Tex is the weight in grams of a 1000 m long single strand used in the weaving process, i.e. with the unit [g/1000 m]

Repetitions	Face	Layer	M_1/M_2	φ_σ	φ_o
3	quadraxial	CSM	-0.5	0.013	0.14
3	quadraxial	CSM	0.0	0.20	0.64
4	quadraxial	CSM	0.2	0.39	0.98
3	quadraxial	CFM	-0.5	0.013	0.14
3	quadraxial	CFM	-0.2	0.13	0.39
3	quadraxial	CFM	0.0	0.20	0.64
3	quadraxial	CFM	0.15	0.35	0.84
3	quadraxial	CSM + tex 68	-0.5	0.013	0.14
3	quadraxial	CSM + tex 68	0.0	0.20	0.64
1	quadraxial	CSM + tex 68	0.15	0.35	0.84
3	quadraxial	CSM + tex 68	0.2	0.39	0.98
3	quadraxial	CFM + tex 68	-0.5	0.013	0.14
4	quadraxial	CFM + tex 68	-0.2	0.13	0.39
3	quadraxial	CFM + tex 68	0.0	0.20	0.64
3	quadraxial	CFM + tex 68	0.15	0.35	0.84
3	quadraxial	CSM + tex 300	-0.4	0.047	0.22
3	quadraxial	CSM + tex 300	-0.2	0.13	0.39
3	quadraxial	CSM + tex 300	-0.12	0.18	0.49
3	quadraxial	CSM + tex 300	0.0	0.20	0.64
3	quadraxial	CSM + tex 300	0.2	0.39	0.98
1	quadraxial	CSM + tex 300	0.3	0.68	0.99
2	quadraxial	CFM + tex 300	-0.4	0.047	0.22
3	quadraxial	CFM + tex 300	-0.3	0.087	0.28
3	quadraxial	CFM + tex 300	-0.12	0.18	0.49
3	quadraxial	CFM + tex 300	0.0	0.20	0.64
3	quadraxial	CFM + tex 300	0.15	0.35	0.84
3	only core	-	-1	0	0

Table 4.1: Various parameters for the 90 tested specimens, e.g. interface lay-ups, moment ratios, and corresponding average and crack tip mode-mixities φ_σ and φ_o found from simulation of the DCB-UBM specimen described in Section 4.2.1.

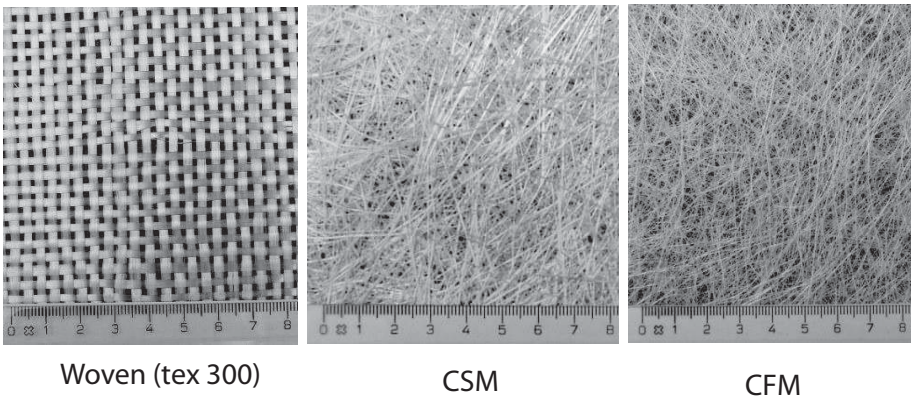

Figure 4.10: Photos of various laminates used in this study (unit on ruler is cm).

4.4 Results

Initially, some general observations are described regarding the crack propagation path. Subsequently, the measured fracture resistances are presented and a more detailed description of the fracture behaviour is given. Finally, in the discussion section the behaviour is commented on and analysed.

4.4.1 Observations regarding the Crack Propagation Path

As mentioned in the Introduction of this chapter, the crack may propagate in one of the following three ways: (1) the crack stays in the CSM or CFM layer, (2) the crack kinks into the core or (3) the crack kinks into the face. For the materials used in the present study all three regimes can be reached by varying the moment ratio M_1/M_2. In the cases where the crack kinks into the laminate the crack gradually jumps from one layer to the next, and the distance (in the crack propagation direction) between points where the crack changes layer varies between 2 and 10 cm, while the distances between kinking positions decrease with increasing φ_o. A picture of a specimen with a crack gradually kinking through the laminate is seen in Figure 4.11. It should be noted how the crack initially propagates in the resin between the CSM and the core for 2-3 cm, then in the CSM, then in the (-45)-degree layer and finally in the 0-degree layer. The 0-degree layer is not penetrated but in some experiments the crack continues on the other side of the 0-degree layer without breaking the fibres. A schematic illustration of the crack path is shown at the bottom of Figure 4.11.

It is an aim of this study to consider the effect of a woven mat on the tendency for crack kinking into the adjacent face. The woven layer is never penetrated by the crack and to some degree the woven layer succeeds in preventing the crack from kinking into the face. However, for mode II dominated cases, a secondary crack is initiated on the opposite side of the woven layer, which continues to propagate in the interface between woven layer and quadraxial layers without breaking the woven mat, see the picture in Figure 4.12. As the

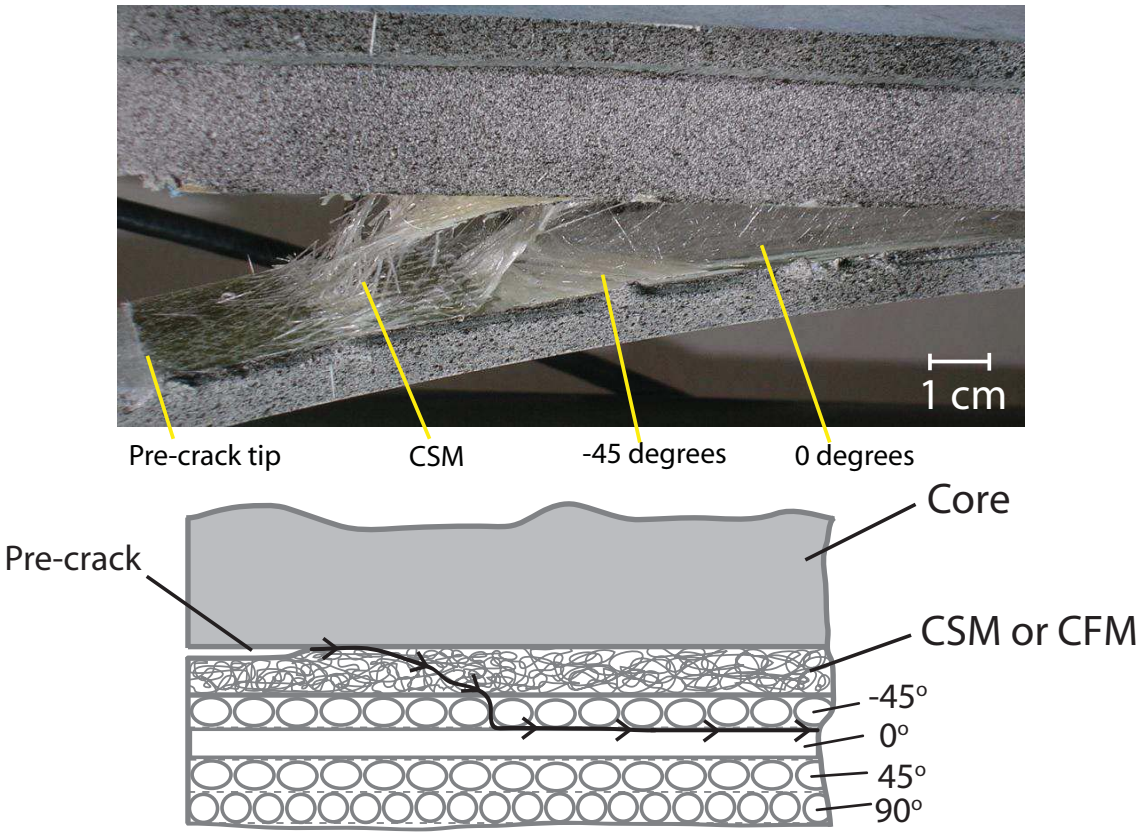

Figure 4.11: Photo and schematic illustration of loaded DCB-UBM specimen with CSM mat in the interface. A crack is gradually kinking through the CSM and face layers. The specimen has a CSM laminate, no woven layer and the moment ratio is $M_1/M_2 = 0.2$ equivalent to $\varphi_o = 0.98$.

crack continues on the other side of the woven mat it propagates with a relatively small fracture resistance, and particularly the fine-woven layer (tex 68) shows limited bonding capability with the adjacent face due to the relatively fine-textured surface of the woven layer. This behaviour is further described in Section 4.4.2.

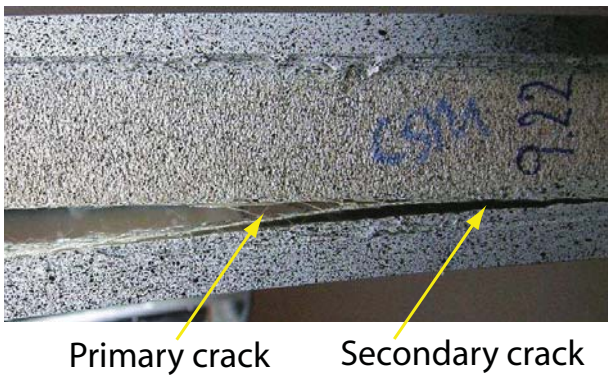

Figure 4.12: A crack jumping to the opposite side of the woven layer without penetration. The specimen shown is CSM+tex 300 loaded at $M_1/M_2 = 0.3$ corresponding to $\varphi_o = 0.60$.

Pictures of various fracture scenarios are shown in Figure 4.13 a)-d). Subplot a) shows crack propagation in the CFM layer under large-scale bridging. Subplot b) shows a test performed on the core materials with the purpose of determining the fracture toughness J_{core}. In this test the steel bars were adhered directly to the core material, a 60 mm long pre-crack was cut in the centre and the specimen was loaded by the moment ratio $M_1/M_2 = -1$. The average fracture toughness value of the H200 core material for three specimens was measured to $J_{core} = 2.5$ kJ/m^2. Subplot c) shows the cracked CSM + tex 68 specimen at $\varphi_o = 0.14$. In these tests the crack initially kinked into the core material and subsequently returned to the interface. Subplot d) shows the behaviour of the specimen with a CFM and no additional woven layer loaded at $\varphi_o = 0.14$. Here the crack kinked into the core material and continued to propagate in the core 2-3 mm from the interface throughout the experiment. Generally, the fracture behaviour was approximately identical for specimens tested with the same lay-up and applied moment ratio. The mentioned fracture scenarios are described further in the following section.

The mode I fracture toughness of the Divinycell H200 foam core is measured from the DCB-UBM experiments to 2.5 kJ/m^2, whereas Viana and Carlsson (2003) measured a fracture toughness of 1.3 kJ/m^2 also for H200 core material. However, through correspondence with the manufacturer of the core it has been discovered that since the paper by Viana and Carlsson (2003) was published, the core material has been altered, and the fracture toughness improved.

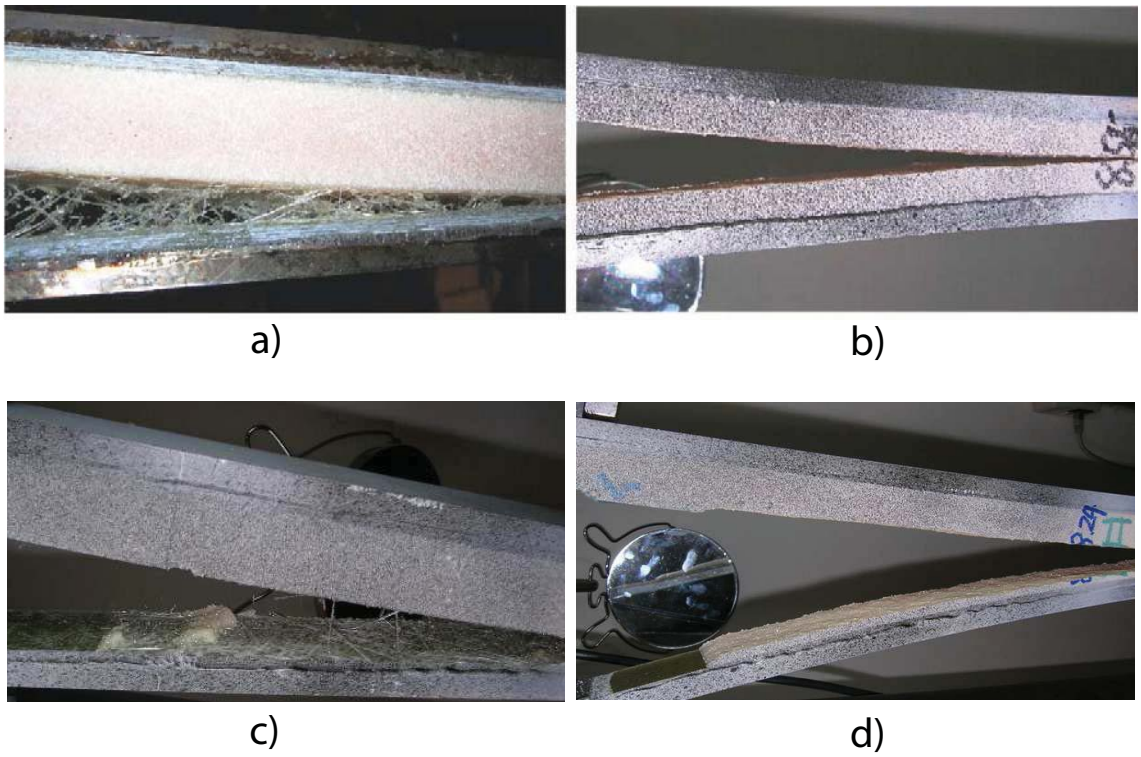

Figure 4.13: Photos of DCB-UBM specimens: a) specimen with a CFM layer loaded at a mode-mixity of $\varphi_o = 0.39$, while a crack is propagating in the CFM layer under large-scale bridging, b) specimen loaded in pure mode I with a crack propagating in the centre of the core, c) CSM + tex 68 at mode-mixity $\varphi_o = 0.14$ and a crack initially kinking into the core but subsequently quickly returning to the interface, and d) CFM loaded at $\varphi_o = 0.14$ and a crack propagating in the core 2-3 mm from the interface.

4.4.2 Fracture Resistance and Crack Kinking Transition Points

Generally, the fracture resistance as a function of pre-crack tip opening behaves as the plot shown in Figure 3.14 where J initially increases steeply before the pre-crack opens, then as the crack propagates large-scale fibre bridging may develop, leading to rising fracture resistance until a plateau is reached where $J_R = J_{ss}$. The steady state fracture resistance J_{ss} as a function of mode-mixity is plotted in Figure 4.14 for the six tested lay-ups: a) CSM, b) CFM, c) CSM + woven tex 68, d) CFM + woven tex 68, e) CSM + woven tex 300, and f) CFM + woven tex 300.

The pre-crack is positioned between the core and the CSM or CFM layer, see Figure 4.5. In Figure 4.14 the x-symbol is used to mark results where the crack propagated in the CSM or CFM layer, and the o-symbol indicates that the crack kinked into the face or core. The red x-symbol marks the load-cases where the crack kinked into the resin between the CSM or CFM layer and the woven, but did not cross the woven layer. The approximate transition where the crack starts to kink into the adjacent face (quadraxial layers) is marked with a vertical dashed line.

For the CSM layer in Figure 4.14 a) three mode-mixities are considered, $\varphi_o = \{0.14, 0.64, 0.84\}$. For two out of four specimens loaded by the mode-mixity $\varphi_o = 0.84$, the crack kinked into the quadraxial layers, whereas for all other specimens the crack stayed in the CSM layer. As the crack kinks into the quadraxial layers the measured fracture resistance increases substantially. Subsequently, consider the results for the CFM layer in Figure 4.14 b), regarding the mode-mixities $\varphi_o = \{0.14, 0.39, 0.64, 0.84\}$. In contrast to the specimens with CSM, a mode-mixity of $\varphi_o = 0.14$ leads to crack kinking into the core, with a measured fracture toughness of approximately 2.7 kJ/m^2, which corresponds approximately to the measured mode I fracture toughness of the core (2.5 kJ/m^2). At a mode-mixity of $\varphi_o = 0.39$ the crack propagates in the CFM layer with large-scale bridging and a steady state fracture resistance between 2.0 and 2.3 J/m^2. For the final two tested mode-mixities ($\varphi_o = 0.64$ and 0.84) the crack kinked into the quadraxial laminate, which entails increased fracture resistance compared to crack propagation in the CFM layer.

In Figure 4.14 c) and d) results are given for specimens with a relatively fine woven layer (tex 68) inserted between the CSM or CFM and the face. For the CSM layer in subplot c) the transition point where the crack kinks into the face is not found within the tested mode-mixity range. For $\varphi_o = 0.14$ the crack initially propagated in the core for 2-3 cm and then returned to the interface and remained here throughout the remaining part of the test, see Figure 4.13 c). Conversely, the CFM + tex 68 in subplot d) did not kink into the core at $\varphi_o = 0.14$ and possible explanations for the difference in kinking behaviour are discussed in Section 4.4.3. Based on the results shown in Figure 4.14 subplots a) and c), the woven tex 68 layer did have an effect on the transition point regarding crack kinking into the quadraxial layers for the CSM configuration, while no change was observed regarding the CFM configuration.

For the CSM+woven tex 300 in subplot e), specimens were tested at $\varphi_o = \{0.22, 0.39, 0.49, 0.64, 0.98, 0.99\}$ and only the mode-mixity of 0.99 showed kinking into the face. At

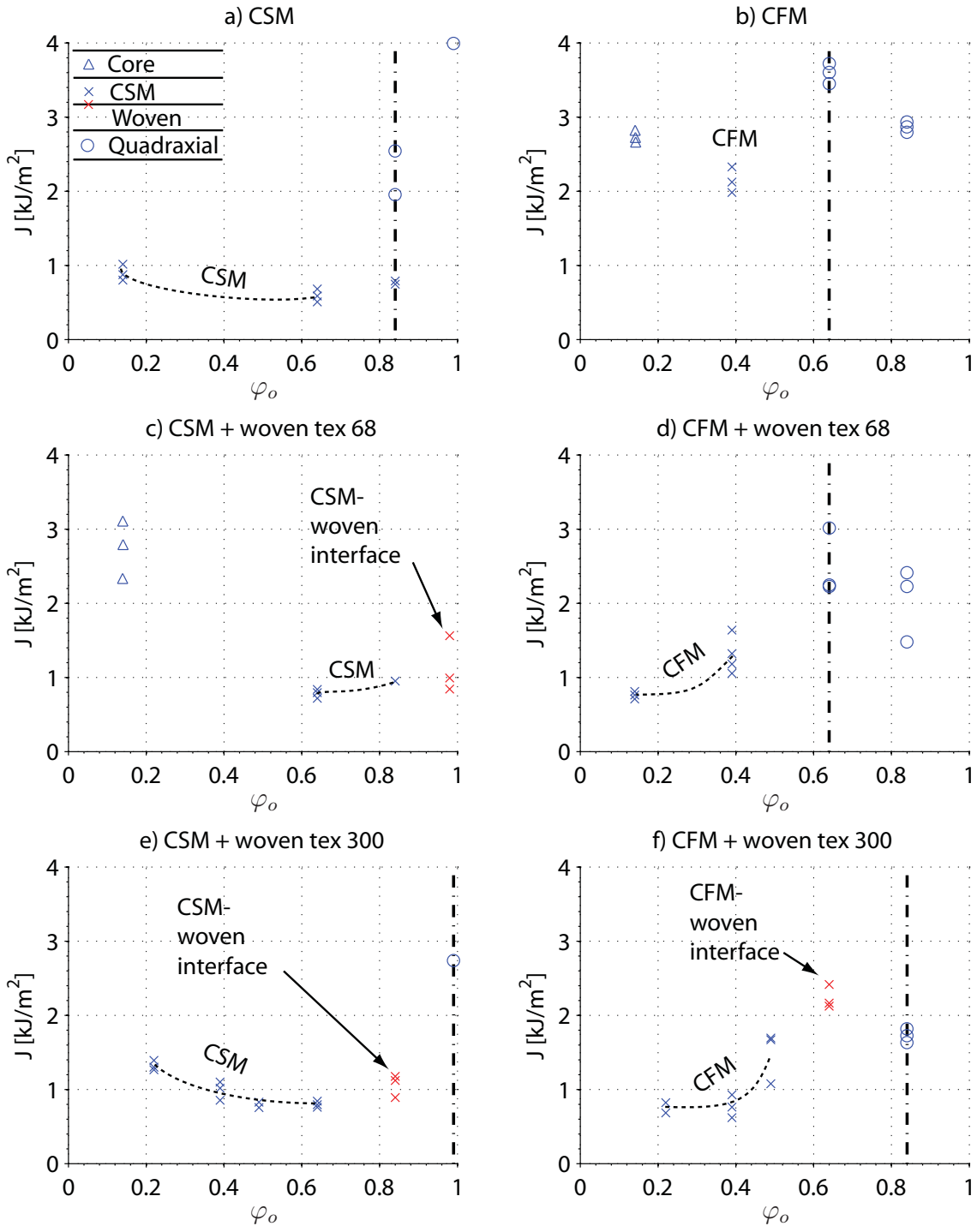

Figure 4.14: Steady state fracture resistance as a function of mode-mixity for tested sandwich specimens. The blue x-symbol indicates crack propagation in the CSM or CFM layer, the red x-symbol marks crack propagation in the interface between the woven and the CSM or CFM, the o-symbol is for crack kinking into the quadraxial layers, and the △-symbol indicates crack kinking into the core. The black dashed vertical line indicates the approximate transition where the crack kinked into the quadraxial layers.

a mode I dominated loading ($\varphi_o \simeq 0.2$), the crack propagated in the centre of the CSM, resulting in relatively dense fibre bridging, whereas a mode-mixity of $\varphi_o \simeq 0.6$ made the crack propagate in the outer edge of the CSM with less fibre bridging, and consequently less fracture resistance. The plot for the CFM + woven tex 300 laminate configuration shown in subplot f) illustrates a somewhat different behaviour compared to that of the CSM in subplot e). Here a mode I dominated loading leads to crack propagation in the resin between the core and the CFM layer. Only at more mode II dominated loadings the crack starts kinking into the CFM layer, which results in increased fibre bridging and fracture resistance. As the crack propagates in the centre of the CSM or CFM layer the steady state fracture resistance is approximately 1.4 and 2.4 kJ/m^2 for the CSM and CFM layer, respectively, and conversely as the crack propagates in the outer region of the layer the steady state fracture resistance is approximately 0.8 kJ/m^2 for both of them.

4.4.3 Discussion

The distribution of the mode-mixity φ in Figure 4.8 is interesting to study. The mode-mixity at the crack tip is relatively dominated by shear stresses whereas φ becomes increasingly mode I further back in the process zone and some distance behind the crack tip it reaches an approximately constant level. Both crack tip mode-mixity φ_o and average mode-mixity φ_σ are sensitive to the moment ratio M_1/M_2, see Figure 4.9, however, due to the distribution of φ in the process zone $\varphi_o > \varphi_\sigma$. A short explanation for the distribution of φ is given in the following. The DCB-UBM specimen may be considered as three individual beams, where beam 1 and 2 is separated by the crack, and beam 3 constitutes the intact part of the specimen, see Figure 4.6. The specimen is loaded by pure bending moments, and beam 1, 2 and 3 are loaded by moments M_1, M_2 and $-(M_1 + M_2)$, respectively, where the latter is found from equilibrium and constitutes the reaction from the end support. In the intact part of the specimen (ahead of the crack tip), the cohesive elements in the interface is loaded in pure shear inflicted by the bending of beam 3. Inside the process zone the stiffness of the cohesive elements degrade and the shear stresses due to bending of beam 3 are relaxed. Consequently, the ratio between normal and shear stresses becomes increasingly controlled by the deflections of beam 1 and 2. This is believed to be the reason for the observed distribution of φ inside the process zone.

In Section 3.1.2 an expression for the J integral as a function of geometry, elastic properties and applied moments is derived for a crack propagating in the interface. As the crack deflects from the interface and into the adjacent face or core the geometry changes and the expression for J should be taken with reservation. However, due to the thick steel bars adhered to the face laminates, the J integral value is not changing radically as the crack tip changes path. It was shown by the plot in Figure 3.7 that a change in the laminate thickness of 17 % only results in a J value deviation of 5 %, and the J integral is therefore still valid within some reasonable margin of error. Conversely, as a second crack is initiated on the opposite side of the woven layer, and instead of a single crack tip the problem is changed into three

competing crack tips, see Figure 4.12, the J integral obtained in Section 3.1.2 can no longer be related to the fracture resistance of the material.

The H200 core considered in this study has a relatively high fracture toughness ($J_{core} = 2.5$ kJ/m^2) compared to the steady state fracture resistance of the CSM or CFM layer (between 0.8 and 2.4 kJ/m^2), thus crack propagation in the core material leads to superior fracture resistance compared to the CSM or CFM layers. This was not expected before conducting the tests, since earlier studies e.g. by Viana and Carlsson (2003) measured the fracture toughness of H200 core to 1.3 kJ/m^2. As described in Section 4.1.2, the true potential of the designed interface is only obtained as the steady state fracture resistance of the CSM or CFM layer is larger than the fracture toughness of the core, see Figure 4.15, and the proposed interface design would be more advantageous when used in structures with lighter and brittler cores. A schematic illustration of the fracture behaviour of the CSM or CFM layer along with the fracture toughness of the core is shown in Figure 4.15. This hypothesis is not pursued further in this study but may be investigated in future work.

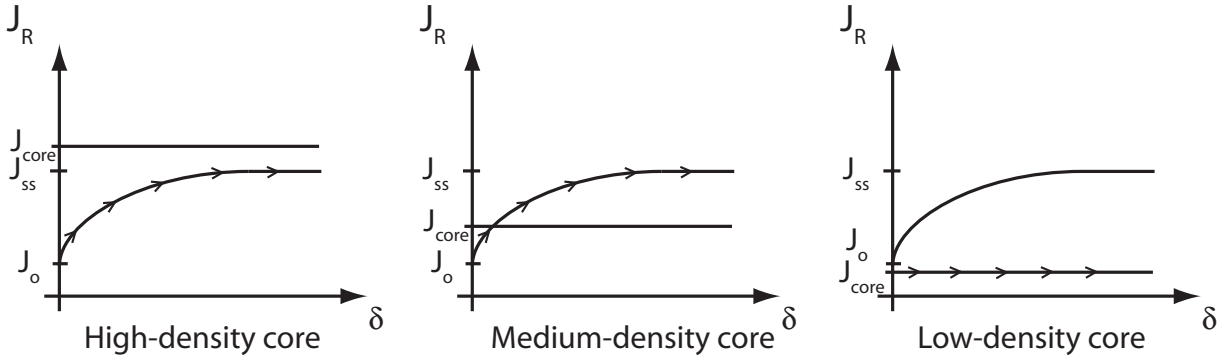

Figure 4.15: Schematic illustration of the fracture resistance as a function of pre-crack tip opening for high-, medium-, and low-density cores.

For the tested specimens with a woven mat in a mode II dominated loading, the crack did not penetrate the woven layer but instead a second crack developed on the opposite side of the woven mat which for some cases continued to kink into the quadraxial mat. It was found that the bonding between the woven layer and the quadraxial face was relatively poor, and it is believed that the mode-mixity transition point where the crack will start propagating across the woven layer is highly dependent on the bonding capabilities with the quadraxial layers. This correlates well with the fact that the transition point for jumping is higher for the coarser-woven mat (tex 300) than for the fine (tex 68), see Figure 4.14. It is believed that the woven tex 300 has better bonding capabilities than the tex 68 due to larger strands and a more rough surface. The larger strands entails gaps between the strands of the woven mat, which are filled with resin during production, and consequently cohesion between woven and quadraxial mats is improved. The transition point might be extended even further into mode II dominated mode-mixity e.g. by stitching the woven and quadraxial layers together before resin injection.

Considering Figure 4.14 a)-f) it is found that the results for specimens with the same lay-up are generally reproducible, both with regards to kinking behaviour and steady state fracture toughness. However, there is some disagreement between the fracture behaviour of specimens with and without a woven layer regarding crack kinking into the core, which is unexpected since the woven layer is not positioned next to the core and should not affect crack kinking into the core. With regards to the specimens with CSM in subplot a) and c) at a mode-mixity of $\varphi_o = 0.14$, the crack in the specimens with a woven tex 68 layer initially propagates in the core for 1-2 cm and then returns to the interface, whereas specimens without a woven layer do not kink into the core. The core material is two to three times tougher than the CSM layer, however as explained in Parmigiani and Thouless (2006) both J_o^{CSM}/J_o^{core} and $\sigma_o^{CSM}/\sigma_o^{core}$ affect the kinking behaviour. The tensile strength of the core material is given as 7.1 MPa in the manufacturer's data sheet, whereas the tensile strength of the pure resin is tested to be approximately 70 MPa. The pre-crack is defined by slip film exactly between the core and the CSM or CFM layer, and the crack initially favours to propagate into the relatively low-strength, yet tough, core while later the crack returns to the high-strength but brittle interface and stays here. The fact that the same does not happen to specimens without a woven layer indicates that the behaviour is sensitive to small variations, e.g. in production variables. Perhaps for some specimens a blob of resin is generated at the pre-crack tip which may influence the initial crack path. A more realistic pre-crack tip could be obtained by cracking the specimens before testing, which should be considered in future studies.

4.5 Summary

A modified sandwich Double Cantilever Beam loaded by Uneven Bending Moments (DCB-UBM) is used to explore the fracture behaviour of sandwich specimens with a face/core debond loaded under various mixed-mode conditions. The crack either propagates in the interface or kinks into the adjacent face or core and each regime is reached by varying the ratio between the applied moments. A finite element model with cohesive elements is used to determine the relation between moment ratio and a stress-based mode-mixity. Intermediate layers of mats with randomly oriented fibres are embedded in the interface to generate a weak layer, where the crack tends to propagate with the development of large-scale fibre bridging. It is found that fibre bridging develops mostly as the crack propagates near the centre of the CSM or CFM layer, which leads to a relatively high steady state fracture resistance (approx. 1.6 kJ/m^2 for the CSM and 2.4 kJ/m^2 for the CFM). Conversely, as the crack propagates in the outer region of the CSM or CFM layer, almost no fibre bridging appears and the steady state fracture resistance is significantly smaller (approx. 0.8 kJ/m^2). The mode-mixity transition where the crack kinks from the CSM or CFM layer and into the quadraxial part of the face laminate may be extended by inserting a thin woven layer between the quadraxial laminate and the CSM or CFM layer. In this case a fine-woven mat (tex 68) has an effect on the mode-mixity transition point for the CSM configuration but not for the CFM while for the coarser layer (tex 300) the transition point is extended for

both CSM and CFM. The crack never penetrates the woven layer but for high mode II cases a secondary crack is initiated and continues on the opposite side of the woven layer.

Chapter 5

Interface Cracking of Sandwich X-joints Loaded in Tension

5.1 Introduction

Part of the practical work described in this chapter was conducted by M.Sc. student Ulrik Rasmussen, who manufactured the specimens and collaborated with the author on conducting the experiments.

5.1.1 Background and Objectives

In many sandwich structures, e.g. sandwich naval ships, there is a need to assemble panels in out-of-plane joints, designated T-joints and X-joints, where one or two panels are attached perpendicularly to the faces of another panel which extends continuously through the joint. Loading of the attached panels entails out-of-plane forces acting on the faces of the continuous panel. In compression this can lead to indentation and crushing of the core, whereas tension can lead to debonding and face pull-off. Furthermore, crushing of the core can lead to debonded areas which can act as a starting crack causing debond propagation through parts of the structure, see Berggreen (2004). Thus, a joint that has been damaged in compression may fail under tension loads significantly smaller than those for an intact joint.

A literature search has revealed an appreciable amount of research into the behaviour of sandwich T-joints, see e.g. Dharmawan et al. (2004), Li et al. (2006a) and Toftegaard and Lystrup (2005). As regards X-joints, several recent studies were conducted, e.g. on the compression behaviour in Berggreen et al. (2007a) and on the tension behaviour in Lundsgaard-Larsen et al. (2007). The study described in this chapter is an extension of the work presented in Lundsgaard-Larsen et al. (2007).

Experiments are conducted on a sandwich beam that correspond to the through-going panel in a sandwich X-joint. To simplify the geometry of the specimens, no perpendicular panels are attached to the through-going panel, but the loading is instead applied directly to the sandwich faces, see Figure 5.1. It is thus assumed that fracture occurs inside the through-going panel due to a sufficiently strong connection between the perpendicular panels and the faces of the through-going panel. In the remaining part of this chapter the test illustrated in Figure 5.1 (b) is designated the Sandwich Tear Test (STT).

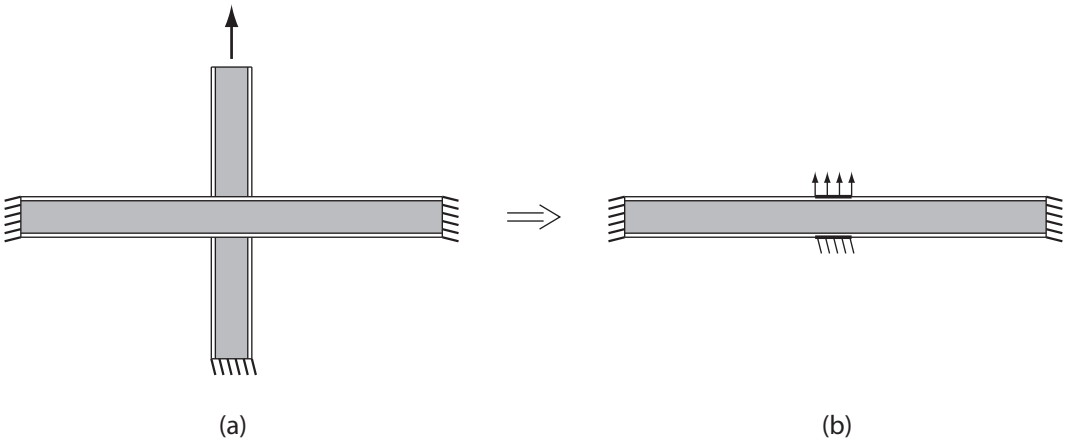

Figure 5.1: Simplified geometry and boundary conditions used to mimic an X-joint sandwich structure loaded in tension.

Berggreen et al. (2007b) conducted a similar study where numerical predictions based on LEFM were compared to experimental results for various core densities 80, 130 and 200 kg/m^2, i.e. H80, H130 and H200. Numerical and experimental results coincided well for the H80 case where the crack propagated in the core material just below the interface. For the H130 and H200 cases the crack kinked into the CSM layer between the face and the core and Large-Scale Bridging (LSB) developed behind the crack tip. As pointed out in Berggreen et al. (2007b), the assumption of LEFM is doubtful in the presence of LSB, and a significant disagreement between the experimental and numerical results was observed for specimens with H130 and H200 cores. In the present study specimens with H200 core are tested and the case is simulated using a Cohesive Zone Model (CZM) to represent tractions due to LSB in the process zone. A mat of randomly oriented fibres is inserted between the core and the quadraxial face during production. Two various intermediate layers are considered, Chopped Strand Mat (CSM) and Continuous Filament Mat (CFM), of which the CSM consists of 3-4 cm long fibre bundles in contrast to the CFM layer where the fibre bundles are very long. In addition, a thin woven layer is inserted between the CSM/CFM and the quadraxial face to delay the mode-mixity transition point where the crack will kink into the quadraxial face. The materials and the lay-up are identical to those of the study described in Chapters 3 and 4, thus the previously extracted cohesive laws are used as input for the finite element model in order to predict fracture in the STT specimens.

The objectives of this chapter are: (1) validate the proposed methodology of using a CZM to predict the fracture behaviour of a sandwich component and (2) investigate the effect

of the woven mat in the interface, regarding preventing crack kinking into the quadraxial face layers. (1) is pursued by by implementing the previously determined cohesive laws in a finite element model and subsequently compare numerical and experimental results. The crack kinking behaviour of the STT specimens is predicted by linking the kinking behaviour of the DCB-UBM tests to a mode-mixity measure, see Chapter 4. (2) is pursued by simply comparing the fracture behaviour of specimens with and without a woven mat in the interface.

5.2 Experimental Setup

The test rig used for the experiments is a slightly modified version of the one used in Berggreen et al. (2007b). It is constructed of welded steel tubes with rectangular cross sections and a wall thickness of 6 mm. The test rig constitutes a highly rigid structure compared to the sandwich beam and thus the compliance of the test rig may be neglected. The specimen is clamped at the ends where the core material is replaced by wood to enable a high contact pressure. Four bolts at each end are used of which, two are through-going and two are applying pressure to the sandwich skin. At the centre of the specimen steel plates are glued to the faces with epoxy adhesive, the top face is fixed to the crosshead, whereas the bottom face is connected to the test rig, see Figure 5.2. The specimen is loaded by moving the crosshead upward at a rate of 2 mm/min, and it is ensured that all rate effects are negligible and each specimen is loaded 30-40 mm before the crack is fully propagated. The lift force is provided by an Instron 8502 servo-hydraulic test machine.

The displacement field on the specimen surface is recorded using a Digital Image Correlation (DIC) system ARAMIS 4M, where points on part of the specimen surface are traced by the system software. A speckled pattern is applied to the specimen using spray paint and a thin layer of first white and then black paint is used to ensure a high contrast in the pattern. For the used loading speed (2 mm/min) a picture rate of one frame per four seconds is chosen as appropriate to be able to follow deformations continuously, without the need to process an unnecessarily large amount of data. The software can recognise points in the speckled pattern and is able to calculate the displacement field of the surface of the loaded specimen by comparison with the frame of the initial undeformed specimen. The force is measured by means of a 10 kN Instron load cell with a certified accuracy of 0.5 % of the capacity of the load cell.

A slip film is inserted between the face and the core along 480 mm of the specimen length, see Figure 5.3, so that the crack will only propagate to one side and only one fracture incidence will occur in the measurements. This entails that the specimen is not symmetric. The reason for not simply cutting off the pre-cracked part of the specimen and only test the intact half is that the tension in the face becomes very large during the experiment. This generates side forces on the crosshead, which might damage the test machine. The beam half with the slip film incorporated provides some symmetry and takes up part of the side force acting on the crosshead. The width of the specimen (z-direction in Figure 5.3) is 65 mm.

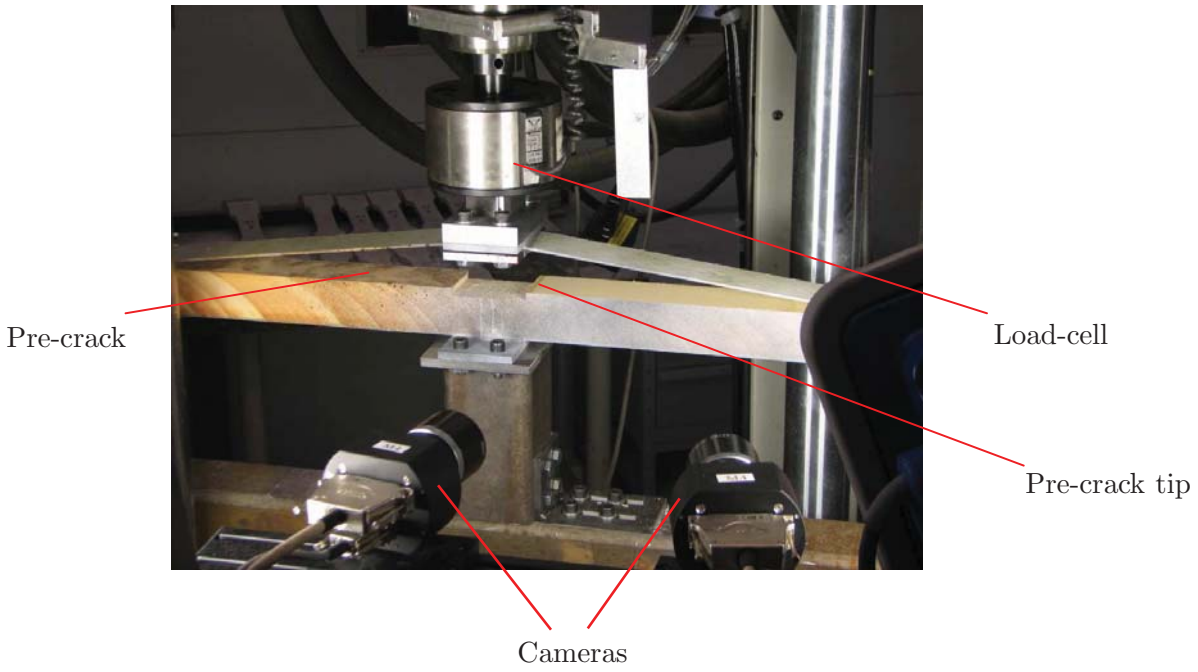

Figure 5.2: Loaded sandwich specimen in test-machine with crack running from the center to the right. Two cameras are used to record the displacement field in the right half of the specimen. Photo is from Jenstrup and Karlsen (2007), who conducted similar experiments using the same test-rig.

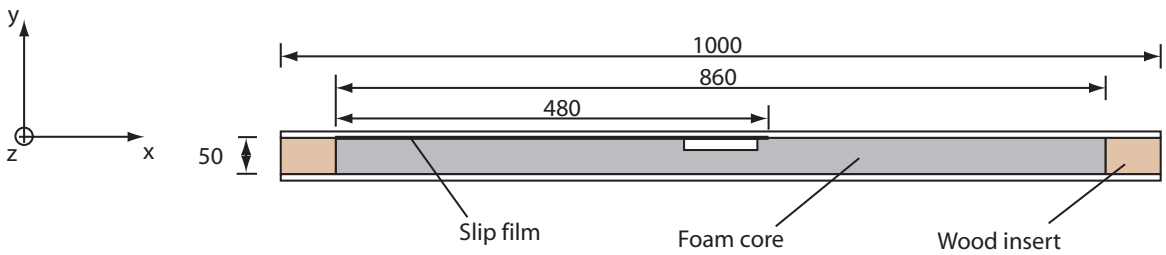

Figure 5.3: Schematic illustration of specimen with slip film and wood inserts at the ends (all dimensions are in mm).

The sandwich faces consist of four Devold Amt DBLT 850 quadraxial glass fibre mats, each with a dry area density of 850 g/m^2, and an additional layer with fibres oriented randomly (CSM or CFM) with area density of 450 g/m^2 placed between the quadraxial faces and the core. Furthermore, a plain-woven layer (tex 300) with area density 200 g/m^2 is inserted between the CSM/CFM mat and the DBLT during production, to act as a mechanical "wall" to prevent the crack from kinking into the face and damaging the load-carrying laminates. The effect of the woven layer was investigated in Chapter 4 by use of the DCB-UBM specimen with the same lay-ups as tested here. In this chapter the effect of the woven layer is examined by using the STT specimen and results are described in Section 5.4.2. A polyester resin Polylite® 413-575 is added by vacuum injection and the following panel configurations are manufactured:

1. $[90, 45, 0, -45]_4$ + woven tex 300 + **CSM** + core H200 + $[-45, 0, 45, 90]_4$

2. $[90, 45, 0, -45]_4$ + woven tex 300 + **CFM** + core H200 + $[-45, 0, 45, 90]_4$

3. $[90, 45, 0, -45]_4$ + **CSM** + core H200 + $[-45, 0, 45, 90]_4$

where configuration 3. is included to consider the effect of removing the woven layer from the interface, which will be described in Section 5.4.2. The pre-crack is defined with slip film between the CSM/CFM and the core and the total face thickness after production is approximately 3.0 mm for laminates with CSM and 3.5 mm for laminates with CFM. The sandwich core is Divinycell H200, 50 mm thick and with a density of 200 kg/m^3. The faces are assumed to be linear elastic and in-plane isotropic and the stiffness properties are measured in individual tests, see Jenstrup and Karlsen (2007) and Table 5.1. The H200 core material is assumed to be linear elastic and isotropic and the elastic properties are found in DIAB (2008) and listed in Table 5.1 as well.

Parameter	Designation
Face in-plane Young's modulus	14.1 GPa
Face out-of-plane Young's modulus	8.4 GPa
Face Poisson's ratio	0.33
Core Young's modulus	0.250 GPa
Core Poisson's ratio	0.29

Table 5.1: Elastic properties of face and core.

The following describes the finite element model used to predict the fracture behaviour of the sandwich specimens.

5.3 Numerical Model

5.3.1 General Assumptions

A 2-D plane strain finite element model is generated in the commercial finite element program ABAQUS version 6.6 and the Explicit solver is used. The model consists of two faces and a core, where part of the top face and core is connected through zero-thickness cohesive elements, which represent the traction-separation behaviour of the interface. Since part of the face is not initially bonded to the core the specimen is not symmetric, and no symmetry conditions are applied to the top face, see Figure 5.4. However, for the core and bottom face, symmetry conditions may be exploited in order to reduce the degrees of freedom and the computational time of the model. The symmetry assumption does not affect the solution noticeably, since it is applied far from the crack tip, see Figure 5.4. This assumption is tested by examining the strain distribution in the core, hereby ensuring that the strains near the edge where symmetry is applied are very small. The bottom face is fixed along a length of 40 mm since this zone is clamped to the rigid test rig in the experiments. The finite element model is meshed uniformly with four-node bilinear square elements each with eight degrees of freedom and the element side length is 0.5 mm, which corresponds to seven elements through the thickness direction of the face. The nodes of the continuum elements at the interface are coincident with the cohesive elements, which are also 0.5 mm in length. Convergence tests are conducted regarding the element size, by considering the resultant force-displacement curve for various meshes.

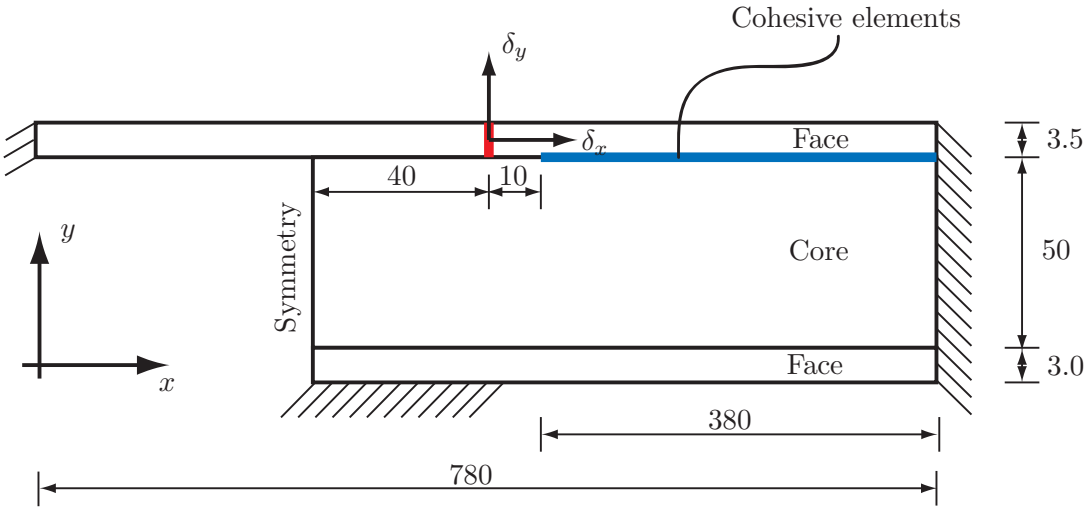

Figure 5.4: Illustration of geometry and boundary conditions of finite element model (dimensions in mm).

Since the specimen is not symmetric, side forces will appear and act on the load point. This entails a small horizontal displacement of the crosshead in the experiments, since the test machine is not completely rigid. The sideward displacement is measured by the DIC

system, and to generate boundary conditions for the finite element model that accurately represent the experimental conditions, this sideward displacement is included in the finite element model. The measured displacement in the horizontal direction δ_x is plotted as a function of vertical displacement δ_y in Figure 5.5, and it is found that δ_x reaches a maximum of approximately 0.5 mm at $\delta_y = 20$ mm. This horizontal displacement of the load point is included in the finite element model. The nodes along a line in the through-thickness direction of the face, marked with red in Figure 5.4, are tied together in a master/slave configuration, so that the slave nodes follow the master node. Rotation of the node set is prevented, and the specimen is loaded by applying a displacement to the master node according to Figure 5.5.

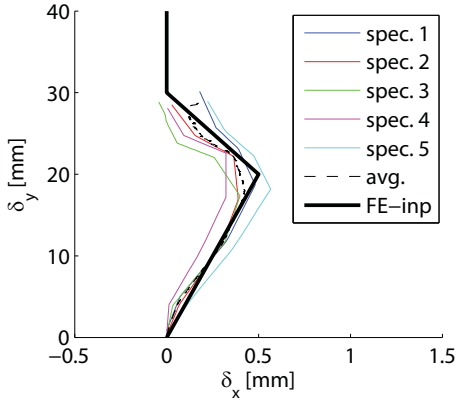

Figure 5.5: Vertical loading displacement δ_y vs. horizontal displacement δ_x, measured by the DIC system and applied as displacement controlled loading in the finite element model.

As described in Section 2.2, the finite element model is solved in the Explicit regime over a given time domain and inertia effects are included in the solution. Conflicting interests prevail since it is desired to reduce inertia effects as well as keep the simulation time (proportional to CPU time) as short as possible. Small modifications are made to the loading displacement curve illustrated in Figure 5.5 by rounding the sharp corners and hereby reducing the tendency for triggering inertia effects, such as natural vibration modes or stress waves in the specimen. Furthermore, in the simulation the total kinetic energy is always below 1% of the total elastic energy.

5.3.2 Implementing Cohesive Laws in the FE-Model

A traction-separation relation is to be defined for the interface in the finite element model according to the measured cohesive laws described in Sections 3.3.2 and 3.3.3. In Figures 3.19-3.21 the extracted mixed-mode cohesive laws for specimens with a CSM layer are presented. Regarding the traction-separation curves in the normal direction, the peak stress is between 5.1 and 5.7 MPa and the extracted cohesive laws consist approximately of two branches, of which the first represents separation near the crack tip with area below the

traction curve J_o and the second represents tractions due to LSB with area $J_{bridging}$. From the $J-\delta^*$ plot in Figure 3.15 the energy of the first branch is approximately $J_o = 0.4$ kJ/m^2, whereas $J_{bridging}$ depends on the amount of fibre bridging, which varies with mode-mixity.

The measured cohesive laws are noisy (see example in Figure 3.19) and a suitable idealization is sought in order to provide a simple, yet sufficiently detailed, input for the finite element model. The chosen idealised cohesive shape is illustrated schematically in Figure 5.6 and described by the parameters δ_o, δ_1, δ_c, σ_o, σ_1 and J_c, see Figure 5.6 (not all the mentioned variables are independent). Two parameters are chosen constant for all mode-mixities: $k = \sigma_o/\delta_o = 6 \cdot 10^{11}$ Pa/m and $\delta_c = 10$ mm. The slope of the initial linear branch $k = \sigma_o/\delta_o$ is chosen sufficiently high so that no significant compliance will be added to the intact part of the structure (found from a convergence test) and the stiffness corresponds to 120 times the stiffness of the core, E_c/h, where E_c is the core Young's modulus and h is the core thickness. The remaining parameters of each cohesive law are determined in the following order: 1) The maximum stress σ_o is found from the DCB-UBM test for individual mode-mixities, see e.g. Figure 3.23 for the CFM case, 2) the displacement variable δ_1 is chosen so that $J_o = 0.4$ kJ/m^2, and 3) σ_1 is chosen so that the total fracture energy of the cohesive law J_c matches the steady state J integral value from the DCB-UBM experiments. The obtained parameters for the tested mode-mixities are given in Table 5.2, and each cohesive law is transformed into a tabbing array of the damage variable $D(\delta_e, \varphi_\sigma)$, where δ_e is the effective displacement given by (2.12) and φ_σ is given by (4.3). For any intermediate mode-mixity between the ones described in Table 5.2, ABAQUS interpolates between them to estimate the damage variable D for the current δ_e and φ_σ value.

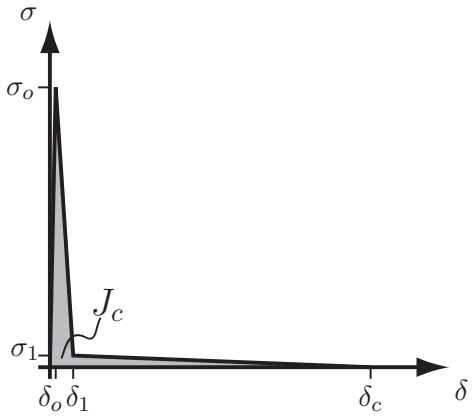

Figure 5.6: Shape of cohesive law used in simulations. Properties are listed in Table 5.2.

5.3.3 Mode-mixity and Crack Kinking

As explained in Section 4.4.1, the crack can propagate in various positions of the CSM or CFM layer, which entails different amounts of fibre bridging and consequently different fracture resistance values J_c. Thus, it is an objective to be able to link the crack kinking behaviour from the DCB-UBM specimens described in Chapter 4 to the STT fracture tests

Layer	M_1/M_2	φ_σ	J_c^{min} [kJ/m^2]	J_c^{max}[kJ/m^2]	σ_o [MPa]	σ_1 [MPa]	δ_1 [mm]
CSM + tex300	-0.4	0.047	1.1	1.4	5.6	0.169	0.134
CSM + tex300	-0.2	0.13	0.85	1.1	5.1	0.122	0.149
CSM + tex300	-0.12	0.19	0.76	0.83	5.3	0.080	0.137
CSM + tex300	0.2	0.39	0.76	0.84	5.7	0.135	0.135
CFM + tex300	-0.4	0.047	1.0	1.2	11.1	0.144	0.0711
CFM + tex300	-0.3	0.087	0.76	1.0	11.1	0.962	0.0711
CFM + tex300	-0.12	0.19	1.1	1.7	5.7	0.226	0.130
CFM + tex300	0.0	0.23	2.1	2.4	5.7	0.354	0.134

Table 5.2: Variables used to define traction-separation laws for specimens with CSM or CFM interfaces for various mode-mixities found from DCB-UBM experiments described in Sections 3.3.2 and 3.3.3. The parameters defining the cohesive law are illustrated in Figure 5.6 and the following parameters remain constant: $J_o = 0.4$ kJ/m^2, $k = \sigma_o/\delta_o = 6 \cdot 10^{11}$ and δ_c=10 mm.

described here. This is pursued by linking the observed fracture behaviour to a mode-mixity measure, which is described in the following.

Imagine a single cohesive element in the interface representing a finite element model of a sandwich structure: As the process zone passes the element, the mode-mixity varies during the loading history of the cohesive element, and the variation depends on the geometry and loading conditions of the considered specimen and of the prescribed cohesive law. ABAQUS utilises an average mode-mixity measure similar to φ_σ to relate the mixed-mode loading to the prescribed cohesive laws. The variation of mode-mixity inside the process zone is explored by using results from the finite element model at a crack length of 290 mm, see Figure 5.7. The mode-mixity in the process zone is intermediate close to the crack tip ($\varphi \simeq 0.48$), whereas it becomes increasingly mode I dominated toward the trailing edge ($\varphi \simeq 0.06$), see Figure 5.7.

The relation between φ_o and φ_σ as the crack propagates along the interface of the STT specimen is explored, see Figure 5.8, and the plot is generated in the following way: The mode-mixity at the crack tip φ_o is found from Eq. (4.2) by considering the cohesive element in the position of the leading edge of the process zone (where damage starts) during crack propagation. The mode-mixity at the crack tip as the crack propagates is then recorded and plotted as function of crack tip position. Additionally φ_σ is found as the average mode-mixity history of each individual cohesive element along the interface after complete damage, by using Eq. (4.3). For the considered loading case it is found that the ratio between φ_o and φ_σ is approximately constant with a value close to 4.

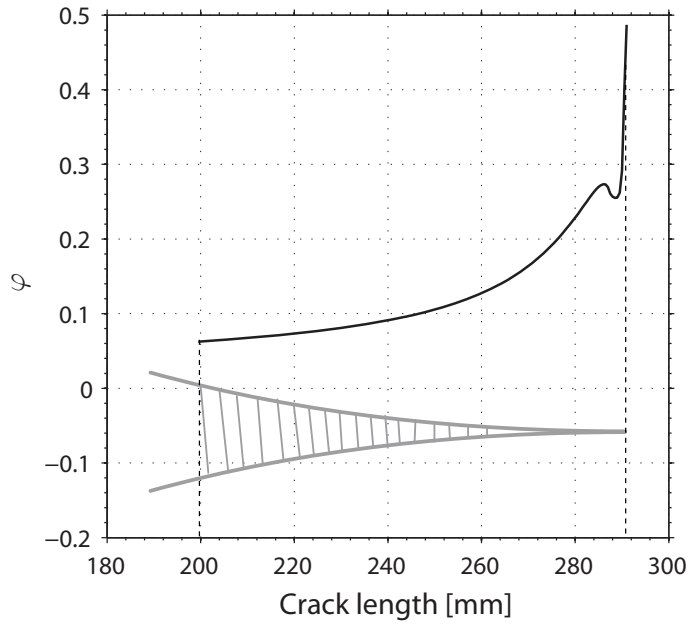

Figure 5.7: Mode-mixity calculated from stresses in cohesive elements inside process zone at fixed time. The crack length refers to the distance from the pre-crack tip.

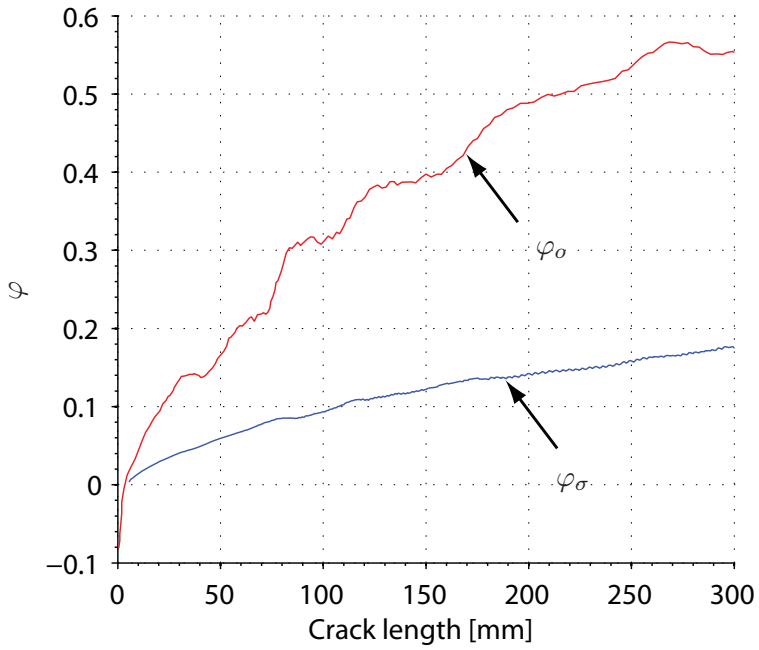

Figure 5.8: Crack tip and average mode-mixity in various positions along the interface.

5.4 Experimental Results

In this section experimental results from the STT tests are described and compared with the results from the finite element model. First, the crack kinking behaviour is considered for specimens with a woven layer incorporated in the interface, subsequently the behaviour of specimens without a woven layer is explored and finally results for load and crack length as a function of crosshead displacement are presented and compared with the numerical results.

5.4.1 Interlaminar Crack Path

When considering the crack kinking behaviour of specimens with a woven layer and either a CSM or a CFM layer incorporated in the face sheet, there is a clear difference between them. For the first type the crack initially kinks into the CSM layer and propagates here 150-200 mm with fibre bridging developing behind the crack tip. The crack subsequently changes path from the CSM layer and into the resin between the CSM and the woven layer and propagates here for the remaining part of the test without noticeable fibre bridging. A representative cracked specimen with CSM layer is seen in Figure 5.9, while a cracked CFM specimen is shown in Figure 5.10. For specimens with a CFM layer, the crack initially kinks into the core and continues to propagate here 20-70 mm. Subsequently, the crack changes path to the CFM layer for approximately 100 mm and finally kinks into the resin between the CFM and the woven layer for the remaining part of the test.

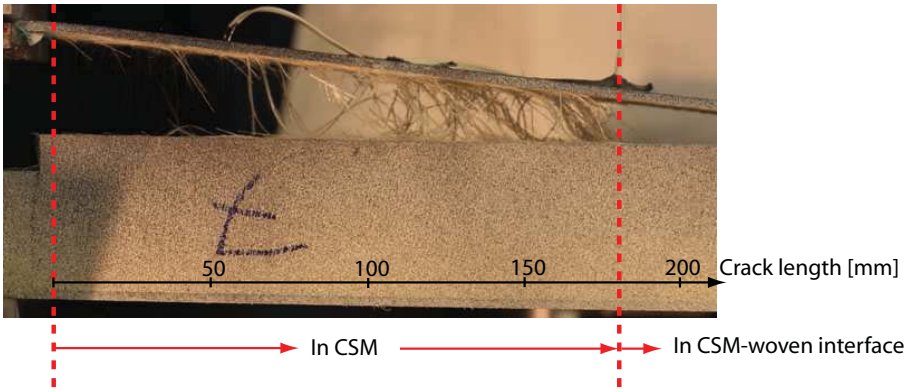

Figure 5.9: Cracked specimen with CSM in the interface. The left vertical red line indicates the position of the pre-crack tip, and the right the transition point where the crack kinks into the resin layer between the CSM and the woven mat. Between the two vertical red lines the crack propagates in the CSM layer with visible large-scale fibre bridging.

Regarding the STT tests each material combination (CSM and CFM) is repeated five times and repetitions show the same qualitative crack path behaviour. However, the crack lengths where the crack kinks are associated with some scatter and the variation is up to 50 mm between the conducted tests.

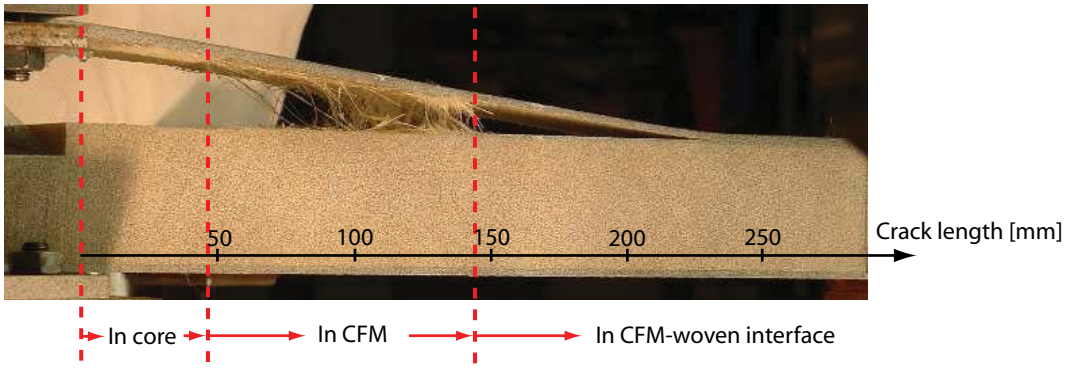

Figure 5.10: Cracked specimen with a CFM layer at the face/core interface. The vertical lines show where the crack propagates: 1) In the core, 2) in the CFM layer and 3) in the resin between CFM and woven mat.

5.4.2 Effect of Woven Layer on Crack Kinking

In this section results are presented for specimens with a CSM layer in the interface but without any woven layer. The purpose is to compare the crack kinking behaviour with previously described results and hereby examine the effect of the woven layer. In Chapter 4 it was shown by use of the DCB-UBM specimen, that the woven mat extends the mode-mixity transition point where crack deflects into the quadraxial face layers. In this section the effect of the woven layer is examined by the STT specimen. The results described in this section are from a Master's Thesis project, see Jenstrup and Karlsen (2007), that was conducted with the author as co-supervisor. The experiments were carried out approximately 1 year earlier than the other tests described in this chapter, however, the materials, the geometry and the test method used for the specimens are identical, thus a comparison between the two test series is believed to be valid.

Consider the the fully cracked STT specimen without any woven layer in Figure 5.11. Large scale bridging is developing in the crack wake, and at a crack length of approximately 180 mm, the crack kinks into the quadraxial layers and continues to gradually kink through the layers. This is observed by considering the top face layer still attached to the core, which increases in thickness towards the end of the specimen. The same occurs for all five tested specimens, and it is interpreted that the woven layer (not incorporated in this specimen) prevents crack kinking into the quadraxial face layers. This is further discussed later in this chapter.

5.4.3 Reaction Force and Crack Length

This section compares numerical and experimental results regarding reaction force and crack length, both as a function of crosshead displacement, for specimens with a woven mat and either a CSM or CFM layer incorporated at the interface. If the fracture behaviour is

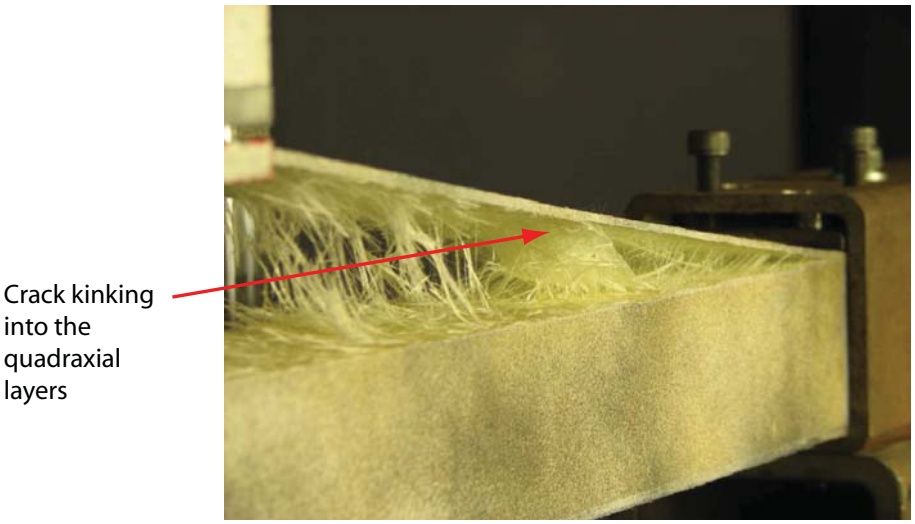

Figure 5.11: Specimen with a CSM layer in the interface without any woven layer from Jenstrup and Karlsen (2007). Crack kinking into the quadraxial layers occurs after at a crack length of approximately 180 mm.

correctly measured from the DCB-UBM tests and suitably implemented in the finite element model of the STT, the experimental and numerical results should match. The crack length at a given point in time is defined as the distance from the pre-crack tip to the current crack tip position, i.e. the leading edge of the process zone. In the experiments the crack tip position is manually identified from the DIC measurements, and the crack length is subsequently measured with the aid of the DIC software. Force and crack length, both as a function of crosshead displacement, are illustrated for the CSM specimens in Figure 5.12. The experiments are represented by thin coloured lines, while numerical results are illustrated by thick black lines representing both the upper and lower bound of J_c from the DCB-UBM experiments, see input in Table 5.2.

Regarding the load-displacement relations for specimens with *CSM*, shown in Figure 5.12 a), the load initially increases steeply until reaching a peak where the crack starts propagating followed by a load drop to approximately 60 % of the peak value. As the crack continues to propagate the loading case becomes increasingly mode II dominated and the reaction force increases. Generally, the reaction force predicted from the finite element model is larger than the experimentally measured reaction force. The initial peak load in the simulation is 1.05 kN, which is within the experimental range of 0.6-1.1 kN. However, at a crosshead displacement of 10 mm the predicted load is about 50 % higher than the experimental results and finally towards the end (crosshead displacement above 20 mm) a fair agreement is again achieved. As regards the crack length vs. lift displacement in Figure 5.12 b), results agree reasonably well within the first 20 mm of lift displacement. Towards the end the experimentally found crack length becomes approximately 20 % shorter than the numerical one for the same crosshead displacement value. Results are further discussed in Section 5.5.

Regarding results for specimens with *CFM*, see Figure 5.13, initially consider the force vs.

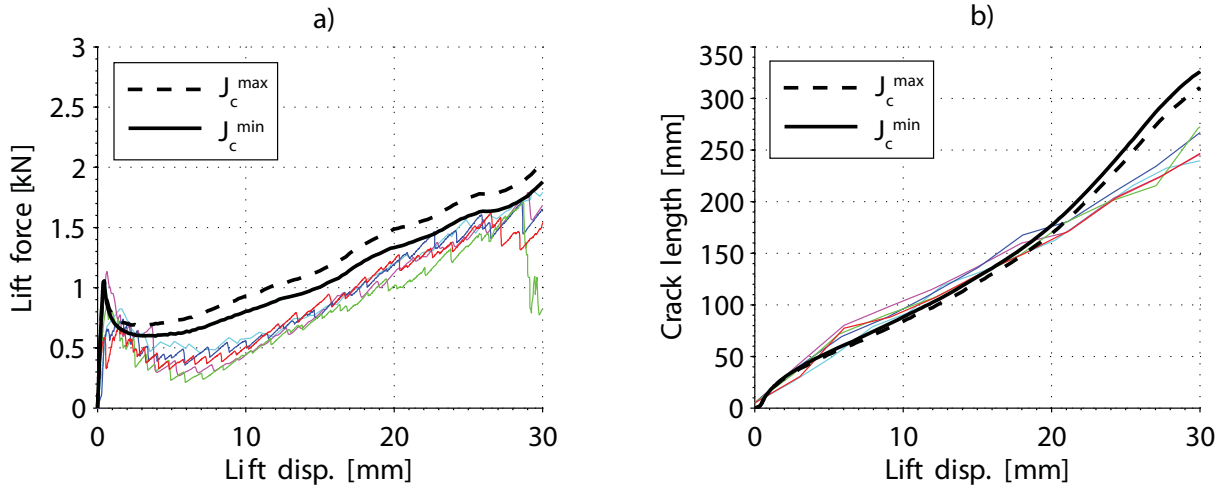

Figure 5.12: Comparison between experimental and numerical results for specimens with CSM and woven tex 300. Experiments are represented by thin coloured lines and finite element results are thick black lines. The solid black line is the lower bound regarding measured J_c whereas the dashed line represents the upper bound.

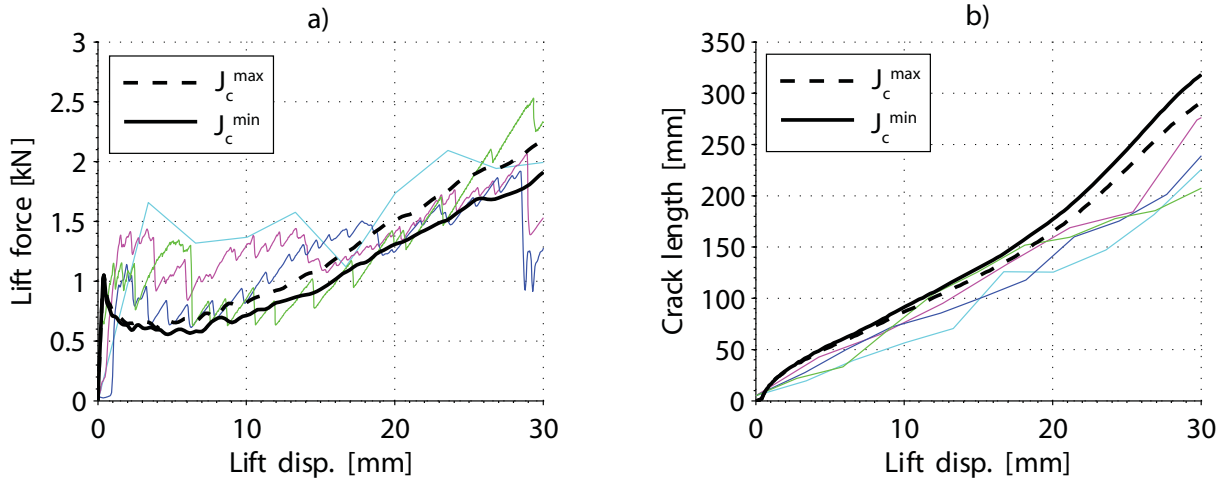

Figure 5.13: Comparison between experimental and numerical results for specimens with CFM and woven tex 300. Only four out of five experimental results are included due to an error in the load signal in one of the tests

displacement in subplot a): The fracture behaviour of the specimens is distinctly different from the CSM case. Within a few mm of crosshead displacement the load increases to within a range of 1 to 1.5 kN (compared to 0.6-1.1 kN for the CSM). This behaviour may be related to initial crack kinking into the core material, which is tougher than the interface. The reaction force is generally connected with a high degree of scatter between the four presented experiments, however the load level is clearly higher compared to the CSM case. In contrast to the CSM case, the numerical results underestimate the lift force necessary to drive the crack in the CFM specimens, and possible causes for this behaviour are discussed in Section 5.5. As for the crack length vs. displacement in subplot b), results generally agree fairly, however deviations increases towards the end (displacements above 20 mm).

5.4.4 Parametric Study

To understand how the parameters of the cohesive law affect the numerical results a sensitivity study is conducted. The following cases are tested:

1. The peak stress σ_o is changed $\pm$ 50 % while keeping J_o and J_c constant.
2. The area below the curve of the first branch of the cohesive law J_o is altered $\pm$ 20 % while keeping σ_o and J_c constant.
3. The total fracture energy J_c is changed $\pm$ 20 % overall, so that both J_o and $J_{bridging}$ are changed 20 % while σ_o remains constant.

Case 1: For the cohesive laws used in this study the critical stress varies between 5.1 and 11.1 MPa, which is measured from the DCB-UBM experiments, see Figure 3.23. However, the measured critical stress may be connected with some uncertainty due to tedious displacement measurements as discussed in Section 3.3.5. It is of interest to examine the sensitivity of the critical stress on the found load-displacement curves. The cohesive law is altered so the critical stress σ_o is changed without modifying any of the areas of the two branches J_o and $J_{bridging}$, see schematic insert in Figure 5.14.

It is found that the peak load (just before the crack starts propagating) is affected 8-9 % as the critical stress is changed 50 %, however, the remaining part of the load-displacement curve is unaffected. This behaviour is discussed further in Section 5.5.

Case 2: As described in Section 5.3.2 the area of the first branch J_o is assumed to be 0.4 kJ/m^2, which is found to be reasonable by considering the $J - \delta^*$ curves, see e.g. Figure 3.15, where J_o is generally in the range of 0.3-0.5 kJ/m^2. It is of interest to examine the sensitivity of J_o on the load-displacement curve of the STT specimen to investigate whether the assumption of $J_o = 0.4$ kJ/m^2 is sufficiently detailed. The cohesive law is altered so that J_o is modified $\pm$20% without changing any of the remaining parameters σ_o and J_c (consequently $J_{bridging}$ is varied $\mp$20 % since $J_c = J_o + J_{bridging}$), see insert in Figure 5.15.

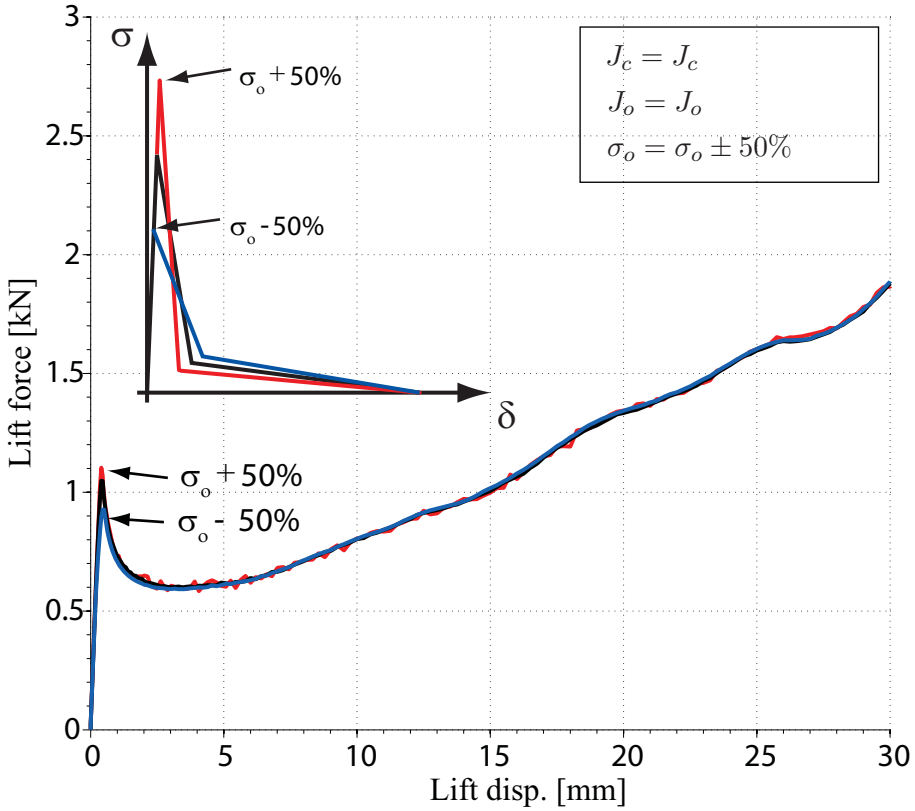

Figure 5.14: Sensitivity study based on changing the critical stress $\sigma_o \pm 50\%$ while keeping J_o and J_c fixed.

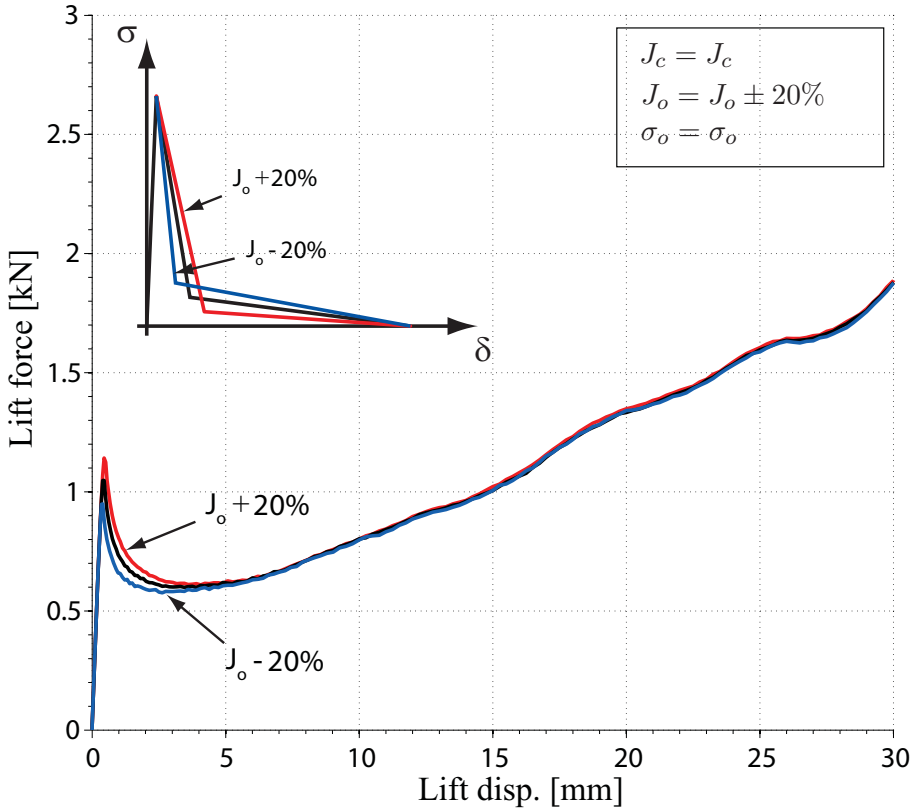

Figure 5.15: The influence of changing the crack tip toughness J_o while keeping J_c fixed on the load-displacement curves.

The load-displacement curves are plotted in Figure 5.15: The deviation in lift force is largest at the peak, where the 20 % change in J_o causes a 10-11 % change in the peak force. From this point the curves approach each other and at a lift displacement of approximately 6 mm (crack length 60 mm) the difference is negligible for the remaining part of the test.

Case 3: Finally, the overall fracture energy J_c is varied in order to investigate the sensitivity on the load-displacement curves. Both branches are modified with the same percentage, so that $J_o = J_o \pm 20\%$ and $J_{bridging} = J_{bridging} \pm 20\%$, see insert in Figure 5.16.

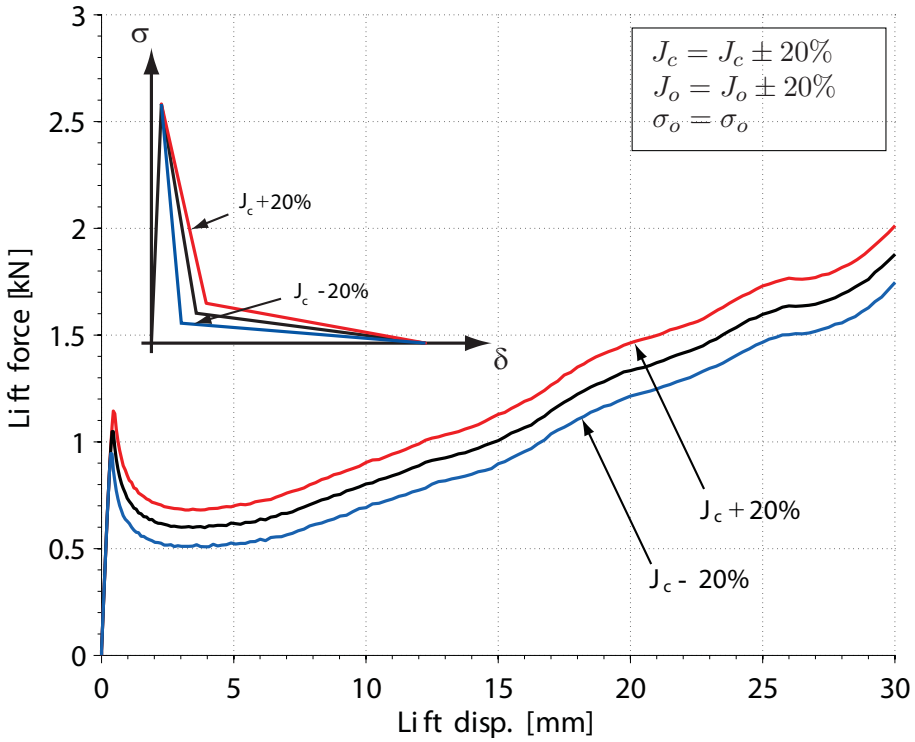

Figure 5.16: Parameter study of the influence of the critical energy J_c on the load-displacement curve.

It is found by considering the results in Figure 5.16 that the curves are approximately translated 0.1 kN in the vertical direction as J_c is altered 20 %, thus both the peak load and the load at large crack lengths are affected. The results from the parametric study are discussed in Section 5.5.

5.4.5 Development of the Process Zone

By using the finite element model a small analysis of the process zone development is conducted to comment more on the influence of the cohesive law on the fracture behaviour. The positions of the leading and trailing edges of the process zone as function of load-point displacement is plotted in Figure 5.17 a). The position of the leading edge (where damage

initiates) is represented by a black line and the trailing edge (where tractions vanish) by a red line. Furthermore, the process zone length given as the vertical distance between curves is plotted in subplot b). For the first 0.05 mm of displacement the crack tip has not propagated yet and the crack length equals the pre-crack length of 10 mm. Due to the short crack length the load is sensitive to the critical stress σ_o and the shape of the cohesive law (varying J_o), as shown in Figures 5.14 and 5.15. Subsequently, the crack tip departs from the pre-crack tip and the crack length increases. At a load point displacement of 8 mm the process zone is fully developed and the steady state process zone size is approximately 70 mm, see subplot b). The process zone is indeed not small compared to various specimen dimensions (e.g. crack length and face thickness), thus it may seem surprising that the load-displacement curve is relatively unsensitive to σ_o and J_o. However, the cohesive law consists of a two-branch shape where stresses are very small along the major part of the process zone, so the case is not as sensitive to the critical stress σ_o as the size of the process zone might imply.

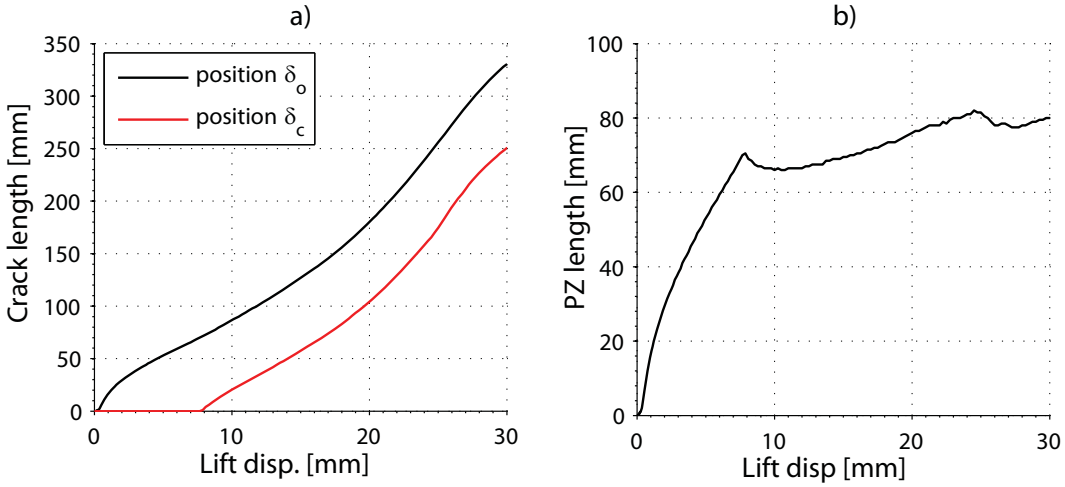

Figure 5.17: a) Position of leading and trailing edge of the process zone, and b) process zone size, i.e. vertical distance between black and red curves in subplot a).

5.5 Discussion and Perspectives

Consider the load vs. displacement plot for the CSM configuration in Figure 5.12 a): In the displacement range of 5-20 mm, numerical and experimental results disagree, and the predicted load is about 50 % larger than the experimental one. Conversely, for small and large load-point displacements the predicted and experimental results show fair agreement. To identify possible sources of error a sensitivity study of the parameters defining the implemented cohesive laws is conducted, see Figures 5.14-5.16. Variations in peak stress σ_o and the shape of the cohesive law (varying J_o and $J_{bridging}$) only affect the load-displacement curve in the vicinity of the peak load, i.e. in the load point displacement interval 0 to 6

mm. For this interval deviations in the reaction force are small. It is therefore not plausible that inaccuracies in σ_o and J_o cause the disagreement in the load point displacement interval of 5 to 20 mm. The overall load-displacement curve is mostly affected by J_c and probably deviations are related to this parameter, which is described further in the following.

For the CFM configuration, see Figure 5.13 a), a large scatter is observed between the four tested specimens, and some of the results agree fairly with the predicted, whereas others do not. The scatter is significantly larger than what is predicted by considering the upper and lower bound from the DCB-UBM experiments. The large deviations at load-point displacements below approximately 5 mm may be explained by the fact that the crack initially propagates between 20 and 70 mm in the core which is not taken into account in the finite element model. The fracture toughness of the core is previously measured to be around 2.5 kJ/m^2, which is 2-3 times higher than J_c for the interface and this might lead to an underestimation of the reaction force at load-point displacements below 5 mm.

For the cases considered in this study it is believed that φ_o is more suitable than the global mode-mixity measure φ_σ, since kinking is governed by the stress state in front of the crack tip, as discussed in Chapter 4. Presently, the mode-mixity measures for the cohesive elements in ABAQUS depend on the complete loading history of the element rather than only the load situation at damage initiation, i.e. mode-mixity at the crack tip. The influence of the mode-mixity measure on the crack kinking behaviour and consequent fracture resistance is not studied further here but a systematic investigation of the subject is needed and should be explored in the future.

The proposal of implementing a woven layer to prevent crack kinking into the load carrying face layers, is an essential part of this thesis. It is shown in Section 4.4.2 by means of the DCB-UBM specimen, that the mode-mixity transition point where the crack kinks into the quadraxial face layers is extended by the woven layer. The concept is furthermore tested in the STT specimens by comparing the crack path of specimens with and without a woven layer. Results show that for the case without a woven layer the crack kinks into the quadraxial face at a crack length between 180 and 250 mm (as the load becomes sufficiently mode II). Conversely, for the STT specimens with a woven layer, the crack does not kink into the quadraxial layers and instead the crack propagates in the resin between the woven and the CSM/CFM layers. Thus, for the STT specimen, the woven layer succeeded in preventing crack kinking into the quadraxial face layers.

The specimen width (z-direction in Figure 5.3) could cause some deviations, since an analysis conducted by the DCB-UBM specimens showed that in the case of LSB the fracture resistance per unit width increases with increasing width, see Section 3.3.4. The DCB-UBM specimens used for extracting cohesive laws are 30 mm wide, whereas the STT specimens are 65 mm, which could lead to an underestimation of the reaction force for the STT specimen, as occurs for the CFM configuration, see Figure 5.13. This does, however, not explain why the reaction force is overestimated in the CSM configuration.

It is observed that for the present face/core interface configuration the CFM layer is significantly more damage resistant than the CSM layer, found by comparing Figure 5.12 and 5.13.

The fibre bundles in the CFM layer are longer and more difficult pull out of mat, thus the fibre strands transfer larger tractions and sustain the tractions over longer crack openings than the CSM strands.

5.6 Summary

The procedure of predicting the fracture behaviour of debonded sandwich structures by incorporating a measured traction-separation law in a cohesive zone model is studied. Experiments are conducted where the glass fibre/polyester face of a sandwich beam is separated from a foam core by pulling the face in the perpendicular direction of the face surface. A mat of randomly oriented fibres (CSM or CFM) is incorporated between the face and core, acting as a weak layer where the crack will tend to propagate while developing large-scale fibre bridging that increases the fracture resistance. Furthermore, a thin woven layer is incorporated between the CSM/CFM and quadraxial layers to prevent crack kinking into the quadraxial face layers. By comparing the crack propagation path for specimens with and without a woven layer it is found that the woven layer succeeded in preventing crack kinking into the quadraxial layers. The load-displacement relation is predicted using the cohesive zone model and the predicted and experimental results agree within deviations of approximately 50 %. From a parametric study it is found that deviations are likely to be related to the measured steady state fracture resistance J_c, i.e. area below the curve of the cohesive law rather than the detailed shape, which the load-displacement curve of the STT specimen is not specifically sensitive to. A possible source of error could be the mode-mixity measure in ABAQUS, which averages over the loading history of the cohesive element. The mode-mixity measure should depend on the attributes that govern crack kinking, and it is believed that a local mode-mixity measure at the crack tip is more appropriate than the present measure in ABAQUS.

This page is intentionally left blank.

Chapter 6

Dynamic Fracture of Composite ENF Specimens

6.1 Introduction

The work presented in this chapter is part of an international research project that comprises several participants including Dr. Brian Cox[1], Associate Professor Roberta Massabò[2] and Professor Weinong Chen[3]. The project involves experimental and numerical investigations, and the overall goal is to deduce high-rate cohesive laws from through-thickness reinforced composites by varying the cohesive law in a numerical model until experimental and numerical results coincide. The work presented here is a contribution to the project and an initial step towards designing test specimens for extracting high-rate cohesive laws. The work was conducted in collaboration with Dr. Brian Cox and Associate Professor Roberta Massabò as a part of the PhD study during stays of five months at Teledyne Scientific and two months at University of Genova.

6.1.1 Background

Crack propagation may be either quasi-static or dynamic. In a quasi-static crack growth scenario the crack is in equilibrium with the external applied loads, so that the energy used to generate new crack surfaces and plastic deformation as the crack propagates is directly supplied by the external forces. Even when cohesive fracture properties are rate dependent, quasi-static crack growth can occur. If, however, the elastic energy in the specimen exceeds the energy necessary to propagate the crack, this may lead to unstable crack growth in which

[1]Teledyne Scientific, Thousand Oaks, California, USA
[2]University of Genova, Genova, Italy
[3]Purdue University, West Lafayette, Indiana, USA

case the stored elastic energy is used to propagating the crack unstably, with excess energy transferred into dynamic effects such as vibrations or stress waves. Thus, a dynamic crack growth event may take place without any simultaneous increase in external loading.

Several experimental studies indicate that fracture of composite materials is rate dependent, see e.g. Cantwell and Blyton (1999) for a review. In Ravi-Chandar and Balzano (1988), Kinloch and Williams (1980) and in Section 3.3.5 of this thesis, it is described how the crack propagates in a "stick-slip" mode, which indicates that the critical energy release rate decreases with rate. Sun et al. (2008) characterises a "crack-initiation toughness" that may be different from the "crack-arrest toughness". An example of this is if the plastic deformation ahead of the crack tip leads to blunting of the crack tip, which increases the energy necessary to initiate crack propagation. Conversely, as the crack starts propagating, the crack tip suddenly becomes sharp, and the critical energy release rate is reduced which increases the tendency for unstable crack growth. Dimensioning of composite structures based on quasi-static fracture toughness may therefore be unconservative in the case of unstable crack growth or high propagation rates in dynamic fracture, and there is a desire to develop methods for simulating dynamic fracture coupled with adequate rate dependent fracture properties measured in dynamic experiments.

Laminates with Through-Thickness Reinforcements (TTR), e.g. z-pins or stitching, generally improve the damage tolerance of composite materials since TTR involves fibres being pulled out of a matrix material, which increases the energy release rate. Delamination of composite with TTR normally involves a large process zone, in which case LEFM is not suitable and instead cohesive zones may be used. Only very limited experimental work has been carried out to determine the fracture rate dependence of laminates with TTR. In Liu et al. (2007) experiments were conducted by pulling fibres out of a substrate at rates of 1 mm/min and 100 mm/min, and the results show that friction increases with speed. A possible physical explanation given by the authors is the visco-elastic behaviour of the fibre/matrix interface e.g. coupled with a temperature increase due to friction. Several numerical studies using micromechanical models have been made in order to investigate rate effects on fibre pull-out of a laminate, see e.g. Cox et al. (2001), Sridhar et al. (2003) and Cox (2005).

As described in Section 2.1.1, various approaches to extract cohesive laws from fracture tests under static conditions have been proposed. When dynamic effects are present it is not valid to use theory derived for static conditions relating the far-field applied loading to the fracture processes. Instead, local measurements of the crack tip opening is often more suitable for determining dynamic fracture properties, see Sharpe and Böhme (1994). In Cox and Marshall (1991) a method is presented for deducing cohesive laws from experimental measurements of the crack opening profile near the process zone. In Massabò et al. (1998) cohesive laws are extracted from stitched laminates by varying the cohesive law until numerical and experimental results coincide for an ENF specimen loaded in three-point bending, and both the displacement profile in the process zone and reaction forces are used independently to deduct the cohesive law. The overall research project (of which this study is a part) should eventually become an extension of the methods presented in Cox and Marshall (1991) and Massabò et al. (1998) into the dynamic regime.

It is desired to measure the cohesive laws in a range going from static to impact loading, but as the loading rate is increased the interpretation of the results becomes increasingly problematic. In Böhme and Kalthoff (1982) a composite ENF specimen was loaded in three-point bending with a drop-weight impact. The experiment was heavily instrumented in order to simultaneously measure the impact load, reaction force at supports, specimen displacement relative to supports and stress intensity factor at the crack tip by an optical method. Results showed that the load synchronised neither with the support reaction forces nor the crack tip stress intensity factor. Furthermore, shortly after impact the specimen lost contact with the supports and large variations in the stress intensity factor at the crack tip were observed.

In a dynamic fracture test an important challenge is to find an optimal loading speed and ramp time. The ramp time should be sufficiently short to obtain the desired crack tip speed before the crack reaches the end of the specimen, yet large enough for the load point acceleration to be moderate and thus avoiding heavy oscillations and stress waves sweeping back and forth inside the specimen influencing the stress state at the crack tip. It is desired to create conditions where the crack propagates at an almost constant rate. If the crack speed is varied (uncontrollably) during the test, it will be difficult to associate the measured cohesive law with a certain rate.

6.1.2 Objectives and Scope

It is an aim to investigate the fracture behaviour of composite ENF specimens with z-pins during high-rate loading. In particular, it is interesting to investigate the sensitivity of the cohesive law as regards the experimentally measurable output, which is considered by analysing the change in response as the cohesive law is modified. If the fracture behaviour is sensitive to the cohesive law, the experiment is information rich, and it is plausible that the cohesive law can be extracted from the experiments by seeking interference between experimental and numerical results. It is furthermore relevant to conduct a stress analysis of the specimen, in order to ensure that the specimen will not break unintendedly.

Only the mode II ENF specimen is considered in this study, even though mode I and mixed-mode fracture are of equal interest. One advantage of the ENF specimen is that for high loading rates the damage energy dissipation is close to pure mode II, with only negligible mode I energy. In contrast, the fracture energy of the mode I DCB specimen (fixed at one arm and loaded at the other, see Figure 2.3) becomes mixed-mode when loaded at high rates, since the specimen will deform in an un-symmetric way, due to inertia effects. Mixed-mode fracture entails a choice as regards the mode I and II coupling formulation, which is unknown for the considered materials, however, it still has a significant influence on the calculated fracture behaviour. However, since the ENF specimen is chosen, (almost) pure mode II conditions prevail and the mixed-mode coupling used in the simulation does not affect the results.

6.2 Definition of the Problem

6.2.1 Specimen Geometry and Material Properties

This study considers an ENF specimen loaded in three-point bending, see Figure 6.1.

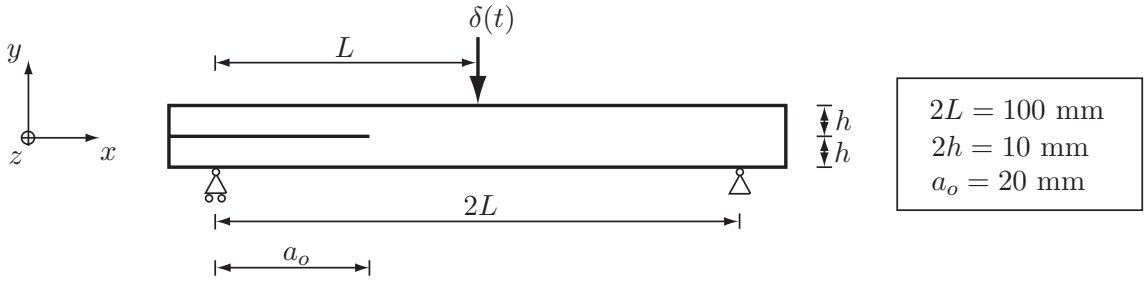

Figure 6.1: Dimensions of centre-loaded ENF specimen.

The material is assumed to be linear elastic with material properties typical of carbon fibre reinforced epoxy. The aim of this purely numerical study is to investigate the behaviour of the specimen when loaded in the dynamic regime, and it is believed that small variations in the elastic properties of the composite are not of great importance and will not change the conclusions drawn. The assumed laminate lay-up is quadraxial $(90, \pm 45, 0)$ (in-plane quasi-isotropic) with effective properties as listed in Table 6.1.

E_x, E_z	50 GPa
E_y	10 GPa
$\nu_{xy}, \nu_{xz}, \nu_{yz}$	0.28
G_{xy}, G_{yz}	5 GPa
G_{xz}	$E_x/(2(1+\nu_{xy}))$
ρ	1600 kg/m^3
σ_u (tension)	750 MPa
σ_u (compres)	630 MPa

Table 6.1: Material properties for quadraxial $(90, \pm 45, 0)$ carbon/epoxy laminate related to coordinate system in Figure 6.1. The ultimate stresses σ_u in tension and compression are obtained from experiments presented in Soden et al. (2002).

The choice of specimen dimensions such as length, thickness and pre-crack length is made on the basis of the following considerations:

The **specimen length** should be several times the process zone length in order to enable full development of the process zone and steady state propagation during the test. Conversely, if the specimen becomes very long this will lead to awkwardly large deflections. Simulations show that if the loading displacement is applied at a high acceleration at the midpoint of a very long slender specimen, the material close to the load point will move much faster

than the material distant from the load point, which is retained by inertia. This leads to a deflection shape remarkably different from the quasi-static case, and this non-equilibrium state will eventually lead to oscillatory behaviour of the specimen. This effect is increased with specimen length, which is the reason for choosing a relatively short specimen of a length (between supports) of $2L = 100$ mm. Some additional effects of choosing a longer specimen are considered in Section 6.3.3.

The **specimen thickness** is found from stress analysis performed by application of the finite element model. A thicker arm reduces the maximum stresses, but also increases the size of the process zone, which should be a fraction of the specimen length. For the chosen thickness of $2h = 10$ mm the maximum stress in the longitudinal direction of the beams is approximately 410 MPa in tension and 360 MPa in compression (maximum stresses in compression and tension are different due to the influence of the process zone). According to Table 6.1, the strength of the laminate is 750 MPa in tension and 630 MPa in compression. Thus, the specimen should be able to withstand the applied loading without failing unintendedly.

The **pre-crack length** should be long enough to avoid unstable crack growth, yet short enough for the process zone to develop and reach a certain speed before the crack tip reaches the end of the specimen. For an ENF specimen on the assumption of LEFM the transition between stable and unstable crack growth occurs at a pre-crack length of $a = 0.7L$, see Carlsson et al. (1986). However, for large-scale bridging cases, stable crack growth can be obtained with much shorter pre-cracks depending on the shape of the cohesive law (this will be shown later). Based on numerical analysis the notch length is chosen to be 20 mm, i.e. $0.4L$.

The simulations described in this chapter are 2-D, thus the specimen width (specimen dimension in z-direction in Figure 6.1) will affect results proportionally and a unit width (1 m) is chosen for specimen in the simulations. In a physical test the width of the specimen would typically be 20-30 mm chosen in accordance with the distance between z-pins or stitches, so that the specimen averages over at least 5-10 z-pins or stitches in the width direction.

6.2.2 Finite Element Model

The 2-D finite element model consists of two beams connected through zero thickness cohesive elements that partly cover the beam length, see Figure 6.2. The pre-crack constitutes the part of the beam without cohesive elements. A frictionless contact interaction is formulated in a penalty master-slave configuration between the two beams to prevent interpenetration. The mesh is mainly uniform with a refinement near the interface, see similar mesh in Figure 2.12, with a ratio of four between the side length of the smallest and largest element. Nodes between bulk and cohesive elements are coincident and the side length of the cohesive elements is 0.125 mm. Mesh convergence is found by varying the element size, and the same general assumptions as described in Section 2.2 are presumed.

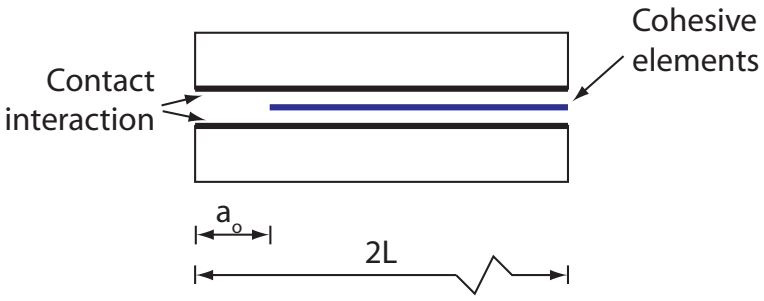

Figure 6.2: Exploded schematic illustration of an ENF specimen in the finite element model. Zero-thickness cohesive elements constitute the bonding between the beams, and contact interaction prevents interpenetration.

Three idealised cohesive laws are considered, one representing a laminate without z-pins (triangular) and two representing z-pinned laminates (triangular and trapezoidal), see Figure 6.3. The cohesive laws with an area below the traction-separation curve of 5000 J/m^2 and critical displacement $\delta_c = 0.5$ mm correspond to z-pinned laminates, whereas area and critical displacement for laminates with no z-pins are reduced to 1/10 of the triangular z-pinned case, which is an approximate estimate based on previous experience. The three cohesive laws are used as examples to test the influence of the cohesive law on the fracture behaviour of the specimen. The triangular and trapezoidal shapes are chosen since they are simple and adequate for initial analysis. The properties of the cohesive laws are illustrated in Figure 6.3 and listed in Table 6.2.

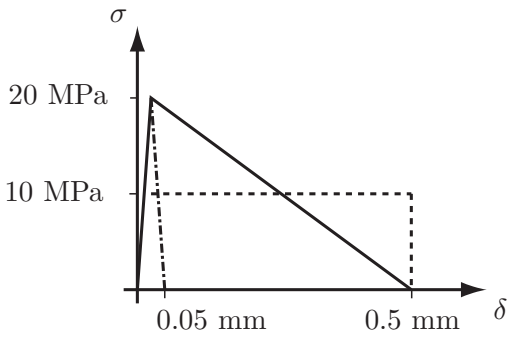

Figure 6.3: Cohesive laws used in the simulations.

	σ_o[MPa]	δ_c[mm]	J_c[J/m^2]
Not reinforced (triangular)	20	0.05	500
Reinforced (triangular)	20	0.5	5000
Reinforced (trapezoidal)	10	0.5	5000

Table 6.2: Properties defining the three cohesive laws.

In a cohesive zone model there is no crack tip singularity. Instead the position of the crack tip

is assumed to be the point where damage starts, i.e. the point where the cohesive traction-displacement relation deviate from the initial linear regime. The crack tip constitutes the front edge of the process zone and for the cohesive laws in this study the crack tip is given by the displacement $\delta_o = \sigma_o/k = 1.7$ and 3.3 microns for the trapezoidal and triangular-shaped cohesive laws, respectively. The trailing edge of the process zone is found at $\delta_c = 0.5$ mm and $\delta_c = 0.05$ mm for laminates with or without z-pins, respectively.

6.2.3 Loading History

In the simulation the specimen is loaded in displacement control with the boundary conditions indicated in Figure 6.1. The loading history is an idealisation of described experimental loading conditions similar to what can be achieved with a split Hopkinson pressure bar with a special pulse shaper, see Weerasooriya et al. (2006). The velocity of the load point is zero at time $t = 0$ and increased linearly to a constant speed v_o over the time t_o, see Figure 6.4. If v_o is small and t_o large, the loading situation is quasi-static. If, conversely, the velocity is large and t_o approaches zero, the loading corresponds to a hard impact and the acceleration in the time interval 0 to t_o becomes large.

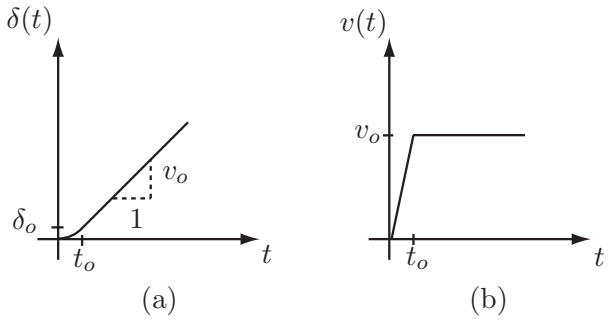

Figure 6.4: Schematic displacement (a) and velocity (b) histories for the load point in the simulations.

It is important to acknowledge that the ramp time t_o will have a large influence on the dynamic fracture behaviour of the specimen. If the ramp time is very short natural vibrations of the specimen may be exited, leading to an oscillating stress state near the crack tip. The challenge is to choose a ramp time sufficiently small to obtain rapid crack growth, yet sufficiently large to avoid a highly fluctuating fracture behaviour. Andrews (2005) analysed the effect of ramp time on the dynamic amplification of the energy release rate for specimens with a stationary crack. Here it was found that if the ramp time was equal to the first natural vibration period T_1, there was no dynamic amplification, and no subsequent oscillations. Conversely, smaller rise times led to oscillations in the specimen. The cases studied in Andrews (2005) are different from the present since loading is force controlled (the force is increased linearly instead of displacement), and the crack is stationary. However, by considering the fracture behaviour of the tested specimens at various ramp times, T_1 is

found to be a suitable compromise to obtain rapid crack growth while limiting stress wave effects.

An eigenvalue analysis of the specimen is performed. During the analysis the specimen is supported at the three points where it is connected to the test machine in three-point bending, cf. Figure 6.1. The bond-line outside the pre-crack is assumed intact and the nodes between the two beams are fixed except along the pre-crack where cohesive elements are inserted. The cohesive elements are given a very large stiffness in the normal direction and a negligible stiffness towards tangential deformation, which is chosen to allow sliding but restrain normal opening of the pre-crack during the analysis. This ensures that only the relevant natural vibration modes will appear in the analysis, i.e. normal opening of the pre-crack is prohibited. For a specimen of length $2L = 100$ mm the oscillation period is $T_1 = 188$ microseconds, i.e. a ramp time $t_o = 188$ microseconds is chosen. Additionally, for a longer specimen of $2L = 210$ mm, $T_1 = 558$ microseconds, which is chosen as the ramp time for the simulations of long specimens described in Section 6.3.3.

6.2.4 Possible Output from Simulations and Experiments

The long-term goal of this study is to extract cohesive laws from dynamic experiments by varying the cohesive law in the simulation until numerical and experimental results coincide. The following results may be considered for this purpose: (1) the force-displacement relation at the load point and (2) optical measurements of the displacement field along the process zone. Full-field displacements may be measured using a Digital Image Correlation (DIC) system, typically able to track displacements with a resolution below 1 micron. The DIC measurements may further be used to extract the sliding speed in the process zone, which is suitable as a rate measure, as will be explained in the following section. The relative sliding displacement in the specimen is illustrated schematically by arrows in Figure 6.5.

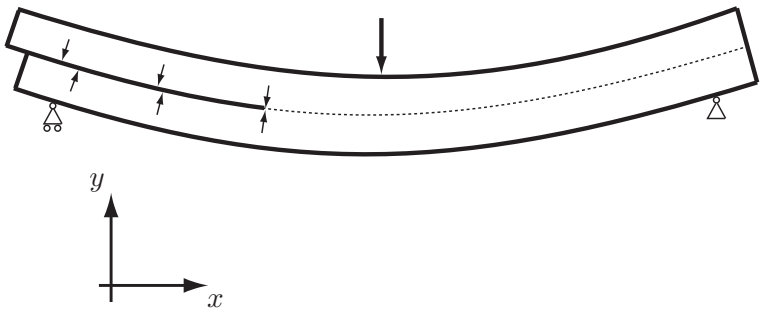

Figure 6.5: Relative sliding displacement in the process zone of a loaded ENF specimen indicated by arrows.

6.2.5 Remarks on Describing Rate in a CZM

As mentioned in Section 6.1.1 many earlier studies consider the influence of rate on fracture toughness for brittle materials, see e.g Tsai et al. (2001). In those studies the measure of rate is the propagation speed of the crack tip, which is reasonable since the fracture energy dissipation is confined to a small area close to the crack tip. However, in the presence of LSB the crack tip speed is no longer suitable as a measure of rate, which is explained below.

The overall objective of this study is to develop methodologies for extracting cohesive laws at different rates and subsequently use these laws to simulate high speed fracture of other geometries. The relation between opening/sliding displacement of the pre-crack tip and crack length (see e.g. schematic illustration in Figure 3.1) is not a material property and depends on the geometry and size of the specimen (Bao and Suo (1992)). From this it can be inferred that the relation between opening/sliding speed in the precess zone and crack tip speed also depends on size and geometry. The process zone opening/sliding speed dictates the rate at which e.g. z-pins are being pulled out of the laminate. Furthermore, when a rate dependent cohesive law is implemented in a cohesive zone model it is straightforward to obtain the sliding/opening speed from the degrees of freedom of the elements while the crack tip speed is not directly obtained from the individual elements. It is therefore simpler and more intuitively correct to use the local sliding/opening speed instead of the crack tip speed as a variable to be coupled with the implemented rate dependent cohesive law.

In the following example a schematic illustration of the cohesive law is presented in a 3-D diagram with the three axes being sliding displacement, shear traction and sliding speed. Assume a linear (triangle-shaped) cohesive law where the critical stresses of the fracture mechanisms increase with rate and the critical length δ_c is rate independent. The cohesive law would accordingly turn out as illustrated in Figure 6.6.

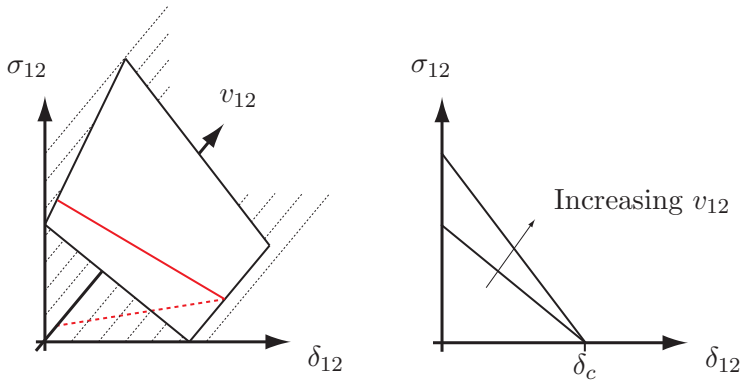

Figure 6.6: Schematic illustration of a possible rate dependence for a cohesive law, i.e. effect of increasing sliding speed v_{12} on the cohesive law.

The sliding speed in the process zone is not necessarily constant even though the crack tip speed is, i.e. the sliding speed near the leading edge of the process zone is usually smaller than near the trailing edge. Considering a fixed point at the intact ligament of the specimen,

the sliding velocity at the point will vary as the process zone passes. The red line in Figure 6.6 illustrates a possible loading history scenario (variation of δ_{12}, σ_{12} and v_{12}) from considering a single point in the process zone, i.e. a single cohesive element in the model, as the process zone passes.

6.3 Results for Quasi-static Loading

It is beneficial first to consider the results from quasi-static loading in order to subsequently understand the behaviour of the high rate loaded specimen and distinguish between the static and the dynamic effects. In the quasi-static analysis in this study a loading rate ($v_0 = d\delta/dt = 0.05$ m/s) is found to be sufficiently slow (convergence analysis shows that no visible dynamic effects appear in the results) and a further reduction is not pursued, since this will increase the computational time due to the increased number of time increments. The dimensions of the considered specimen are given in Figure 6.1, and the implemented cohesive laws are illustrated in Figure 6.3.

6.3.1 Laminate without z-pins

In Figure 6.7 results regarding force vs. displacement and crack length vs. displacement are plotted for quasi-static loading of a specimen with no through-thickness reinforcements ($J_c = 500$ J/m^2). Consider the force-displacement relation in subplot a): Initially, the force increases approximately linear until a load point displacement of 0.55 mm. Here the crack propagates unstably, which entails a sudden drop in the applied load and a small amount of oscillations are triggered as seen in the reaction force history. In subplot b), the positions of the leading and trailing edges of the process zone are plotted as a function of load point displacement. During the unstable crack propagation the process zone translates at a constant size at a speed of 290 m/s, until the crack tip reaches the midpoint of the specimen (i.e. 50 mm on the y-axis of subplot b)). Subsequently, the process zone translates stably along the bond line as the loading point displacement is increased. To perform a check on the results a straight dashed line is included in subplot a), that represents the calculated load-displacement relation of the fully cracked specimen. This is calculated from beam theory by assuming two centre loaded, simply supported beams each of thickness h, see Massabò et al. (1998). As expected the load-displacement relation approaches this line as the crack length increases.

The process zone length as a function of load point displacement (found as the distance between the leading and trailing edges of the process zone, i.e. vertical distance between curves in Figure 6.7 subplot b)) is plotted in Figure 6.8. It is found that a maximum process zone size of 13.5 mm is reached just before the unstable crack growth occurs, while the process zone monotonically decreases throughout the remaining part of the simulation. The size variation of the process zone during the build-up and crack propagation is qualitatively

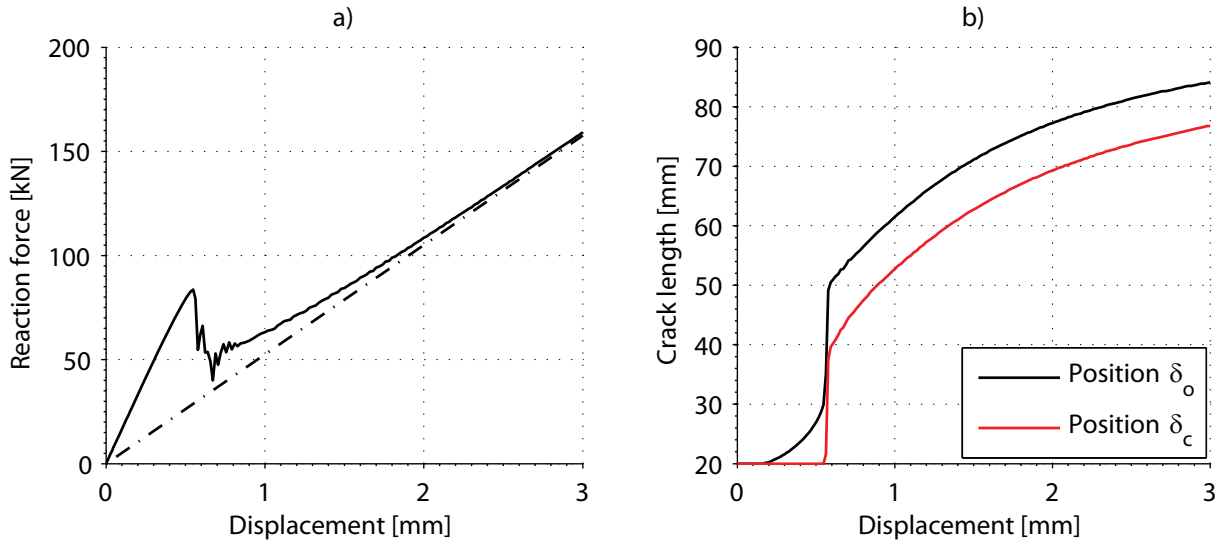

Figure 6.7: Results for quasi-statically loaded ENF specimen with 2L = 100 mm and cohesive law corresponding to triangular with no reinforcements ($\delta_c = 0.05$ mm). In both sub-plots the x-axis represents the load point displacement, see Figure 6.1. The sub-figures are a) reaction force in loading point, and b) position of leading (black line) and trailing (red line) edge of the process zone. The dashed line in subplot b) is the load-displacement curve of a completely damaged specimen (two beams each of thickness h) calculated from beam theory.

similar to the predicted behaviour of a DCB loaded in mode I, see Figure 10 in Suo et al. (1992).

6.3.2 Laminate with z-pins

Results for the cases representing laminates with z-pins are plotted in Figure 6.9. Dashed lines represent trapezoidal cohesive law, whereas solid lines represent the triangular. By considering the reaction force in subplot a) it is found that in contrast to the case without z-pins unstable crack growth does not occur, due to the large process zone initially developing as described in Section 6.1.1. Consider the crack length plot in subplot b): Regarding the specimen with a triangular cohesive law (solid line), the crack tip departs from the pre-crack tip at a loading displacement of 0.2 mm and the process zone subsequently builds up. As the crack tip passes the centre of the specimen (i.e. the load point corresponding to 50 mm on the y-axis) the curve suddenly changes slope, and from here the crack tip moves at a monotonically decreasing rate relative to the load point displacement. The process zone size vs. load point displacement is plotted as the solid line in Figure 6.10, and results are qualitatively similar to the non-reinforced case plotted in Figure 6.8.

The specimen with a trapezoidal cohesive law represented by dashed lines in Figure 6.9 fractures much different from the triangular case (solid lines). Since the critical stress σ_o is only half that for the triangular law, the process zone develops at a smaller load and the

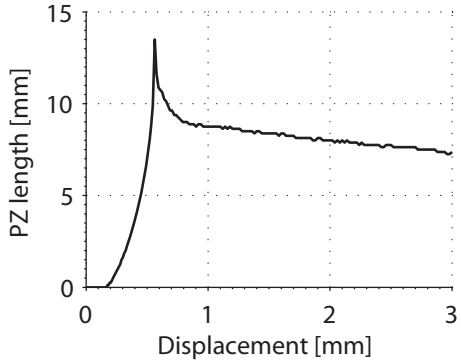

Figure 6.8: Process zone length as a function of loading displacement, i.e. the vertical distance between the black and red lines in Figure 6.7 b).

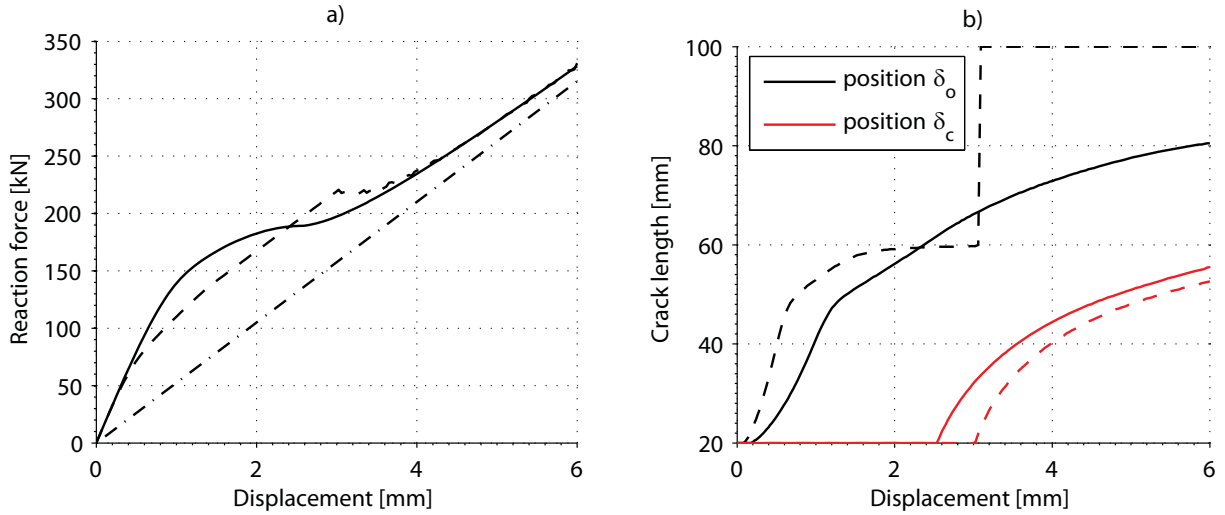

Figure 6.9: Results for a mode II ENF specimen loaded under quasi-static conditions with $2L = 100$ mm, $a_o = 20$ mm and $J_c = 5000$ J/m^2. Cohesive laws correspond to fracture properties with reinforcements where the solid line represents the triangle-shaped and the dashed is the trapezoidal.

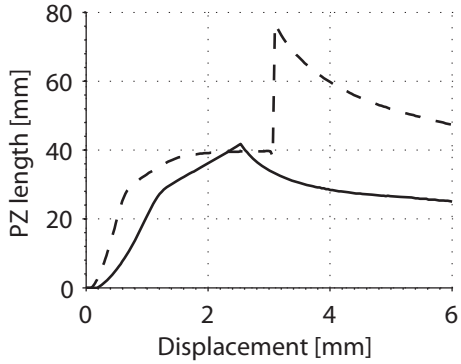

Figure 6.10: Process zone length corresponding to results described in Figure 6.9.

specimen is more compliant during the first 2 mm of loading displacement, see subplot a). In subplot b) the crack tip apparently instantly changes position from 60 mm to 100 mm at a loading displacement of 3 mm, which is explained in the following: The nominal shear stress distribution along the bond-line of a mode II loaded ENF specimen (when ignoring the stress concentration due to the notch and edge effects) is constant with a change of sign at the midpoint where the load is applied. A process zone might start at a distance from the pre-notch if the shear stress in the intact ligament exceeds the critical stress σ_o. This occurs in the case of the trapezoidal law. Consider Figure 6.11 subplot a): The stresses in the normal and tangential directions along the cohesive elements in the intact ligament of the specimen is shown at a fixed time corresponding to a loading displacement of 1.2 mm. In the left part of the specimen (x-coordinate below 50 mm), the process zone has developed from the pre-crack for both cases, since stresses have reached the critical values $\sigma_o = 20$ MPa and $\sigma_o = 10$ MPa, respectively. In the right half ($x > 50$ mm), the specimen is undamaged, however, the specimen with the trapezoidal law (dashed line) is close to initiating a second process zone, since σ_{12} is approaching -10 MPa. In subplot b) the equivalent opening and sliding displacements of the cohesive elements are shown. A sliding displacement between 0.003 and 0.5 mm i.e. between δ_o and δ_c of the cohesive law, indicates that the considered cohesive element is inside the process zone.

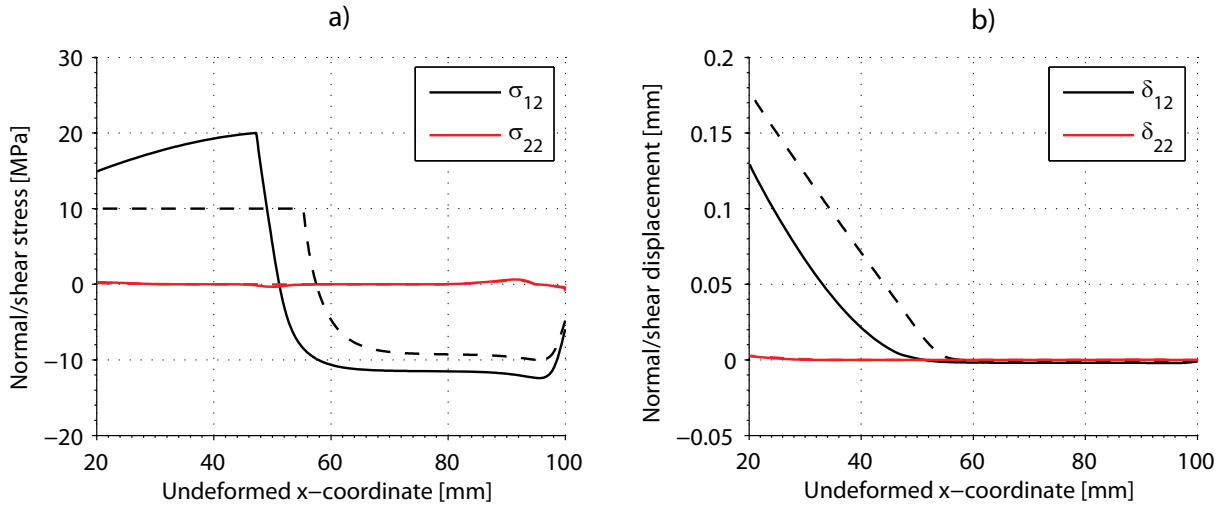

Figure 6.11: Stresses and relative displacements along cohesive elements at a loading displacement of 1.2 mm. The pre-notch tip is located at x = 20 mm. The solid line represents the triangular cohesive law and dashed represents the trapezoidal, and the simulation is the same as presented in Figure 6.9.

In Figure 6.12 subplot a) the stress distribution in the cohesive elements is plotted at a loading displacement of 3 mm. Consider the trapezoidal case (dashed line) in subplot a): Two separate process zones have developed, and are completely covering the left and right part of the specimen, since the stress is constant +10 or -10 MPa in the cohesive elements (the critical traction value of the trapezoidal cohesive law). The load situation shown is the limiting case just before the two process zones join which occurs as the sliding displacement

of the pre-crack tip exceeds the critical displacement $\delta_c = 0.5$ mm, see subplot b) at $x = 20$ mm. The described stress and displacement distribution in the cohesive elements along the bond line at load point displacements of 1.2 and 3.0 mm respectively, can be compared to the reaction-force and crack length plots in Figure 6.9. As the two process zones join at a load point displacement of 3.0 mm, the apparent crack tip instantly moves from 60 mm to 100 mm (from the crack tip position of the first to the second process zone illustrated in Figure 6.12 a)).

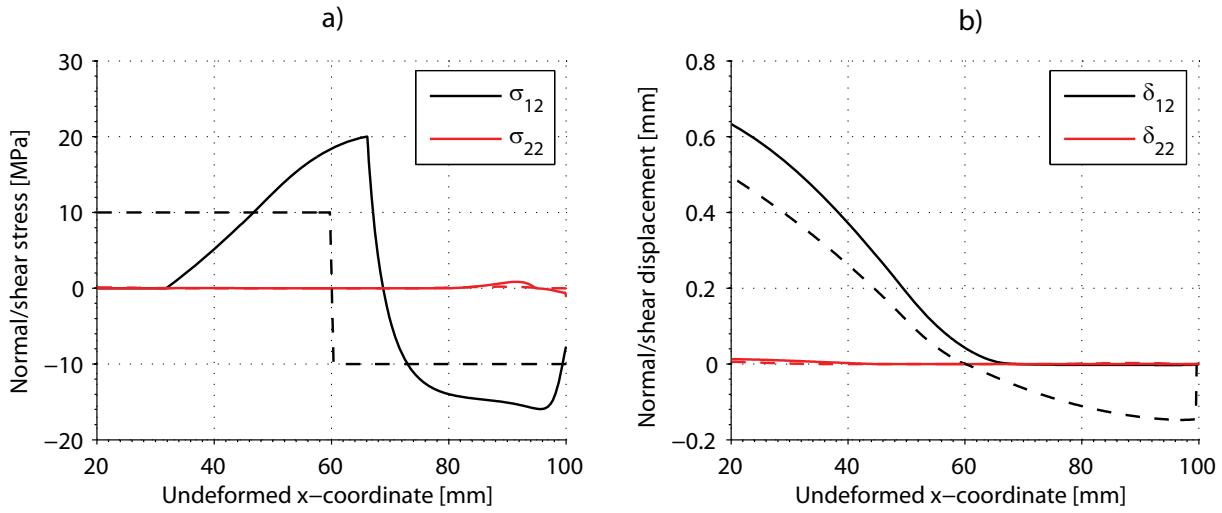

Figure 6.12: Stress and relative displacements along cohesive elements at a loading displacement of 3 mm. Solid line indicates a triangular cohesive law and dashed indicates a trapezoidal. The simulation is the same as in Figure 6.9.

It may be concluded from this section, that when dealing with the ENF specimen combined with a cohesive law with a relatively large value of the dimensionless expression $\overline{E}J_I^c/\sigma_o^2 h$ (presented in Section 2.2.6), multiple process zones may develop in the specimen. This phenomena may be reduced by increasing the length of the specimen, which is shown in the following section.

6.3.3 Effect of Increasing Specimen Length

As found from the analysis of a specimen of a length of $2L = 100$ mm, two independent process zones develop in the case of the trapezoidal cohesive law. Simulations show that this does not occur as the specimen is remarkably longer (for the quasi-static load-case). By increasing the length L and the pre-crack length a_o while a fixed L/a_o ratio is maintained the crack propagates at a smaller load. Since the nominal shear stress is proportional to the force applied to the loading point, the shear stress in the intact ligament distant from the pre-crack will not exceed the critical stress σ_o before the crack has propagated throughout the specimen. Results for specimens with z-pins and length $2L = 210$ mm are plotted in Figure 6.13.

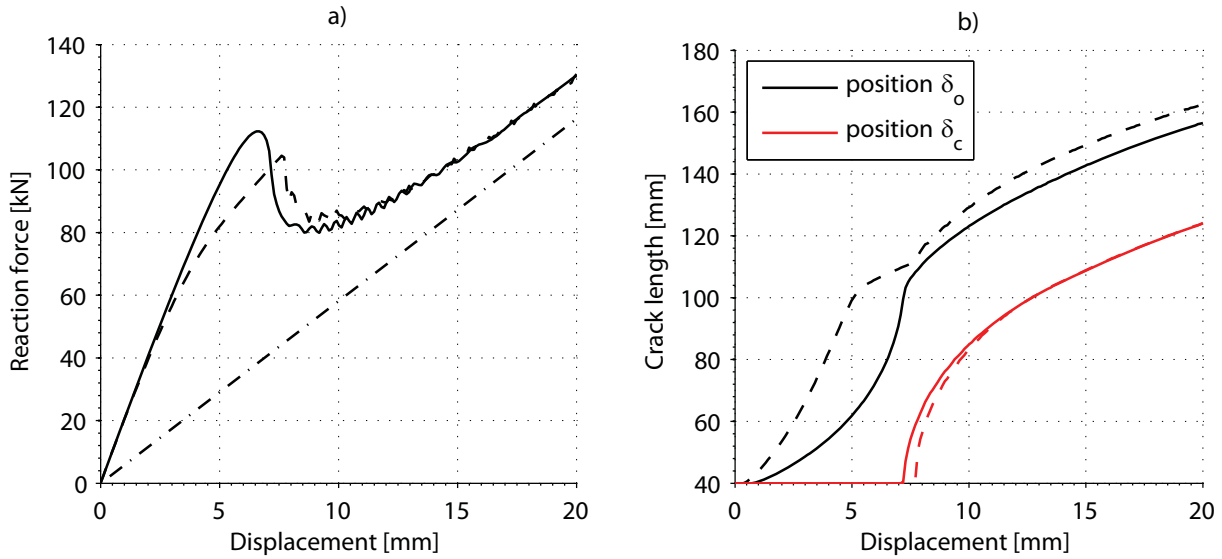

Figure 6.13: Quasi-static results for large specimen, $2L = 210$ mm, $a_o = 40$ mm and $J_c = 5000$ J/m^2. Cohesive laws correspond to fracture properties with reinforcements, the solid line is triangular and the dashed is trapezoidal.

An additional advantage of increasing the specimen length is that the intact ligament in the specimen becomes longer, and the possibility for the process zone to develop and obtain a certain speed before reaching the end of the specimen is increased. However, it is found from comparing Figures 6.9 and 6.13 that the process zone is bigger for the longer specimens, which reduces the advantage. Furthermore, as described previously, high rate loading of the longer specimen triggers natural vibration modes and oscillations to a larger extend than for the shorter specimens. Therefore the shorter specimens are preferred for high-rate loading, which is the theme in the following sections.

6.4 Results for High-speed Loading

In the following results are presented for specimens with z-pins loaded at high speed. Results are described at various rates with either a trapezoidal or a triangle-shaped cohesive law. Furthermore, a simple method is suggested for relating the process zone sliding speed with the crack tip speed and displacement profile.

6.4.1 Laminates with z-pins Loaded at High Speed

Initially consider results at a load point velocity $v_o = 20$ m/s in Figure 6.14. By comparing to the quasi-static case in Figure 6.9, it is found that there are visible dynamic effects, especially for the reaction force in subplot a) in the form of oscillations, whereas the crack

length history in subplot b) seems less affected. In the loading displacement interval of 4.0 to 5.0 mm, see subplot b), the leading and trailing edges move at approximately the same constant velocity of 140 m/s), and furthermore, the sliding displacement profile is also constant within this load point displacement interval, as will be elaborated in Section 6.4.2. A similar interval appears for other loading rates between 10 and 50 m/s and the crack propagation speed and process zone sliding speed within the constant interval are given in Table 6.3.

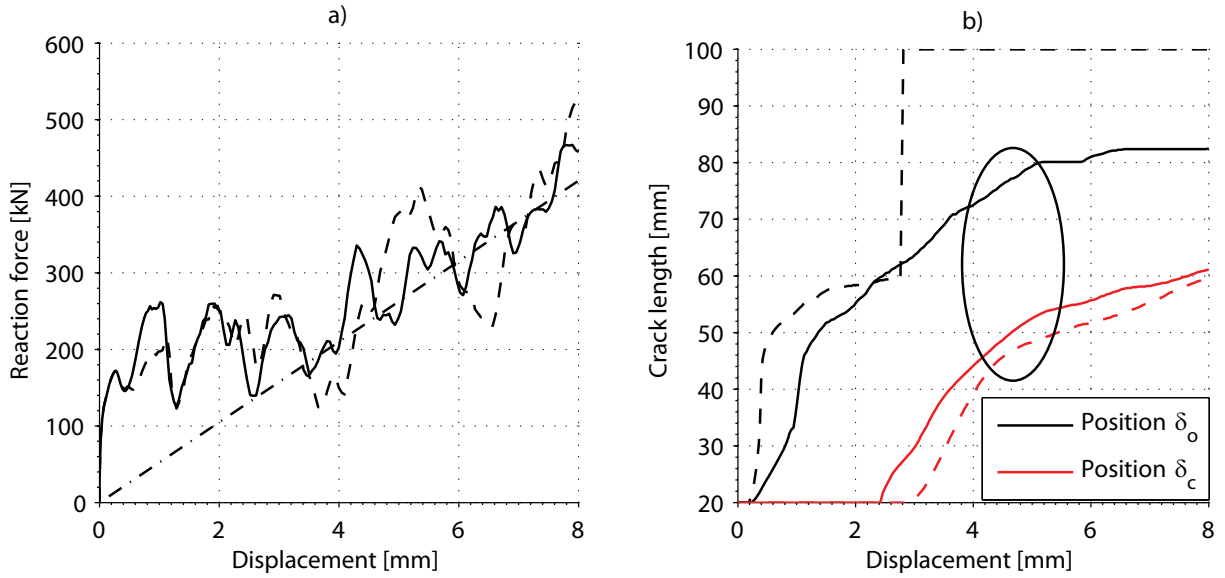

Figure 6.14: Results for specimen with $2L = 100$ mm, $a = 20$ mm and $v = 20$ m/s. Cohesive laws correspond to a z-pinned laminate, the solid line is triangular and the dashed is trapezoidal.

Loading speed [m/s]	Crack tip speed [m/s]	PZ sliding speed (at trailing edge) [m/s]
10	85.1	2.3
20	140	4.7
30	236	6.7
40	273	7.7
50	271	7.5

Table 6.3: Crack tip velocities and process zone sliding velocities obtained during various loading rates.

The maximum crack propagation velocity in Table 6.3 is 273 m/s, which is reached at a loading velocity of 40 m/s. An increase in loading velocity to 50 m/s does not lead to increased propagation speed, however, instead the high loading speed has the disadvantage of multiple process zones developing and increased oscillations, which makes results more difficult to interpret. Results for sliding speed in the process zone, as found in the third

column of Table 6.3, are measured at the trailing edge, since the sliding speed varies inside the process zone. This is elaborated in the following section.

6.4.2 Sliding Velocity in the Process Zone

As explained in Section 6.2.5, the process zone sliding speed is useful as a rate measure, since it describes the rate of the fracture processes (e.g. by which z-pins are pulled out). The following shows by an example a simple method for relating the sliding speed in the process zone to the crack displacement profile and crack tip speed (both are experimentally measurable quantities using a DIC system). Consider Figure 6.14 subplot b): The crack speed becomes approximately constant within a small range corresponding to load point displacements between four and five mm. The following describes a simple method for calculating the sliding speed in the process zone from the displacement profile and crack tip speed.

The opening velocity of a pure mode I crack is analogous to the sliding velocity of a pure mode II crack, which is the topic of this study, but for illustration purposes a mode I crack is considered in the following. A schematic illustration of a propagating mode I crack is presented in Figure 6.15. If the opening profile is constant in a certain loading interval, the opening speed of a fixed point in the process zone may be found from the crack tip speed and the displacement profile

$$\frac{du(x)}{dt} = \frac{du(x)}{dx}\frac{dx}{dt} = \frac{du(x)}{dx}v_{tip} \tag{6.1}$$

where $u(x)$ is the opening displacement as a function of x, t is time and v_{tip} is the speed of the crack tip in the x-direction. For illustration purposes the opening profile $u(x)$ in Figure 6.15 is linear, whereas it is non-linear in the general case.

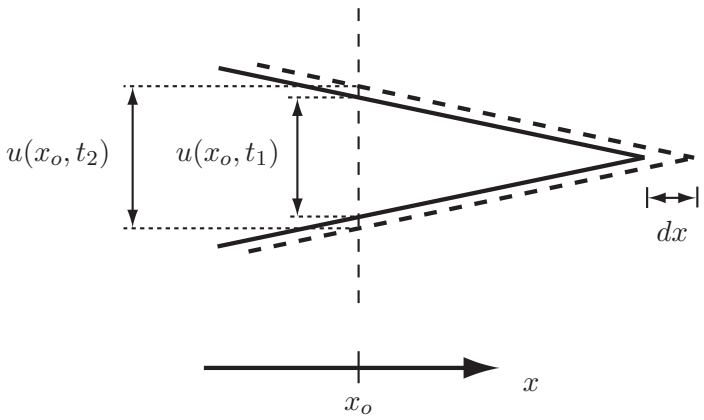

Figure 6.15: Schematic illustration of opening profile for a pure mode I crack.

In the following example, the sliding velocity is found from the numerical results in two ways: (1) in accordance with the right-hand side of Eq. (6.1), where the opening displacement

profile $u(x)$ of the process zone at time t_n is differentiated with regard to the x-direction and multiplied by the crack tip speed, and (2) from the difference in displacement between two time steps divided by the time step, i.e. $(u(x,t_n)-u(x,t_{n-1}))/(t_n-t_{n-1})$, where (t_n-t_{n-1}) is the time step between outputs from the simulation equal to 1/200 of the total time domain. The found sliding velocity profiles are plotted in Figure 6.16 for times corresponding to loading displacements of 4.0, 4.3, 4.6 and 4.9 mm.

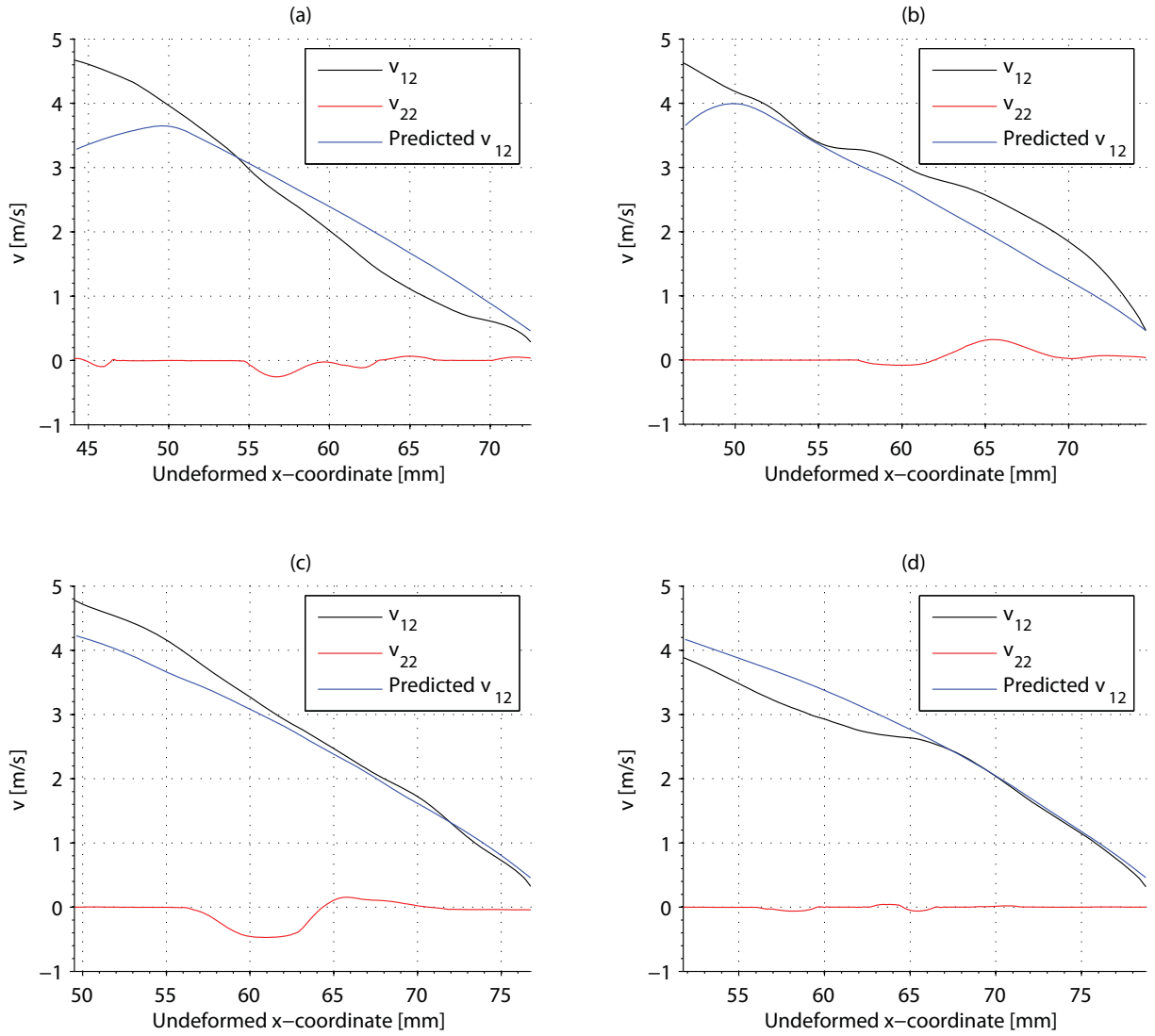

Figure 6.16: Actual and predicted relative sliding speeds in the process zone. The simulation corresponds to results in Figure 6.14 at load point displacements of 4.0, 4.3, 4.6 and 4.9 mm in subplot (a), (b), (c), and (d), respectively.

It is found that the measured and predicted sliding speed profiles correlate fairly well, which indicates that the method could be used to approximate the process zone sliding speed. The approach is only valid when the crack tip speed and the displacement profile are constant,

which only occurs for a limited interval in the simulation. The sliding speed varies within the process zone from a minimum at the leading edge to a maximum at the trailing edge. The maximum sliding speed in the process zone within the considered loading interval is approximately 4.7 m/s for a loading speed of 20 m/s, see Figure 6.16. The sliding speeds at the trailing edge of the process zone for various loading speeds of 10-50 m/s are listed in Table 6.3.

6.5 Discussion and Perspectives

The aim of the present study is to demonstrate the behaviour of the ENF specimen loaded at high rates and to identify the sensitivity of the shape of the cohesive law on the dynamic fracture response. For the quasi-static case observed in Figure 6.9 the difference in reaction force between triangular and trapezoidal cohesive laws is up to 25 % at load point displacements below 3.5 mm. This difference is significant compared to the expected noise that will unavoidably enter the experimental measurements, thus the reaction force may potentially be used to back-trace the cohesive law by changing the cohesive law in the finite element model until numerical and experimental results coincide. Subsequently consider results for the dynamic loading case in Figure 6.14. From the reaction forces in subplot a) there is a visible difference between the responses from specimens with triangular and trapezoidal cohesive laws, however, it is difficult to relate a certain response to a certain shape of cohesive law due to oscillations in the specimen. As the process zone develops, the cohesive law will influence the compliance of the specimen, which again influences the natural frequency and observed oscillation modes. Due to the many interrelated variables, it is difficult to deduce a cohesive law from the reaction force results in the dynamic loading case.

A more promising output is the relative sliding displacement of the process zone during high-rate loading of the specimen, see Figure 6.17 b). This plot shows results for trapezoidal and triangle shaped cohesive laws at $v_o = 20$ m/s and a load point displacement of 4.0 mm. Here it is clearly possible to distinguish between the two cohesive laws (dashed and solid lines). The difference in sliding displacement at the pre-crack tip (x-coordinate of 20 mm) is approximately 0.1 mm, which is several orders of magnitude higher than the resolution of a typical DIC system (1 micron), and the experimentally measured full-field displacement images may be used to extract the cohesive law, similarly to what is conducted under slow loading rate in Massabò et al. (1998).

From the various analysis conducted at loading speeds between 0.05 and 50 m/s it is found that at a loading rate of 40 m/s the crack tip speed reaches 273 m/s for the z-pinned laminate, whereas a loading of 50 m/s does not increase the crack propagation speed further. Instead this increases the triggering of higher order natural frequencies which makes results difficult to interpret. The maximum crack velocity of 273 m/s corresponds to a sliding velocity near the trailing edge of the process zone of 7.7 m/s, and it is found that the crack tip speed and process zone sliding speed increase successively as the loading speed v_o is increased from 0 to 40 m/s.

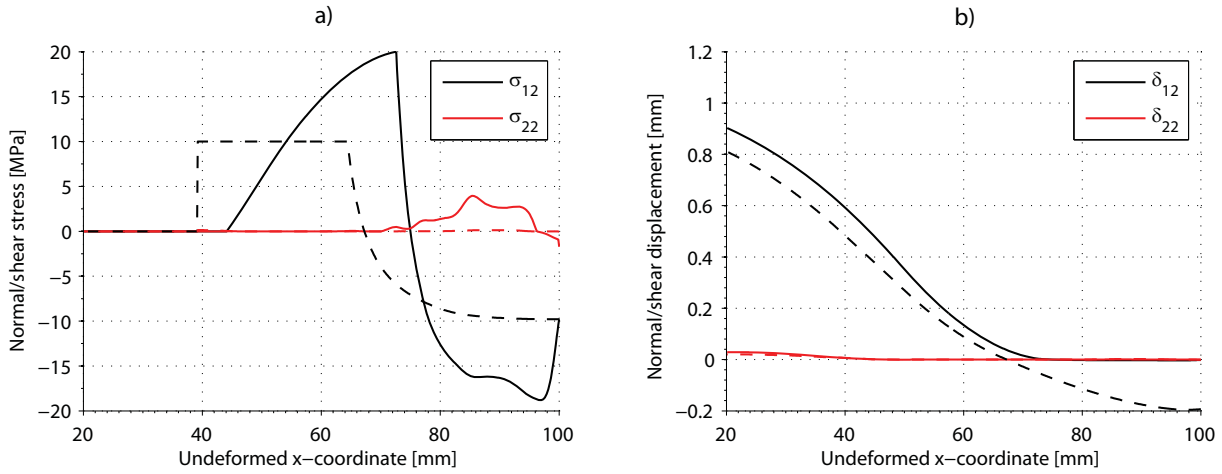

Figure 6.17: Stresses and relative displacements in cohesive elements at a loading displacement of 4.0 mm. The loading speed is $v_o = 20$ m/s and the simulation is the same as in Figure 6.14.

The cohesive law implemented in the finite element model is not rate dependent, due to the restrictions of the cohesive elements in ABAQUS, however, the model may still be used to extract rate dependent cohesive laws. By comparing displacement profiles from experimental and numerical results at various loading rates between 0 and 40 m/s a cohesive law may be extracted and associated with the sliding speed distribution in the process zone, which is approximately constant in a certain interval, see example in Figure 6.14. By repeating the analysis at various loading rates, a set of cohesive laws at various rates may be obtained.

For both quasi-static and dynamic loading of z-pinned specimens the crack tip has passed the midpoint of the specimen before the trailing edge of the process zone departs from the pre-crack tip. In order to extract information about the full cohesive law, it is necessary to use experimental data from crack propagation in the second half of the specimen. Friction between the cracked faces might influence the results since the contact forces are high near the centre of the specimen (load point). The possible effects of friction on the experimental output is not considered within the scope of this study.

Liu et al. (2007) showed that specimens with z-pins might be rate dependent even at loading rates much slower than the ones considered in this study. A large difference in the reaction forces was observed when a fibre was pulled out of a matrix material at rates of 1 mm/min and 100 mm/min, respectively, which is much slower than a process zone sliding velocity between 2 and 7 m/s as considered in this study. Various loading rates where the kinetic energy is negligible (quasi-static conditions prevail) might still be rate dependent, and these cases are also relevant to study.

As described in Section 6.3.1 the crack propagates unstably for approximately 20 mm in the specimen without z-pins loaded under quasi-static conditions. As the force becomes high enough to drive the pre-crack, part of the stored elastic energy is dissipated into propagating

the crack rapidly for approximately 20 mm. The cohesive law implemented in ABAQUS is not rate dependent and the crack does not propagates unstably due to any rate effects as described in the Introduction. Instead the unstable crack propagation occurs as a result of the short pre-crack ($a_o = 0.4L$) combined with a relatively small process zone in the case without z-pins.

Stiffness and strength properties of composite materials are often rate dependent, see e.g. Song et al. (2003), and it is necessary to explore the effect of a change in e.g. E-modulus due to high-rate loading. If the varying E-modulus has a large effect on the deduced cohesive law it is necessary to take the varying material properties into account in the model. This is out of the scope of this study, but should be considered in the future.

The work conducted in this chapter considers extracting cohesive laws during high rate fracture of monolithic composite materials with TTR. This falls well within the title of the thesis "Predicting and Improving Damage Tolerance of Composite Structures", however, it is not clear how the study fits with the other chapters that deal with sandwich structures. Still, from the perspective of CZM the chapters are fairly well connected, and approximately the same theory, basic understanding, and models for simulation are applicable to all studies mentioned in this thesis. This chapter is an initial step towards using known methodologies from the static regime in the dynamic regime. The same could be considered for sandwich specimens in a future study.

6.6 Summary

A purely numerical study using a 2-D finite element model on the assumption of plain strain is used to predict the static and dynamic fracture behaviour of an ENF specimen loaded in three-point bending. The model includes inertia in order to investigate the effect of high loading speed in the range of 0.05 to 50 m/s, and the effect of choosing an appropriate rise time for the load is discussed. Zero thickness cohesive elements are embedded between bulk elements along the bond line, and these show a traction-separation behaviour corresponding to composite specimens both with and without z-pins. At slow quasi-static loading, stable crack propagation is observed for z-pinned laminates and unstable for specimens without z-pins. At a loading rate of 40 m/s the crack tip speed reaches 273 m/s for the z-pinned laminate, whereas loading above 40 m/s does not increase the crack propagation speed, but leads to a highly oscillating behaviour of the specimens, which makes results difficult to interpret. A second process zone may initiate distant from the pre-crack for large $\overline{E}J_I^c/\sigma_o^2 h$ values, however the tendency of this behaviour may be reduced by increasing the length of the specimen. Conventionally, the crack tip speed is used as a rate measure when dealing with brittle fracture, however, in the presence of LSB it is more suitable to measure rate by the opening/sliding speed in the process zone. Finally, a simple method for relating the sliding speed to the displacement profile and crack tip speed is proposed.

This page is intentionally left blank.

Chapter 7

Conclusions and Future Work

7.1 Predicting the Damage Tolerance of Debonded Sandwich Structures

The major objective of this thesis is to develop methodologies for predicting the fracture behaviour of sandwich structures with face/core debonds. The development involves two overall steps: (1) measuring the cohesive law at various mixed-mode loadings from fracture mechanics tests, and (2) implementing the cohesive laws in a finite element model, subsequently used for simulating the fracture behaviour of different geometries and loading conditions.

In **step (1)**, a modified sandwich Double Cantilever Beam loaded by Uneven Bending Moments (DCB-UBM) specimen is proposed, where the modifications entail adhering steel layers to the sandwich faces to reduce deflections. Analysis of the specimen is made, and the J integral is derived analytically using laminate beam theory. By relating the J integral value to the pre-crack tip opening of the DCB-UBM test, cohesive laws are derived directly without use of finite element analysis. The stiff steel layers have the effect that the J integral is insensitive to variations in the (more compliant) composite sandwich faces, and inaccurate properties of these will not affect the calculated J integral value substantiably.

During production of sandwich test specimens a layer of randomly oriented fibres is inserted between face and core, either in the form of a Chopped Strand Mat (CSM) with fibre strands of 2-5 cm or as a Continuous Filament Mat (CFM) with long fibre strands. For mode I dominated loadings the crack tends to propagate in the CSM or CFM layer with large-scale bridging developing in the crack wake. Generally, the shape of the cohesive laws measured in this study, suggest that the fracture processes may be parted into two branches, see e.g. Figure 3.19: The first branch represents cracking of the resin at a relatively large stress level around 5 MPa, and the second branch is the large-scale fibre bridging with stresses gradually decreasing from around 0.5 MPa to zero. The opening displacement as the cohesive tractions

vanish is generally between 5 and 10 mm (depending on the mode-mixity of the loading), see Figure 3.22. Since the area below the curve in the second branch is relatively large, fibre bridging may contribute substantially to the fracture resistance. Whether large-scale bridging occurs or not depends on the interlaminar position of the crack in the CSM or CFM layer and bridging is mostly developing as the crack is propagating near the centre of the CSM or CFM layer. The interlaminar position of the crack is sensitive to the mode-mixity, which in the DCB-UBM experiment is controlled by the ratio between the applied moments. For the CSM case the fracture resistance varies between 0.8 kJ/m^2 at small amounts of fibre bridging and 1.6 kJ/m^2 at large amounts of fibre bridging, while for the CFM case the fracture resistance is between 0.8 and 2.4 kJ/m^2.

A finite element model of the DCB-UBM specimen is generated, in order to associate the moment ratio M_1/M_2 with a mode-mixity measure. The mode-mixity may either be calculated from the normal and shear stresses at the crack tip, or from the average stress distribution in the process zone, and it is believed that the crack tip measure is the most sensitive to attributes that govern the crack kinking behaviour, which to a high extend dictates the fracture resistance. The relation between mode-mixity, interlaminar crack tip position and fracture resistance is found from the DCB-UBM experiments, and subsequently used to predict the fracture behaviour of a different geometry.

In **step (2)**, a fracture test of a sandwich component is conducted, where a debond crack is propagated by pulling the sandwich face apart from the core, and the test is designated the Sandwich Tear Test (STT). The boundary conditions have the effect that the mode-mixity at the crack tip changes gradually from mode I dominated to intermediate mixed-mode as the crack propagates. Thus, the test is highly versatile as regards testing the methodology in a large mode-mixity spectrum. Two lay-up configurations are tested, with different mats of randomly oriented fibres inserted between face and core, i.e. CSM or CFM, and the two cases show significantly different behaviour regarding crack kinking and force-displacement relation. In the *CSM* case the numerical model overestimates the load necessary to propagate the crack by up to 50 % relative to the experiments. From a parametric study it is found that deviations are likely to be related to the measured steady state fracture resistance J_c, i.e. area below the curve of the cohesive law rather than the detailed shape, which the load-displacement curve of the STT specimen is not specifically sensitive to. Various sources for deviation are discussed e.g. the mode-mixity measure available in ABAQUS, which averages over the loading history of the cohesive element. The mode-mixity measure should depend on the attributes that govern crack kinking, and it is believed that a local mode-mixity measure at the crack tip is more appropriate than the present measure used by ABAQUS. By a simple comparison study of the predicted J_c values it is estimated that deviations may be reduced by changing mode-mixity measure from φ_σ to φ_o, which is not currently possible in ABAQUS. Regarding the *CFM* case the scatter is significant between the tested specimens, and some fit the numerical predictions, others do not. Conversely to the CSM case, the numerical predictions are conservative regarding the average experimental behaviour. Again it is found that the disagreement between numerical and experimental results may be reduced by changing the mode-mixity measure.

7.2 Improving the Damage Tolerance of Debonded Sandwich Structures

A face/core debond crack in a sandwich structure may propagate in three basic ways: (1) propagate self-similarly in the interface, (2) kink into the face, or (3) kink into the core. Which scenario is preferred from the designer's point of view depends on the circumstances. However, it is desired to be able to influence the crack propagation path by modifying the sandwich interface design. The optimal fracture scenario (as considered in this thesis) is one where an initial face/core debond crack will propagate in the layer of randomly oriented fibres (CSM or CFM), and subsequently be arrested here due to the developed large-scale fibre bridging. In order to design such an interface, conflicting interests appear, since to arrest the crack, the fracture resistance of the layer should be high, which usually promotes crack kinking into the adjacent face or core. Various aspects of crack kinking are discussed, and it is believed that the crack path is mainly governed by the initial separation fracture energy J_o and critical stress σ_o, whereas the fracture resistance is related to the steady state fracture energy $J_c = J_o + J_{bridging}$. An optimal interface would therefore have a small J_o and small σ_o to keep the crack in the interface, and a large $J_{bridging}$ to stop the crack from propagating further. Results show that crack propagation in the CSM or CFM layer entails a crack tip fracture toughness of approximately 0.4 kJ/m^2, while the total fracture energy J_c is in the range from 0.8 to 1.6 kJ/m^2 for CSM and 0.8 to 2.4 kJ/m^2 for CFM, depending on the mode-mixity. Thus, J_o is relatively small and $J_{bridging}$ relatively large and this combination is believed to be beneficial for keeping the crack in the interface, while requiring a large crack driving force to propagate the crack.

It is found from DCB-UBM tests that the fracture toughness of the core material is approximately 2.5 kJ/m^2, so the core is superior to the CSM or CFM mat regarding fracture toughness and crack kinking from the CSM or CFM and into the core would entail an increased fracture resistance. The true potential of the designed interface is not obtained until the steady state fracture resistance of the CSM or CFM layer is larger than the fracture toughness of the core, and the proposed interface design may be more advantageous when used in structures with lighter and brittler cores.

As the mode-mixity becomes sufficiently high, the crack kinks from the CSM or CFM layer and into the quadraxial layers of the face. For some sandwich structures this behaviour may be critical, and it is desired to be able to predict and perhaps prevent this behaviour. A numerical and experimental investigation regarding predicting the crack kinking behaviour of the STT specimen is conducted. It is generally found that the sequence of layers where the crack will propagate is predictable along with a rough estimate of the positions where the crack kinks. A modification of the interface is proposed by inserting a thin woven layer between the quadraxial face layers and the CSM or CFM mat. It is shown that the mode-mixity transition where kinking occurs is extended significantly due to the woven mat, and this behaviour is observed both for the DCB-UBM and the STT experiments. The crack never penetrates the woven layer but for moderate mode II cases the crack propagates in

the resin between the woven and the CSM or CFM layer. Furthermore, in the case of large mode II loadings, a secondary crack is initiated on the opposite side of the woven layer.

7.3 Dynamic Fracture of Composite ENF Specimens

A purely numerical study examines the fracture behaviour of an ENF specimen loaded in three-point bending for the eventual purpose of designing a fracture specimen for extracting cohesive laws in the dynamic regime. The material properties chosen resemble those of a carbon-fibre/epoxy composite with through-thickness reinforcements (e.g. z-pins), thus LSB is expected during fracture, which is modelled by a cohesive zone. The study examines the sensitivity of the shape of the cohesive law to the experimentally measurable output, with the purpose of designing an information rich test specimen suitable for extracting cohesive laws in the dynamic regime. Simulations are conducted at various load point speeds from 0 to 50 m/s and the following observations are made: At load point speeds up to 40 m/s a load point displacement range appears where the crack tip speed and size of the process zone are approximately constant. It is believed that cohesive laws may be extracted from the experimental output from these regimes and associated with a fixed fracture rate. At a load point speed of 40 m/s the crack tip speed is 273 m/s, whereas loading rates above 40 m/s do not increase the crack tip speed further but instead lead to various unwanted dynamic effects, such as increased specimen oscillation and multiple process zones developing in the specimen.

It is necessary to associate the eventually extracted cohesive laws with a certain rate, and the rate measure should be chosen so it can be transferred freely between various specimen sizes and geometries. The crack tip speed is not suitable as a rate measure, since it depends on the geometry of the specimen rather than solely on fracture processes occurring in the process zone. A more suitable rate measure is the relative opening and sliding speed of the cracked faces inside the process zone. For the conducted simulations, results show that the sliding speed varies with a minimum at the leading edge and a maximum at the trailing edge. A simple method for determining the opening/sliding speed in the process zone from the crack tip speed and the opening/sliding displacement profile is suggested, and results from the simulations are used to support the proposed method.

Whether or not the experimentally obtainable results are information rich with regard to extracting high-rate cohesive laws depends on the response of the specimen on the shape of the cohesive law. Results suggest that the displacement profile, e.g. measured by a DIC system, is sensitive to the cohesive law in opposition to the reaction force, where dynamic effects tend to overrule the effects of the cohesive law.

7.4 Future Work

The fracture resistance of a sandwich interface crack is highly governed by the interlaminar position of the crack, and this must be accounted for. Crack kinking may be predicted by linking experimental observations to a mode-mixity measure, and presently, the mode-mixity measures for the cohesive elements in ABAQUS depend on the complete loading history of the element rather than only the stress situation at the crack tip. The mode-mixity measure should depend on the attributes that govern crack kinking, and it is believed that a local mode-mixity measure at the crack tip is more appropriate than the present measure used by ABAQUS. A systematic investigation of this is needed and should be conducted in the future.

In this thesis the effect of inserting a mat with randomly oriented fibres near the face/core interface is investigated experimentally, along with the effects of various woven mats as regards preventing the crack from kinking into the load carrying part of the face. It is found that the full potential of the design is not reached, since the fracture toughness of the core is larger than the steady state fracture toughness of the CSM and CFM layer (more energy is dissipated as the crack propagates in the core rather than in the interface). The study should be expanded to lighter and brittler cores. Furthermore, the effect of increasing the bonding between the face and the woven mat inserted between CSM/CFM and load carrying face laminate should be considered, since this might increase the mode-mixity range where the crack will kink into the face. The bonding could be improved, by e.g. stitching the woven layer to the face, before resin injecting the sandwich panel.

Results from the sandwich DCB-UBM tests show that the crack often propagates unstably in jumps of 2-5 cm. Sun et al. (2008) describes how the "crack initiation toughness" as the crack is stationary may be significantly different from the "crack arrest toughness", and for adhesives tested in Sun et al. (2008) it was estimated that the fracture toughness was reduced around a factor of four during unstable crack growth. In the present study only the "crack initiation toughness" values are measured from the DCB-UBM experiments, which may be unconservative in the case of fast crack growth. It is necessary to account for unstable crack growth, even during slowly increasing loading conditions, thus, procedures for extracting cohesive laws during unstable/fast crack propagation in sandwich structures are needed.

The numerical work conducted in this thesis assumes 2-D conditions, whereas to accommodate more complicated geometries a 3-D model is necessary. This entails the appearance of a second shear direction, and properties for this direction needs to be defined and measured. Besides this, the implementation is analogous to the 2-D case described in this thesis.

Only monotonic loading is considered in this thesis, while for many cases fatigue constitutes the design limiting load case. In this study it is investigated whether fibre bridging may be utilised to increase the fracture resistance of a face/core debond under monotonic loading, while the behaviour under cyclic loading may be completely different. Thus, it is needed to perform mixed-mode fracture tests on sandwich specimens under cyclic loading.

As regards the numerical analysis of high-rate fracture behaviour of ENF specimens, the current study is only an initial step towards extracting cohesive laws during high-rate fracture. A comparison to experimental observations is vital and high-rate experiments are currently being prepared at University of Purdue, following the design recommendations from this study. In future work, procedures should be developed for deducing cohesive laws by obtaining interference between experimental and numerical results. Furthermore, it is necessary to prepare the implementation of rate dependant cohesive laws in commercial finite element codes, e.g. ABAQUS, which is currently not available.

References

Abaqus, d. (2006), Abaqus Analysis User's Manual Version 6.6, *Simula*.

Alfano, G. (2006), On the influence of the shape of the interface law on the application of cohesive-zone models, *Composites Science and Technology*, 66(6):723–730, ISSN 02663538.

Andersson, T. and Stigh, U. (2004), The stress-elongation relation for an adhesive layer loaded in peel using equilibrium of energetic forces, *International Journal of Solids and Structures*, 41(2):413–434, ISSN 00207683.

Andrews, M. G. (2005), *The static and dynamic interaction of multiple delaminations in plates subjected to cylindrical bending*, Dissertation ph.d. degree, Northwestern University, IL, USA.

ASTM (1996), *ASTM D5528-94a, Standard Test Method for Mode I Interlaminar Fracture Toughness of Unidirectional Fiber-Reinforced Polymer Material*, American Society for Testing and Materials.

Bao, G. and Suo, Z. (1992), Remarks on crack-bridging concepts, *Applied Mechanics Reviews*, 45(8):355–366.

Barenblatt, G. (1959), The formation of equilibrium cracks during brittle fracture. General ideas and hypotheses. Axially-symmetric cracks, *Journal of Applied Mathematics and Mechanics*, 23(3):622–636, ISSN 00218928.

Berggreen, C. (2004), *Damage tolerance of debonded sandwich structures*, Ph.D. thesis, Technical University of Denmark.

Berggreen, C., Lundsgaard-Larsen, C., Karlsen, K., Jenstrup, C. and Hayman, B. (2007a), Improving performance of polymer fiber reinforced sandwich X-joints in naval vessels - Part I: Design Aspects, *16th International Conference on Composite Materials*, Kyoto, Japan.

Berggreen, C. and Simonsen, B. (2005), Non-uniform Compressive Strength of Debonded Sandwich Panels - II. Fracture Mechanics Investigation, *Journal of Sandwich Structures and Materials*, 7:483–518, ISSN 10996362.

Berggreen, C., Simonsen, B. and Borum, K. (2007b), Experimental and numerical study of interface crack propagation in foam-cored sandwich beams, *Journal of Composite Materials*, 41(4):493–520, ISSN 00219983.

Blackman, B., Hadavinia, H., Kinloch, A. and Williams, J. (2003), The use of a cohesive zone model to study the fracture of fibre composites and adhesively-bonded joints, *International Journal of Fracture*, 119(1):25–46, ISSN 03769429.

Böhme, W. and Kalthoff, J. (1982), The behavior of notched bend specimens in impact testing, *International Journal of Fracture*, 20(4):R139–43, ISSN 03769429.

van den Bosch, M., Schreurs, P. and Geers, M. (2006), An improved description of the exponential Xu and Needleman cohesive zone law for mixed-mode decohesion, *Engineering Fracture Mechanics*, 73(9):1220–1234, ISSN 00137944.

Budiansky, B., Fleck, N. and Amazigo, J. (1998), On kink-band propagation in fiber composites, *Journal of the Mechanics and Physics of Solids*, 46(9):1637–53, ISSN 00225096.

Camanho, P., Davila, C. and De Moura, M. (2003), Numerical simulation of mixed-mode progressive delamination in composite materials, *Journal of Composite Materials*, 37(16):1415–38, ISSN 00219983.

Cantwell, W. and Davies, P. (1996), A study of skin-core adhesion in glass fibre reinforced sandwich materials, *Applied Composite Materials*, 3(6):407–20, ISSN 0929189x.

Cantwell, W. J. and Blyton, M. (1999), Influence of loading rate on the interlaminar fracture properties of high performance composites - A review, *Applied Mechanics Reviews - Including Supplement*, 52(6):199, ISSN 00036900.

Carlberger, T. and Biel, A. (2008), Influence of temperature and strain rate on cohesive properties of a structural epozy adhesive (paper c), *PhD thesis: Adhesive Joining for Crashworthiness Material Data and Explicit FE-methods*, 1(1).

Carlsson, L., Gillespie, J. and Pipes, R. (1986), On the analysis and design of the end notched flexure (ENF) specimen for mode II testing, *Journal of Composite Materials*, 20(6):594–604, ISSN 00219983.

Carlsson, L., Matteson, R., Aviles, F. and Loup, D. (2005), Crack path in foam cored DCB sandwich fracture specimens, *Composites Science and Technology*, 65(15-16):2612–2621, ISSN 02663538.

Carpinteri, A. and Massabò, R. (1996), Bridged versus cohesive crack in the flexural behavior of brittle-matrix composites, *International Journal of Fracture*, 81(2):125–45, ISSN 03769429.

Cook, J. and Gordon, J. (1964), A mechanism for the control of crack propagation in all-brittle systems, *Proceedings of the Royal Society of London, Series A (Mathematical and Physical Sciences)*, 282(1391):508–520, ISSN 00804630.

Cox, B. (2005), Snubbing effects in the pullout of a fibrous rod from a laminate, *Mechanics of Advanced Materials and Structures*, 12(2):85–98, ISSN 15376494.

Cox, B., Dadkhah, M. and Morris, W. (1996), On the tensile failure of 3D woven composites, *Composites Part A: Applied Science and Manufacturing (Incorporating Composites and Composites Manufacturing)*, 27(6):447–458, ISSN 1359835x.

Cox, B. and Marshall, D. (1991), The determination of crack bridging forces, *International Journal of Fracture*, 49(3):159–76, ISSN 03769429.

Cox, B. and Marshall, D. (1994), Concepts for bridged cracks in fracture and fatigue, *Acta Metallurgica et Materialia*, 42(2):341–363, ISSN 09567151.

Cox, B., Sridhar, N. and Beyerlein, I. (2001), Inertial effects in the pullout mechanism during dynamic loading of a bridged crack, *Acta Materialia*, 49(18):3863–3877, ISSN 13596454.

D3433-93, A. (1993), *Standard test method for fracture strength in cleavage of adhesive in bonded joints*, American Society for Testing and Materials.

Dantuluri, V., Maiti, S., Geubelle, P. H., Patel, R. and Kilic, H. (2007), Cohesive modeling of delamination in Z-pin reinforced composite laminates, *Composites Science and Technology*, 67(3-4):616–631, ISSN 02663538.

Dharmawan, F., Thomson, R. S., Li, H., Herszberg, I. and Gellert, E. (2004), Geometry and damage effects in a composite marine T-joint, *Composite Structures*, 66(1-4):181–187, ISSN 02638223.

DIAB (2008), www.diabgroup.com.

Dugdale, D. (1960), Yielding of steel sheets containing slits, *Journal of the Mechanics and Physics of Solids*, 8(2):100–104, ISSN 00225096.

El-Sayed, S. and Sridharan, S. (2002), Cohesive layer models for predicting delamination growth and crack kinking in sandwich structures, *International Journal of Fracture*, 117(1):63–84, ISSN 03769429.

Freitas, G., Magee, C., Dardzinski, P. and Fusco, T. (1994), Fiber Insertion Process for Improved Damage Tolerance in Aircraft Laminates, *Journal of Advanced Materials - SAMPE*, 25(4):36, ISSN 10709789.

Griffith, A. (1920), The phenomena of rupture and flow in solids, *Royal Society of London – Philosophical Transactions*, 221(A 587):163–198, ISSN noissn1191514470.

Gu, P. (1994-1995), Notch sensitivity of fiber-reinforced ceramics, *International Journal of Fracture*, 70(3):253–266, ISSN 03769429.

He, M. and Hutchinson, J. W. (1989), Crack deflection at an interface between dissimilar elastic materials, *International Journal of Solids and Structures*, 25(9):1053–1067, ISSN 00207683.

Högberg, J. and Stigh, U. (2006), Specimen proposals for mixed mode testing of adhesive layer, *Engineering Fracture Mechanics*, 73(16):2541–2556, ISSN 00137944.

Hutchinson, J. W. and Jensen, H. M. (1990), Models of fiber debonding and pullout in brittle composites with friction, *Mechanics of Materials*, 9(2):139–163, ISSN 01676636.

Inglis, C. (1913), Stresses in a plate due to the presence of cracks and sharp corners, *Proceedings of the Institute of Naval Architects*, 55:219–230.

Jacobsen, T. and Sørensen, B. (2001), Mode I intra-laminar crack growth in composites-modelling of R-curves from measured bridging laws, *Composites Part A (Applied Science and Manufacturing)*, 32A(1):1–11, ISSN 1359835x.

Jenstrup, C. and Karlsen, K. (2007), *Design of core inserts in sandwich X-joints - Experimental and numerical analysis*, Master's thesis, Technical University of Denmark.

Kinloch, A. and Williams, J. (1980), Crack blunting mechanisms in polymers, *Journal of Materials Science*, 15(4):987–96, ISSN 00222461.

Krasnov, V., Kuznetsov, V. and Maksakov, A. Y. (1987), Automated method of transverse reinforcement of composites by short fibers, *Mechanics of Composite Materials (English translation of Mekhanika Kompozitnykh Materialov)*, 23(3):356–361, ISSN 01915665.

Leffler, K., Alfredsson, K. and Stigh, U. (2007), Shear behaviour of adhesive layers, *International Journal of Solids and Structures*, 44(2):530–545, ISSN 00207683.

Li, H., Dharmawan, F., Herszberg, I. and John, S. (2006a), Fracture behaviour of composite maritime T-joints, *Composite Structures*, 75(1-4):339–350, ISSN 02638223.

Li, S., Thouless, M., Waas, A., Schroeder, J. and Zavattieri, P. (2005a), Use of a cohesive-zone model to analyze the fracture of a fiber-reinforced polymer-matrix composite, *Composites Science and Technology*, 65(3-4):537–549, ISSN 02663538.

Li, S., Thouless, M., Waas, A., Schroeder, J. and Zavattieri, P. (2005b), Use of mode-I cohesive-zone models to describe the fracture of an adhesively-bonded polymer-matrix composite, *Composites Science and Technology*, 65(2):281–293, ISSN 02663538.

Li, S., Thouless, M., Waas, A., Schroeder, J. and Zavattieri, P. (2006b), Mixed-mode cohesive-zone models for fracture of an adhesively bonded polymer-matrix composite, *Engineering Fracture Mechanics*, 73(1):64–78, ISSN 00137944.

Li, S., Wang, J. and Thouless, M. (2004), The effects of shear on delamination in layered materials, *Journal of the Mechanics and Physics of Solids*, 52(1):193–214, ISSN 00225096.

Li, X. and Carlsson, L. (1999), The tilted sandwich debond (TSD) specimen for face/core interface characterization, *Journal of sandwich structures and materials*, 1:60–75.

Liu, H.-Y., Yan, W., Yu, X.-Y. and Mai, Y.-W. (2007), Experimental study on effect of loading rate on mode I delamination of z-pin reinforced laminates, *Composites Science and Technology*, 67(7-8):1294–1301, ISSN 02663538.

Lundsgaard-Larsen, C., Berggreen, C., Karlsen, K., Jenstrup, C. and Hayman, B. (2007), Improving performance of polymer fiber reinforced sandwich X-joints in naval vessels - Part II: Damage Tolerance, *16th International Conference on Composite Materials*, Kyoto, Japan.

Lundsgaard-Larsen, C., Sørensen, B. F., Berggreen, C. and Østergaard, R. C. (2008), A modified DCB sandwich specimen for measuring mixed-mode cohesive laws, *Engineering Fracture Mechanics*, 75(8):2514–2530, ISSN 00137944.

Massabò, R., Mumm, D. R. and Cox, B. (1998), Characterizing Mode II Delamination Cracks in Stitched Composites, *International Journal of Fracture*, 92(1):1–38, ISSN 03769429.

Needleman, A. (1987), A continuum model for void nucleation by inclusion debonding, *Transactions of the ASME. Journal of Applied Mechanics*, 54(3):525–31, ISSN 00218936.

Nøkkentved, A., Lundsgaard-Larsen, C. and Berggreen, C. (2005), Non-uniform Compressive Strength of Debonded Sandwich Panels - I. Experimental Investigation, *Journal of Sandwich Structures and Materials*, 7:461–482, ISSN 10996362.

Østergaard, R. (2008), Buckling driven debonding in sandwich columns, *International Journal of Solids and Structures*, 45(5):1264–82, ISSN 00207683.

Østergaard, R., Sørensen, B. and Brøndsted, P. (2007), Measurement of Interface Fracture Toughness of Sandwich Structures under Mixed Mode Loadings, *Journal of Sandwich Structures and Materials*, 9:445, ISSN 10996362.

Parmigiani, J. and Thouless, M. (2006), The roles of toughness and cohesive strength on crack deflection at interfaces, *Journal of the Mechanics and Physics of Solids*, 54(2):266–287, ISSN 00225096.

Petersson, P. (1981), *Crack growth and development of fracture zones in plain concrete and similar materials*, Ph.D. thesis, Lund institute of technology.

Ravi-Chandar, K. and Balzano, M. (1988), On the mechanics and mechanisms of crack growth in polymeric materials, *Engineering Fracture Mechanics*, 30(5):713–727, ISSN 00137944.

Rice, J. (1968), A path independent integral and the approximate analysis of strain concentrations by notches and cracks, *Journal of Applied Mechanics*, 35(14):379–86.

Sharpe, W. N., J. and Böhme, W. (1994), Dynamic fracture toughness measurements on small Charpy specimens - a preliminary study, *Journal of Testing and Evaluation*, 22(1):14–19, ISSN 00903973.

Soden, P., Hinton, M. and Kaddour, A. (2002), Biaxial test results for strength and deformation of a range of E-glass and carbon fibre reinforced composite laminates: failure exercise benchmark data, *Composites Science and Technology*, 62(12-13):1489–1514, ISSN 02663538.

Solaimurugan, S. and Velmurugan, R. (2008), Influence of in-plane fibre orientation on mode I interlaminar fracture toughness of stitched glass/polyester composites, *Composites Science and Technology*, 68(7-8):1742–1752, ISSN 02663538.

Song, B., Chen, W. and Weerasooriya, T. (2003), Quasi-static and dynamic compressive behaviors of an S-2 glass/SC15 composite, *Journal of Composite Materials*, 37(19):1723–43, ISSN 00219983.

Sørensen, B. and Jacobsen, T. (1998), Large-scale bridging in composites: R-curves and bridging laws, *Composites Part A: Applied Science and Manufacturing (Incorporating Composites and Composites Manufacturing)*, 29(11):1443–1451, ISSN 1359835x.

Sørensen, B. and Jacobsen, T. (2003), Determination of cohesive laws by the J integral approach, *Engineering Fracture Mechanics*, 70(14):1841–1858, ISSN 00137944.

Sørensen, B. and Kirkegaard, P. (2006), Determination of mixed mode cohesive laws, *Engineering Fracture Mechanics*, 73(17):2642–2661, ISSN 00137944.

Sørensen, B. F., Jørgensen, K., Jacobsen, T. K. and Østergaard, R. C. (2006), DCB-specimen loaded with uneven bending moments, *International Journal of Fracture*, 141(1):163–176, ISSN 03769429.

Spearing, S. and Evans, A. (1992), The role of fiber bridging in the delamination resistance of fiber-reinforced composites, *Acta Metallurgica et Materialia*, 40(9):2191–9, ISSN 09567151.

Sridhar, N., Yang, Q. and Cox, B. (2003), Slip, stick, and reverse slip characteristics during dynamic fibre pullout, *Journal of the Mechanics and Physics of Solids*, 51(7):1215–1241, ISSN 00225096.

Stigh, U. (1987), Initiation and growth of an interface crack, *Mechanical behaviour of adhesive joints*, pp. 237–48.

Sun, C., Thouless, M., Waas, A., Schroeder, J. and Zavattieri, P. (2008), Ductile-brittle transitions in the fracture of plastically-deforming, adhesively-bonded structures. Part I: Experimental studies, *International Journal of Solids and Structures*, 45(10):3059–3073, ISSN 00207683.

Suo, Z., Bao, G. and Fan, B. (1992), Delamination R-curve phenomena due to damage, *Journal of the Mechanics and Physics of Solids*, 40(1):1–16, ISSN 00225096.

Suo, Z. and Hutchinson, J. (1990), Interface crack between two elastic layers, *International Journal of Fracture*, 43(1):1–18, ISSN 03769429.

Toftegaard, H. and Lystrup, A. (2005), Design and test of lightweight sandwich T-joint for naval ships, *Composites Part A*, 36(8):1055–1065, ISSN 1359835x.

Tomashevskii, V., Romanov, D., Shalygin, V. and Panfilov, N. (1980), Effect of radial reinforcement on the strength of glass-plastic shells in loading with external pressure, *Mechanics of Composite Materials*, 16(2):139–44, ISSN 01915665.

Truxel, A., Aviles, F., Carlsson, L. A., Grenestedt, J. L. and Millay, K. (2006), Influence of Face/Core Interface on Debond Toughness of Foam and Balsa Cored Sandwich, *Journal of Sandwich Structures and Materials*, 8:237, ISSN 10996362.

Tsai, J., Guo, C. and Sun, C. (2001), Dynamic delamination fracture toughness in unidirectional polymeric composites, *Composites Science and Technology*, 61(1):87–94, ISSN 02663538.

Tvergaard, V. (1990), Effect of fibre debonding in a whisker-reinforced metal, *Materials Science and Engineering: A*, 125(2):203–213, ISSN 09215093.

Tvergaard, V. and Hutchinson, J. (1992), The relation between crack growth resistance and fracture process parameters in elastic-plastic solids, *Journal of the Mechanics and Physics of Solids*, 40(6):1377–1397, ISSN 00225096.

Tvergaard, V. and Hutchinson, J. W. (1993), The influence of plasticity on mixed mode interface toughness, *Journal of the Mechanics and Physics of Solids*, 41(6):1119–1135, ISSN 00225096.

Viana, G. M. and Carlsson, L. A. (2003), Influences of Foam Density and Core Thickness on Debond Toughness of Sandwi ch Specimens with PVC Foam Core, *Journal of Sandwich Structures and Materials*, 5:103, ISSN 10996362.

Weerasooriya, T., Moy, P., Casem, D., Cheng, M. and Chen, W. (2006), A four-point bend technique to determine dynamic fracture toughness of ceramics, *Journal of the American Ceramic Society*, 89(3):990–5, ISSN 00027820.

Xie, D., Salvi, A., Sun, C., Waas, A. and Caliskan, A. (2006), Discrete cohesive zone model to simulate static fracture in 2D triaxially braided carbon fiber composites, *Journal of Composite Materials*, 40(22):2025–46, ISSN 00219983.

Xie, D. and Waas, A. M. (2006), Discrete cohesive zone model for mixed-mode fracture using finite element analysis, *Engineering Fracture Mechanics*, 73(13):1783–1796, ISSN 00137944.

Xu, X. P. and Needleman, A. (1993), Void nucleation by inclusion of debonding in a crystal matrix, *Modelling and Simulation in Materials Science and Engineering*, 1(2):111–132, ISSN 09650393.

Yang, Q. and Cox, B. (2005), Cohesive models for damage evolution in laminated composites, *International Journal of Fracture*, 133(2):107–137, ISSN 03769429.

Yang, Q. and Thouless, M. (2001), Mixed-mode fracture analyses of plastically-deforming adhesive joints, *International Journal of Fracture*, 110(2):175–187, ISSN 03769429.

Zenkert, D. (1995), *An Introduction to Sandwich Construction*, Chameleon Press Ltd., London.

Appendix A

DCB-UBM Specimen Deflection Kinematics

In this section the DCB-UBM sandwich specimen is analysed by utilising the Kirchhoff beam theory. The specimen kinematics is analysed when loaded by varying moment ratios M_1/M_2, and various crack lengths.

The opening of the pre-crack tip is analysed by means of Kirchoff beam theory. Since the beams are loaded by pure moments, the bending radius is constant and can be calculated as a function of applied moments and the extension, coupling and bending terms A_b, B_b and D_b for each of the two beams. Considering Figure 3.13, the opening between point q_2 and q_3 in the global coordinate system is given by ($M_1 \neq 0$)

$$\delta_x^* = \left(R_1 - \frac{H_1}{2}\right)\sin\theta_1 - \left(R_2 + \frac{H_2}{2}\right)\sin\theta_2 \tag{A.1}$$

$$\delta_y^* = \left(R_2 + \frac{H_2}{2}\right)(1-\cos\theta_2) - \left(R_1 - \frac{H_1}{2}\right)(1-\cos\theta_1) \tag{A.2}$$

where R_b is the midplane radius of beam b given by

$$R_b = \frac{1}{\kappa_b} = \frac{D_b - B_b^2/A_b}{M_b} \tag{A.3}$$

The beam thicknesses are $H_1 = t_s + t_f$ and $H_2 = t_s + t_f + t_c$, where t_s, t_f and t_c are the thicknesses of the stiffening material, face and core, respectively. The rotations are given by $\theta_b = L/R_b$, where L is the beam (crack) length (from q_2 and q_3 to crack tip).

For $M_1 = 0$, (A.1) and (A.2) should be replaced by

$$\delta_x^* = L - \left(R_2 + \frac{H_2}{2}\right)\sin\theta_2 \tag{A.4}$$

$$\delta_y^* = \left(R_2 + \frac{H_2}{2}\right)(1 - \cos\theta_2) \tag{A.5}$$

The displacements in the (x, y) coordinate system are transformed into the (n, t) coordinate system rotated θ_3 relative to the global coordinate system according to the standard transformation law:

$$\left\{ \begin{array}{c} \delta_t^* \\ \delta_n^* \end{array} \right\} = \left\{ \begin{array}{c} \delta_x^* \cos\theta_3 + \delta_y^* \sin\theta_3 \\ -\delta_x^* \sin\theta_3 + \delta_y^* \cos\theta_3 \end{array} \right\} \tag{A.6}$$

In Figure A.1 the δ_n^*-δ_t^* relationship is plotted for varying moment ratio (M_1/M_2) and varying crack length normalised by the specimen width. The normalised fracture toughness is constant $J/(E_s t_s) = 8 \cdot 10^{-7}$ and the normalised width $B/t_s = 5$, where E_s and t_s are Young's modulus and the thickness of the stiffening material.

Figure A.1 shows the normal and tangential crack opening relationship for a fixed J value. Several things are of interest. For a fixed M_1/M_2 ratio, as is the case during a single test (described later), the δ_n^*-δ_t^* relationship is non-linear, especially for small crack length (L/B) and as the crack length increases the curves turn more toward normal opening. The maximum obtainable M_1/M_2 value is reached when the two crack flanges are coincident, i.e. $\theta_1 = \theta_2$. For the considered specimen this occurs when $M_1/M_2 \approx 4.89$, which is the ratio between the bending stiffnesses of the two beams. It should be observed that M_1/M_2 needs to be rather close to this value to obtain tangentially dominated openings. It should also be noted that for a fixed L/B ratio, the magnitude of the crack opening decreases with increasing M_1/M_2. For instance, with a beam length of $L/B = 3$, $\delta_n^*/t_s \approx 0.47$ for pure normal opening and $\delta_t^*/t_s \approx 0.15$ for pure tangential opening.

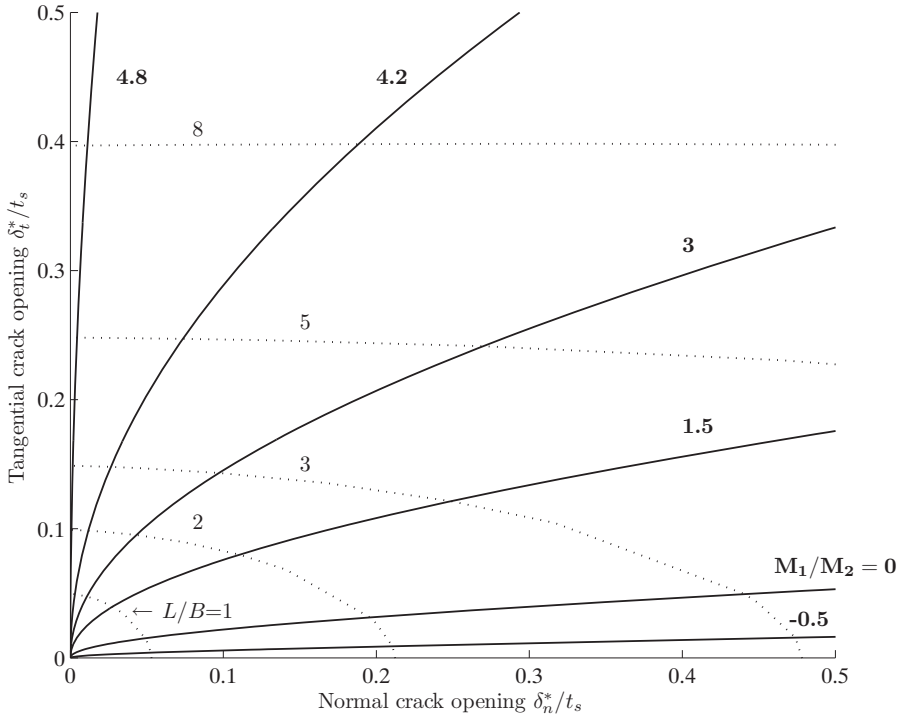

Figure A.1: Normal and tangential end opening displacement for constant J and varying moment ratio and crack length. $J/(E_s t_s) = 8 \cdot 10^{-7}$, $B/t_s = 5$, $E_f = 14.1$ GPa, $\nu_f = 0.32$, $t_f = 2.9$ mm, $E_c = 240$ MPa, $\nu_c = 0.3$, and $t_c = 57$ mm.

PhD Theses
Department of Naval Architecture and Offshore Engineering
Technical University of Denmark · Kgs. Lyngby

1961 Strøm-Tejsen, J.
Damage Stability Calculations on the Computer DASK.

1963 Silovic, V.
A Five Hole Spherical Pilot Tube for three Dimensional Wake Measurements.

1964 Chomchuenchit, V.
Determination of the Weight Distribution of Ship Models.

1965 Chislett, M.S.
A Planar Motion Mechanism.

1965 Nicordhanon, P.
A Phase Changer in the HyA Planar Motion Mechanism and Calculation of Phase Angle.

1966 Jensen, B.
Anvendelse af statistiske metoder til kontrol af forskellige eksisterende tilnærmelsesformler og udarbejdelse af nye til bestemmelse af skibes tonnage og stabilitet.

1968 Aage, C.
Eksperimentel og beregningsmæssig bestemmelse af vindkræfter på skibe.

1972 Prytz, K.
Datamatorienterede studier af planende bådes fremdrivningsforhold.

1977 Hee, J.M.
Store sideportes indflydelse på langskibs styrke.

1977 Madsen, N.F.
Vibrations in Ships.

1978 Andersen, P.
Bølgeinducerede bevægelser og belastninger for skib på lægt vand.

1978 Römeling, J.U.
Buling af afstivede pladepaneler.

1978 Sørensen, H.H.
Sammenkobling af rotations-symmetriske og generelle tre-dimensionale konstruktioner i elementmetode-beregninger.

1980 Fabian, O.
Elastic-Plastic Collapse of Long Tubes under Combined Bending and Pressure Load.

1980 Petersen, M.J.
Ship Collisions.

1981 Gong, J.
A Rational Approach to Automatic Design of Ship Sections.

1982 Nielsen, K.
Bølgeenergimaskiner.

1984 Nielsen, N.J.R.
Structural Optimization of Ship Structures.

1984 Liebst, J.
Torsion of Container Ships.

1985 Gjersøe-Fog, N.
Mathematical Definition of Ship Hull Surfaces using B-splines.

1985 Jensen, P.S.
Stationære skibsbølger.

1986 Nedergaard, H.
Collapse of Offshore Platforms.

1986 Yan, J.-Q.
3-D Analysis of Pipelines during Laying.

1987 Holt-Madsen, A.
A Quadratic Theory for the Fatigue Life Estimation of Offshore Structures.

1989 Andersen, S.V.
Numerical Treatment of the Design-Analysis Problem of Ship Propellers using Vortex Lattice Methods.

1989 Rasmussen, J.
Structural Design of Sandwich Structures.

1990 Baatrup, J.
Structural Analysis of Marine Structures.

1990 Wedel-Heinen, J.
Vibration Analysis of Imperfect Elements in Marine Structures.

1991 Almlund, J.
Life Cycle Model for Offshore Installations for Use in Prospect Evaluation.

1991 Back-Pedersen, A.
Analysis of Slender Marine Structures.

1992 Bendiksen, E.
Hull Girder Collapse.

1992 Petersen, J.B.
Non-Linear Strip Theories for Ship Response in Waves.

1992 Schalck, S.
Ship Design Using B-spline Patches.

1993 Kierkegaard, H.
Ship Collisions with Icebergs.

1994 Pedersen, B.
A Free-Surface Analysis of a Two-Dimensional Moving Surface-Piercing Body.

1994 Hansen, P.F.
Reliability Analysis of a Midship Section.

1994 Michelsen, J.
A Free-Form Geometric Modelling Approach with Ship Design Applications.

1995 Hansen, A.M.
Reliability Methods for the Longitudinal Strength of Ships.

1995 Branner, K.
Capacity and Lifetime of Foam Core Sandwich Structures.

1995 Schack, C.
Skrogudvikling af hurtiggående færger med henblik på sødygtighed og lav modstand.

1997 Simonsen, B.C.
Mechanics of Ship Grounding.

1997 Olesen, N.A.
Turbulent Flow past Ship Hulls.

1997 Riber, H.J.
Response Analysis of Dynamically Loaded Composite Panels.

1998 Andersen, M.R.
Fatigue Crack Initiation and Growth in Ship Structures.

1998 Nielsen, L.P.
Structural Capacity of the Hull Girder.

1999 Zhang, S.
The Mechanics of Ship Collisions.

1999 Birk-Sørensen, M.
Simulation of Welding Distortions of Ship Sections.

1999 Jensen, K.
Analysis and Documentation of Ancient Ships.

2000 Wang, Z.
Hydroelastic Analysis of High-Speed Ships.

2000 Petersen, T.
Wave Load Prediction—a Design Tool.

2000 Banke, L.
Flexible Pipe End Fitting.

2000 Simonsen, C.D.
Rudder, Propeller and Hull Interaction by RANS.

2000 Clausen, H.B.
Plate Forming by Line Heating.

2000 Krishnaswamy, P.
Flow Modelling for Partially Cavitating Hydrofoils.

2000 Andersen, L.F.
Residual Stresses and Deformations in Steel Structures.

2000 Friis-Hansen, A.
Bayesian Networks as a Decision Support Tool in Marine Applications.

PhD Theses
Maritime Engineering · Department of Mechanical Engineering
Technical University of Denmark · Kgs. Lyngby

2001 Lützen, M.
Ship Collision Damage.

2001 Olsen, A.S.
Optimisation of Propellers Using the Vortex-Lattice Method.

2002 Rüdinger, F.
Modelling and Estimation of Damping in Non-linear Random Vibration.

2002 Bredmose, H.
Deterministic Modelling of Water Waves in the Frequency Domain.

2003 Urban, J.
Crushing and Fracture of Lightweight Structures.

2003 Lazarov, B.S.
Slepian Simulations of Plastic Displacement of Randomly Excited Hysteretic Structures.

2003 Ravn, E.S.
Probabilistic Damage Stability of Ro-Ro Ships.

2003 Törnqvist, R.
Design of Crashworthy Ship Structures.

2003 Nielsen, K.B.
Numerical Prediction of Green Water Loads on Ships.

2004 Folsø, R.
Comfort Monitoring of High Speed Passenger Ferries.

2004 Fuhrman, D.R.
Numerical Solutions of Boussinesq Equations for Fully Nonlinear and Extremely Dispersive Water Waves.

2004 Dietz, J.S.
Application of Conditional Waves as Critical Wave Episodes for Extreme Loads on Marine Structures.

2004 Berggreen, C.
Damage Tolerance of Debonded Sandwich Structures.

PhD Theses
Coastal, Maritime and Structural Engineering
Department of Mechanical Engineering
Technical University of Denmark · Kgs. Lyngby

2005 Berntsen, K.N.
Modelling Granular Media and Molecular Dynamics Simulations of Ellipses.

2005 Nielsen, U.D.
Estimation of Directional Wave Spectra from Measured Ship Responses.

2005 Vidic-Perunovic, J.
Springing Response due to Bidirectional Wave Excitation.

2005 Zhang, H.
A Deterministic Combination of Numerical and Physical Models for Coastal Waves.

2005 Høgsberg, J.R.
Modelling of Dampers and Damping in Structures.

2006 Engsig-Karup, A.P.
Unstructured nodal DG-FEM solution of high-order Boussinesq-type equations.

2006 Yamada, Y.
Bulbous Buffer Bows: A Measure to Reduce Oil Spill in Tanker Collisions.

2008 Lundsgaard-Larsen, C.
Predicting and Improving Damage Tolerance of Composite Structures.

DTU Mechanical Engineering
Section of Coastal, Maritime and Structural Engineering
Technical University of Denmark

Nils Koppels Allé, Bld. 403
DK-2800 Kgs. Lyngby
Denmark
Phone (+45) 4525 1360
Fax (+45) 4588 4325
www.mek.dtu.dk
ISBN: 978-87-89502-83-0

DCAMM
Danish Center for Applied Mathematics and Mechanics

Nils Koppels Allé, Bld. 404
DK-2800 Kgs. Lyngby
Denmark
Phone (+45) 4525 4250
Fax (+45) 4593 1475
www.dcamm.dk
ISSN: 0903-1685